Microscopic Aspects of Ageing in Al-Mg-Si Alloys

vorgelegt von

Master of Science

Mazen Adel Madanat

geb. in AlKarak / Jordanien

von der Fakultät III – Prozesswissenschaften
der Technischen Universität Berlin
zur Erlangung des akademischen Grades

Doktor der Naturwissenschaften

– Dr. rer. nat. –

genehmigte Dissertation

Promotionsausschuss:

Vorsitzender: Prof. Dr. Walter Reimers
Gutachter: Prof. Dr. John Banhart
Gutachter: Prof. Dr. Olaf Keßler

Tag der wissenschaftlichen Aussprache: 27. April 2018

Berlin 2018

الإهداء

إلى من أحمل أسمه بكل إفتخار.. إلى من كلله الله بالهيبة والوقار
إلى من رسم المستقبل بخطوط من الأمل والثقة.. إلى الذي لا تفيه الكلمات...

والدي العزيز أمد الله في عمره

إلى ملاكي في الحياة.. إلى من أرضعتني الحب والحنان
إلى من عرفت معها معنى الحياة.. إلى المتربعة على عرش الأيام...

والدتي العزيزة أمد الله في عمرها

إلى السند الذين يضيئون طريق الحياة
إلى من شاركني حضن ألام وبهم استمد عزتي وإصراري

إخوتي وأحبتي

إلى الذين تسكن صورهم وأصواتهم أجمل اللحظات والأيام
إلى الذين برفقتهم سرت دروب الحياة

أصدقائي و زملائي

إلى الذين مهدوا الطريق للوصول الى ذروة العلم

أساتذتي

(Acknowledgement in Arabic language)

Abstract

Al-Mg-Si alloys with a low solute content (0.4 %Mg, 0.4 %Si) and higher contents (Mg+Si=1.4 %, all in wt.%) were solutionized, quenched and then either artificially aged (AA) at 180 °C or naturally pre-aged (NPA) for 2 weeks at room temperature and then reverse aged (RA) at 250 °C. Subsequently, positron annihilation lifetime spectroscopy was applied with the objective of obtaining information about precipitation and vacancy evolution during AA and solute cluster dissolution during RA. Hardness, electrical resistivity and differential scanning calorimetry measurements were also carried out to complement the measurements of positron lifetime.

In addition to AA and RA, natural secondary ageing (NSA) was studied after different AA or RA treatments since the corresponding cluster formation or dissolution phenomena change the positron lifetime, which in turn allows us to infer which microscopic states various AA or RA produce. AA was carried out in four different heating media which allowed for varying the heating rate from 3 to 190 K/s. For the case of RA, only two heating media were chosen, the heating rates equaling 15 and 220 K/s, correspondingly.

The main results of this study are:

For *AA treatment*, there is a competition between vacancy losses and cluster formation. The more precipitation takes place before and during AA, the more vacancies are retained and act back on clustering. Higher solute content, slower heating to 180 °C, natural pre-ageing before AA and slower quenching after solutionising were found to have a comparable effect explainable by pre-precipitation before AA. NSA after AA was found to depend on vacancy concentration and supersaturation of solutes, which are especially high in alloys with a high solute (especially Si) content and after fast heating to 180 °C.

For *RA treatment*, the reversion of natural ageing (NA), i.e. the dissolution of NPA clusters sets in immediately even for the shortest RA time of 1 s. This effect was explained by the interactions between excess vacancies which are still high in concentration and solute clusters which temporarily retain them. Longer RA treatments further dissolve such clusters until maximum dissolution is reached. The clustering characteristics during the subsequent NA (NSA) after RA further imply that this process is governed by the vacancy concentration at the early stage, and by both the solute supersaturation and the chemical composition as NSA proceeds.

Kurzfassung

Niedrig- (0.4 %Mg, 0.4 %Si) und höher- (Mg+Si=1.4 %, alle in wt. %) legierte Al-Mg-Si-Legierungen wurden in dieser Arbeit lösungsgeglüht, abgeschreckt und dann entweder bei 180°C warm ausgelagert (artificial ageing, AA) oder bei Raumtemperatur kalt ausgelagert (natural pre-aging, NPA) und anschließend bei 250°C rückgeglüht (reverse ageing, RA). Anschließend wurde Positronen-Annihilations-Spektroskopie angewandt, um Informationen über Ausscheidungen und Leerstellenbildung entweder während der Warmauslagerung oder der Clusterauflösung während der Rückglühung zu beobachten. Zudem wurden Härte-, elektrische Widerstands- und dynamische Differenzkalorimetriemessungen durchgeführt, um die Messungen der Lebensdauer der Positronen zu vervollständigen.

Zusätzlich wurden Raumtemperatur-Nachauslagerungen (natural secondary ageing, NSA) nach unterschiedlichen Warmauslagerungen und Rückglühbehandlungen untersucht, da die damit eingehenden Auflösungsphänomene und die Clusterbildung die Positronen-Lebensdauer verändern können. Dadurch wiederum kann festgestellt werden, welche mikroskopischen Zustände von den unterschiedlichen Wärmebehandlungen hervorgerufen werden. Warmauslagerung wurde in vier verschiedenen Heizgeräten durchgeführt, was eine Variation der Heizrate von 3 bis 190 K/s ermöglichte. Für die Rückglühung wurden zwei Heizraten, nämlich 15 und 220 K/s, gewählt.

Die wichtigsten Resultate diese Arbeit sind:

Während der Warmauslagerung sind Leerstellenverluste und Clusterbildung gegenläufig. Je mehr Ausscheidungen sich vor und während der Auslagerung bilden, desto mehr Leerstellen bleiben erhalten, was die weitere Clusterbildung begünstigt. Es wurde festgestellt, dass ein höherer Legierungsgehalt, langsameres Heizen auf 180 °C, Kaltvorauslagerung vor der Warmauslagerung und langsameres Abschrecken nach dem Lösungsglühen einen vergleichbaren Effekt hervorrufen, der durch eine Ausscheidungsbildung vor der Warmauslagerung erklärt werden kann. Die Raumtemperatur-Nachauslagerung nach der Warmauslagerung wird hingegen von der Leerstellenkonzentration und der Übersättigung an gelösten Elementen bestimmt, welche besonders in den höherlegierten Systemen (besonders mit Si) und nach schnellem Heizen auf 180°C hoch sind.

Während der durch Rückglühung bewirkten *Rückbildung* der Kaltauslagerung setzt die Auflösung von Clustern schon nach der kürzesten Zeit von 1 s merklich ein. Der Effekt wird erklärt durch die Wechselwirkungen zwischen überschüssigen Leerstellen, welche immer noch in hoher Konzentration vorliegen, und Atomclustern, welche erstere eine Weile zurückhalten. Längere Rückglühung löst diese Cluster bis zu einem gewissen Grad auf, wonach sich erneut Phasen bilden. Die beobachtete Clusterbildung während der Raumtemperatur-Nachauslagerung lässt den Schluss zu, dass dieser Prozess in frühen Stadien von der Leerstellenkonzentration gesteuert wird sowie während des weiteren Verlaufs der Nachauslagerung sowohl von der Übersättigung der gelösten Elemente als auch von der chemischen Zusammensetzung der Matrix.

List of Abbreviations

AA	artificial ageing
AQ	as-quenched
CFD	constant fraction discriminator
DSC	differential scanning calorimetry
fcc	face-centered cubic
FWHM	full width at half maximum
GPZ	Guinier-Preston zones
HP	heating plates
IWQ	ice water quenching
LM	liquid metal
LN_2	liquid nitrogen
LN_2Q	liquid nitrogen quenching
MCA	multi-channel analyzer
MS	molten salt
NA	natural ageing
NPA	natural pre-ageing
NSA	natural secondary ageing
PALS	positron annihilation lifetime spectroscopy
PLT	positron lifetime
PMT	photomultiplier tube
RA	reverse ageing
RT	room temperature
SC	scintillator crystal
SCA	single-channel analyzer
SHT	solution heat treatment
SSSS	supersaturated solid solution
STM	simple trapping model
TAC	time-to-amplitude converter

Table of Contents

1 Introduction

The ternary system Al-Mg-Si defines the technologically important 6xxx series of age-hardenable alloy. Such alloys are widely used in the automotive industry due to their excellent mechanical properties such as, low specific weight, medium to high strength, good formability and corrosion resistance, etc.

After solutionising and quenching, artificial ageing (AA) at typically 180 °C leads to the formation of a series of metastable precipitates that increase strength. 6xxx alloys are well investigated and the precipitation sequence is known, however, not in all details and not under all circumstances (alloy compositions, multi-stage treatments, etc.) [1].

Even the simplest case – direct AA after quenching – bears some unknown problems. The structure of the earliest precipitates is not known. It has to be assumed that the first precipitates have the fcc structure of the host metal and later transform to monoclinic GP zones and β" precipitates [2-4] but how this happens and how the precipitates grow is not known with certainty [5, 6]. Moreover, the role of vacancies in the first stages of AA is not clear. After quenching, the high site fraction of vacancies at the solutionising temperature is partially preserved. During artificial ageing, excess vacancies anneal out and eventually the vacancy site fraction approaches the equilibrium value at, say 180 °C, but how fast this happens is not clear because vacancy annihilation is influenced by interaction with dislocations and growing precipitates [7]. Solute supersaturation is also a crucial factor since it provides the driving force for precipitation. How it varies during AA is not exactly known. The situation becomes even more complicated once natural ageing (NA) steps are involved, either as natural pre-ageing (NPA) before AA or as natural secondary ageing (NSA) after AA.

With the work presented here, we intend to contribute to the understanding of the role of vacancies and solutes in the early (and also later) stages of AA. We study very short AA treatments down to 0.3 s and also vary the heating rate from 'room temperature' to 180 °C. The main tool employed is positron annihilation lifetime spectroscopy (PALS). This method is sensitive to vacancies and clusters/precipitates and has been applied previously to explain the NA behaviour in identical alloys [8, 9]. Another objective is to specify the pronounced differences in ageing behaviour between lean Al-Mg-Si alloys (≤ 1% Mg+Si) and more concentrated ones.

As PALS is not fast enough to resolve ageing phenomena that take place on a time scale of seconds, we investigate samples after AA at 180 °C for different times at 'room temperature' or even lower temperatures ('ex-situ'). The changes during NSA can then be followed in-situ. The study of NSA is an indirect method aiming at deducing the state during or immediately after AA from its long-term behaviour at 'room temperature' and been applied before to Al-Mg-Si [10], Al-Cu-Mg [11] and Al-Zn-Mg alloys [12], however, without completely explaining the changes of positron lifetime observed.

Moreover, applying NPA after solutionising and quenching yields to pronounced clustering phenomena that increase both electrical resistivity and hardness. Clustering negatively affects a subsequent AA step at, for example, 180 °C, which explains the interest in its study. Experimentally, clustering is not easily accessible in direct observation due to the high rate at which it takes place, the low solute concentration, the small size of clusters and the low imaging contrast between Al, Mg and Si [13].

One possible way to study clustering is to dissolve previously formed clusters by applying a sufficiently high temperature instead of observing their formation after solutionising and quenching. The so-called reversion ageing (RA) puts back a part of the solute atoms confined in clusters and possibly also some of the captured vacancies. RA leads to a pronounced decrease of hardness, resistivity and also influences other properties influenced by atomic clusters. By studying the kinetics of reversion one can derive properties of clusters.

Reversion in the Al-Mg-Si alloy family was first studied in Al-0.4Mg-0.5Si(Fe) alloys. It was found that the hardness of the NA state (T4) was reverted at 200 °C and 250 °C in minutes, whereas at 160 °C and lower temperatures no reversion was observed. The reverted state was prone to further (secondary) natural ageing which led to the same final hardness as the first NA step [14]. Reversion of electrical resistivity was also observed [15].

In the current work, we apply four methods to characterise reversion: Vickers hardness (HV) and electrical resistivity measurement (RES), differential scanning calorimetry (DSC) and positron annihilation lifetime spectroscopy (PALS). These methods have all proved to be sensitive to clustering in many previous studies. A first type of experiment is the measurement of properties directly after reversion ageing at 250 °C for different times ranging from 1 s to several minutes.

Two quenching media provided different heating rates to the final reversion temperature. A second type of experiment was the analysis of properties measured during natural secondary ageing after reversion. As these changes were slow they could be in some cases be studied in-situ.

We study pure ternary model alloys to keep out possible effects of both common solute atoms such as Cu that might influence precipitation and intermetallic-forming elements such as Fe and Mn that might lower the Si content and also trap positrons. Most investigations are carried out on one lean alloy (~0.4% of both Mg and Si, similar to industrial alloy 6060) and one alloy higher in solute (0.6% Mg, 0.8% Si, similar to industrial alloy 6005).

2 Theory

2.1 Aluminium Alloys

Aluminium is the third most abundant element in the earth's crust. It is considered as the second most used metal in our time after iron [16, 17]. Pure aluminium itself is a low strength material and this limits its industrial applications. However, the addition of alloying elements such as Mg, Si, etc. makes it possible to produce aluminium alloys with more favorable "specialized" properties, e.g. light weight, medium to high strength, formability, etc. [16], which fulfill the requirements of use as engineering materials in the automotive industry [16]. Information about the properties and categories of aluminium alloys are given below.

2.1.1 Classification

The two main categories of aluminium alloys are: cast and wrought alloys. The former are alloys cast to their final shapes, while the latter undergo subsequent processes after casting, e.g. homogenization, hot rolling, cold rolling, etc. to achieve the required properties. Both alloys can be further divided into two subcategories: heat treatable and non-heat treatable alloys. The different series of wrought alloys and their designation are given in Table 1. The main focus of this work is the age-hardenable 6xxx series Al-Mg-Si alloys, which are widely used as car body panel.

Table 1. Different series of wrought aluminium alloys and their main alloying elements [18].

Designation	Main alloying elements	Heat-treatability
1xxx	-	No
2xxx	Cu	Yes
3xxx	Mn	No
4xxx	Si	No
5xxx	Mg	No
6xxx	Mg, Si	Yes
7xxx	Mg, Cu, Zn	Yes

2.1.2 Strengthening Mechanisms

Various methods can be used to improve the strength of aluminium alloys, including, but not limited to work hardening, grain hardening, solid solution hardening and age hardening. Brief descriptions of these mechanisms are given in the following:

- Work hardening

This is also known as cold working. Exposing the material to a plastic deformation leads to the displacement of the atoms from their equilibrium position permanently and dislocations are formed. As a result of the high dislocation density, higher numbers of dislocation-dislocation interactions occur and the movement of dislocations is inhibited.

- Grain hardening

The movements of dislocations from one grain to the other can be obstructed by the grain boundaries. Since grains differ in the crystallographic orientation, a dislocation moving to the next grain will have to change its direction. Therefore, it is plausible that dislocations 'pile up' at the grain boundaries rather than overpass them. Grain size plays a major role in this process, for instance, a smaller grain size means more grains, which in turn, implies a higher number of grain boundaries, i.e. more obstacles to the motion of the dislocations.

- Solid solution hardening

In either substitutional or interstitial solid solution, strain fields will be created if the size of solutes is larger or smaller than the solvent atoms, i.e. the regularity of the lattice structure is interrupted in the vicinity of such atoms, see Figure 1a. As a result, the movement of dislocation is prohibited due to their interaction with the corresponding strain fields.

- Age hardening

The solid solubility of the alloying elements of age-hardenable alloys decreases significantly with lessened temperature. Thus, after solutionising and quenching, the solid solution becomes supersaturated. Subsequent 'natural ageing (NA)' at 'room temperature (RT)' or 'artificial ageing (AA)' at an elevated temperature correspondingly leads to the formation of uniformly distributed

particles such as solute clusters or precipitates (see Figure 1b). The precipitation sequence in 6xxx series alloys has been proposed by many researchers [13, 19-22]. Although not all details are known, it can be generally summarized as:

Super saturated solid solution (SSSS) → Clusters → Guinier-Preston zone (GPZ) → β'' → β' → β

Such phases can effectively hinder the movement of dislocations. As the main strengthening mechanism related to this work, it will be explained in detail in the following [16, 23]:

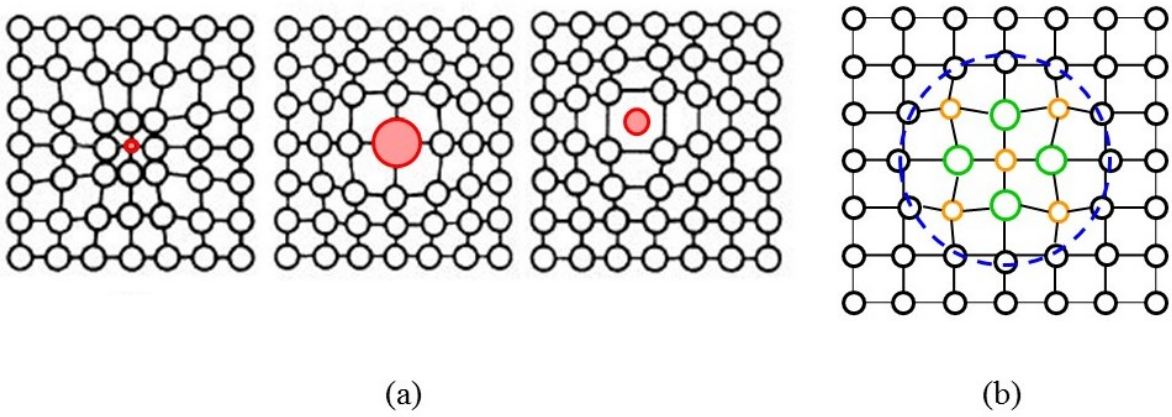

Figure 1. Schematic illustration of the strain fields in the aluminuim matrix created by (a) a small/large substitution atom and an interstitial atom [23], (b) a coherent precipitate.

- Clustering

Clusters can be defined as aggregations of solute atoms with a non-defined structure which are formed during the early stages of NA. In 6xxx series alloys, the diffusion of Si and Mg atoms is aided by quenched-in vacancies. Girifalco & Herman [24] proposed a "vacancy-pump model" to explain the clustering process: a vacancy is able to detach from a cluster, assuming that the binding between a vacancy and a single solute is stronger than to a solute cluster. The liberated vacancy then goes back to the matrix where it brings more solutes to the cluster. However, this assumption appears illogical, thus, Zurob & Seyedrezai [25] rather assumed that the possibility for a vacancy to escape from a cluster scales with $\exp(-nE_b)$, with n the number of solute atoms in that cluster, c a constant and E_b the binding energy between a vacancy and a solute atom. Based on this model, the clustering rate is the highest immediately after solutionising and quenching due to the high number of mobile vacancies. When NA proceeds, not only the degree of solute supersaturation

decreases but also the concentration of vacancies approaches the thermal equilibrium level due to their trapping in clusters and loss at sinks, thus, the kinetics of clustering slows down.

- Precipitation

The precipitates are phases with defined structures formed at elevated temperatures. Guinier-Preston zones (GPZ) – as the earliest precipitation phase to form, are coherent, fine-scaled and solute enriched regions. Sometimes GPZ are also known as the precursor of the metastable β" phase due to their closely related structures [2, 4, 20, 26-28]. The Mg/Si ratio is close to 1 [27, 29].

The coherent and needle-shaped β" phase is formed on the basis of GPZ during AA and is known as the main hardening phase. It has a monoclinic structure with lattice parameters of a=1.516 nm, b=0.405 nm, c=0.674 nm and an angle between b and c of 105.3° [30]. The composition of the β" phase has been proposed by many authors, e.g. Mg_5Si_6 [3], based on the atom probe tomography experiments. The exact stoichiometry of the precipitates varies with the alloy's chemical composition [31-34]. Recent studies showed that β" precipitate contains also ~25% of Al [32, 35, 36].

The β" phase turns into semi-coherent β' phase when AA time is long enough. The new phase has a rod shape with lattice parameters of a=0.715 nm and c=1.215 nm and a chemical composition of Mg_9Si_5 [37]. Although β' is more stable than β", the corresponding hardness of the alloy decreases due to the loss in coherency [29].

The incoherent equilibrium β phase is finally achieved for an even longer AA time. The structure of this phase is in form of cubes and plates with lattice parameters of a=1.04 nm and b=0.405 nm and a chemical composition of Mg_2Si. Due to the elimination of coherency strain, the strength of the material further decreases.

Many other phases are also possible to form during age hardening. The exact sequence of phase formation, however, can be affected by many factors such as the heating rate, temperature and the alloy composition [13].

- Hardening Procedures

The actual strengthening processes, by which the movement of dislocations is hindered, are explained in the following. There are in general three kinds of strengthening mechanisms, depending on the coherency strain and the sizes of particles [23] (Figure 2):

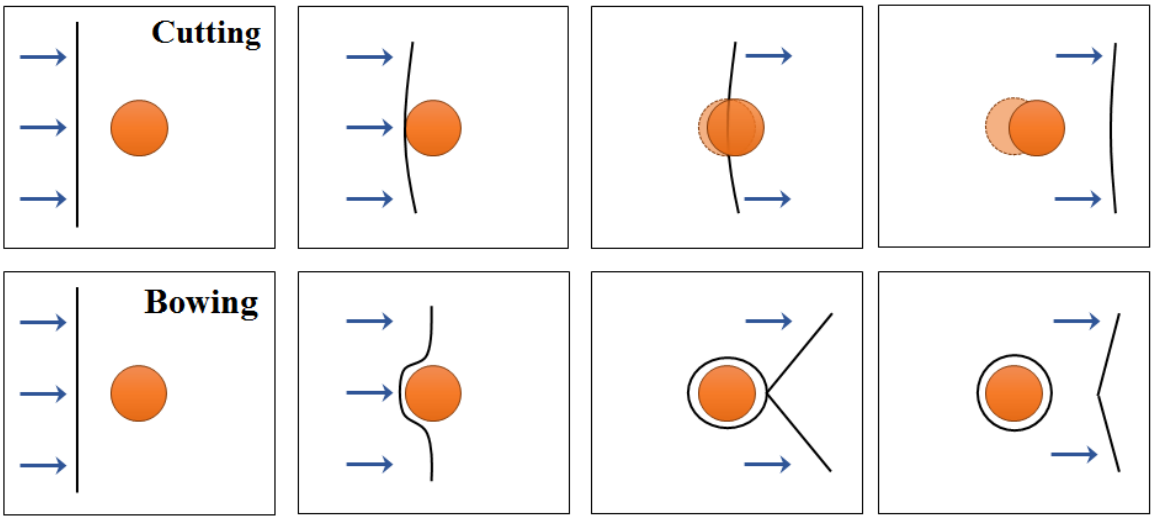

Figure 2. Dislocation (black line) cutting through or bowing around a particle (orange sphere) [23].

(1) Dislocation movement prohibited by strain fields. GPZ are formed during the early stages of AA. High strain fields are introduced due to the coherent structure of such zones. Consequently, larger shear stress is required for the dislocations to move through the matrix.

(2) Dislocations cutting through particles. Dislocations can cut coherent particles, provided that the particles are small. The shear stress depends on both the stress field of the particle and the extra energy to create the new interfacial areas. The strength of the material increases with increasing particle radius.

(3) Dislocations bowing around particles. For large particles, it is no longer possible for dislocations to cut through due to their incoherent structure. Instead, dislocations bow around such particles ("Orowan bowing") after which dislocation loops are left and this leads to a further increase in strength due to interactions with subsequently passing dislocations.

2.2 Basics of Positron Annihilation Spectroscopy

The positron annihilation spectroscopy (PAS) is a nuclear technique widely applied in solid state physics and materials science. The positron (e^+) is the antiparticle of the electron (e^-). After a positron has entered the material, it will annihilate with an electron after a certain time. The annihilation quanta can be detected and provide the spectroscopic signal for varies techniques, e.g. positron annihilation lifetime spectroscopy (PALS). Information about the solid microstructure can be obtained by these signals which depend on the defects and phase compositions. The non-destructive PAS technique has many advantages, above all, the high sensitivity to open volume defects such as vacancies.

2.2.1 Positron Generation

Positron can be generated via various procedures such as the pair production ($\gamma + \gamma \rightarrow e^+ + e^-$), the decay of anti-muon ($\mu^+ \rightarrow e^+ + \nu + \bar{\nu}_\mu$) or isotopes. ^{22}Na is the most commonly used positron source in laboratories. The decay equation of the ^{22}Na source is:

$$^{22}Na \rightarrow {}^{22}Ne + e^+ + \upsilon_e + \gamma\ . \qquad (2.1)$$

^{22}Na has a relatively long half-lifetime of 2.6 years and a high positron yield of 90.4%. More importantly, a 1.275 MeV gamma quantum is "simultaneously" emitted with the "birth" of the positron (Figure 3). This unique feature makes ^{22}Na an ideal source for positron lifetime measurements.

2.2.2 Positron-Matter Interaction and the Positron Lifetime

Energetic positrons penetrating the sample rapidly thermalize within a few ps [38]. After reaching a kinetic energy of ~40 meV (at RT), positrons start to diffuse in the lattice. Due to its positive charge, a positron will be repelled by the positive nuclei, thus, most likely, it diffuses in the interstitial regions. By the presence of open volume defects, e.g. vacancies, positrons are trapped due to the missing positively charged nuclei. Once a positron annihilates with an electron, two 0.511 MeV gamma quanta will be released. The measured time difference between the 1.275 MeV gamma quantum (start signal) and one of the 0.511 MeV (stop signal) gamma quanta is the so called "positron lifetime" τ. The entire process is shown schematically in Figure 4.

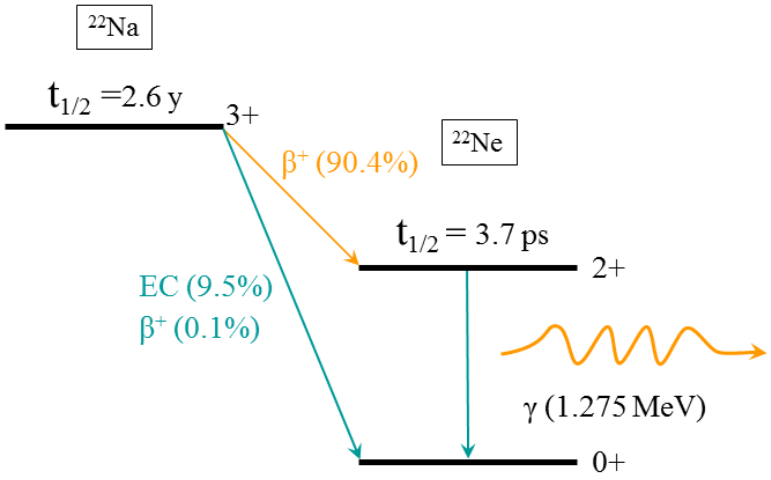

Figure 3. Decay diagram of ^{22}Na. The β^+ decay (90.4%) to the excited state of ^{22}Ne produces positrons. The de-excitation to the ground state within 3.7 ps leads to the emission of the 1.275 MeV gamma quantum. Other processes with lower probabilities to occur are electron capture (EC) and direct β^+ decay to the ground state.

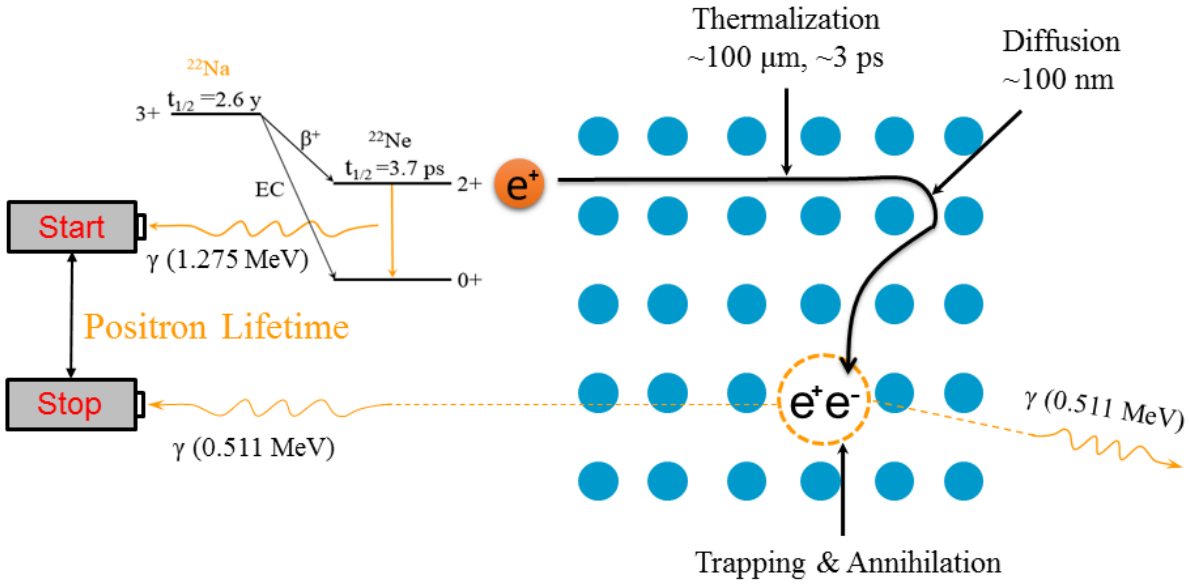

Figure 4. Schematic illustration of PALS technique [39].

2.2.3 Positron Traps

Not only vacancies, but also solute clusters, GPZ, precipitates and their corresponding interfaces can also trap positrons. Figure 5 shows the positron wave functions Ψ_+ of such traps with the corresponding potentials $V_+(x)$ [38]:

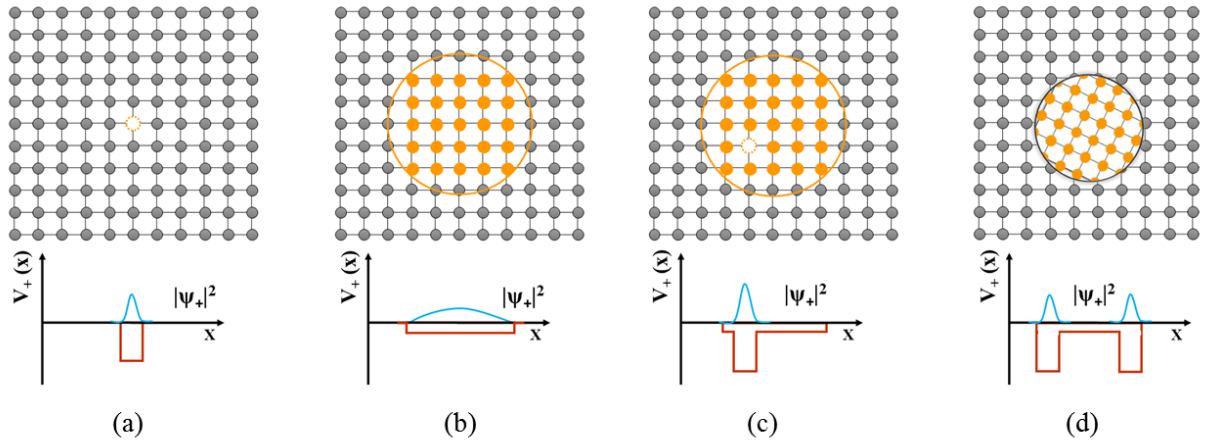

Figure 5. Schematic illustration of the positron wave functions Ψ_+ and the potentials $V_+(x)$ of various types of positron traps: (a) mono-vacancy, (b) fully coherent precipitate, (c) coherent precipitate containing a vacancy, (d) semi-coherent or incoherent precipitate. The vacancy and the solute atoms are shown as orange open circles and dots, respectively.

As fore-mentioned, the positron wave function is strongly localized by open-volume defect such as vacancies. For coherent precipitate, the positron wave function is spreading over the entire precipitate. While for coherent precipitate containing a vacancy and semi-coherent or incoherent precipitate contains misfit defect, the positron wave function will be localized strongly by the vacancy and by the interface region.

The positron lifetime τ is the reciprocal of the annihilation rate λ:

$$\tau = \frac{1}{\lambda}, \tag{2.2}$$

where λ is proportional to the positron and electron density $n_{\pm}(r)$ at the annihilation site:

$$\lambda \propto \int n_+(r)\, n_-(r) \Gamma dr\,, \tag{2.3}$$

where r is the position vector. Γ is a function account for the (e^+, e^-) coulomb interaction. According to Eq. (2.2) and Eq. (2.3), the positron lifetime is higher in open-volume defects than in free-defect bulk material. This is caused by the locally reduced electron density there [38].

2.2.4 Trapping Model

Information about the type and concentration of the defects can be obtained by PALS. A trapping model proposed by [40, 41] and later on generalized by [42] can be applied to quantitatively analyze the influence of positron trapping in defects on the lifetime spectra [38].

- Simple Trapping Model (STM)

Positron trapping in a single open-volume defect type (e.g. vacancies) describes the simplest case of the positron trapping model [38].

If the vacancy concentration is not too high, the thermalized positrons may annihilate in the defect-free bulk with the annihilation rate λ_b. Otherwise, they might also be trapped by the vacancy with a trapping rate of κ_v during diffusion and annihilate subsequently with an annihilation rate λ_v, see Figure 6:

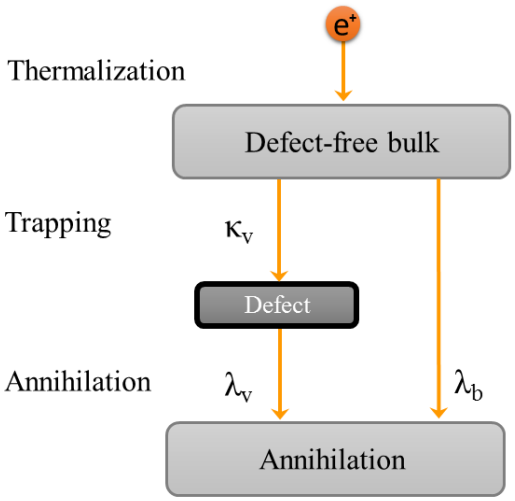

Figure 6. Schematic of the simple trapping model (STM) [38].

The rate equations are:

$$\frac{\mathrm{d}n_b\,(t)}{\mathrm{d}t} = -(\lambda_b + \kappa_v)\, n_b(t)\,, \tag{2.4}$$

$$\frac{\mathrm{d}n_v\,(t)}{\mathrm{d}t} = -\lambda_v n_v(t) + \kappa_v n_b(t)\,. \tag{2.5}$$

n_b and n_v are the number of positrons in the bulk and in the vacancy at time *t*. The initial conditions are $n_b(0) = N_0$, where N_0 is the number of positrons at $t = 0$ and $n_v(0) = 0$. The solution of Eqs. (2.4-2.5) is the decay spectrum of positrons:

$$D(t) = I_1\, exp\left(-\frac{t}{\tau_1}\right) + I_3\, exp\left(-\frac{t}{\tau_3}\right), \tag{2.6}$$

The annihilation parameters from Eq. (2.6) are given as:

$$\tau_1 = \frac{1}{\lambda_b + \kappa_v}, \tag{2.7}$$

$$\tau_3 = \frac{1}{\lambda_v}, \tag{2.8}$$

$$I_1 = 1 - I_3, \tag{2.9}$$

$$I_3 = \frac{\kappa_v}{\lambda_b - \lambda_v + \kappa_v}. \tag{2.10}$$

where τ_3 corresponds to the positron lifetime (PLT) in a vacancy (to avoid confusion, τ_2 will be used as PLT in a solute cluster in later sections), and the presence of such defects leads to the so-called "reduced bulk lifetime" τ_1 (<160 ps).

The trapping rate κ_v is proportional to the vacancy concentration *x* and to the specific trapping rate μ (2.5×10^{14} for mono-vacancies in Al [43]):

$$\kappa_v = \mu \cdot x = I_3\left(\frac{1}{\tau_1} - \frac{1}{\tau_3}\right) = \frac{I_3}{I_1}\left(\frac{1}{\tau_b} - \frac{1}{\tau_v}\right). \tag{2.11}$$

The average positron lifetime can be calculated from each individual component:

$$\bar{\tau} = \tau_1 \cdot I_1 + \tau_3 \cdot I_3. \tag{2.12}$$

The validity of the trapping model can be checked by calculating the positron lifetime in the bulk using the experimental data:

$$\tau_b^{calc} = \left(\frac{I_1}{\tau_1} + \frac{I_3}{\tau_3}\right)^{-1}, \tag{2.13}$$

which should be in the range of 158 to 166 ps [44, 45].

3 Experimental Techniques

3.1 Materials

3.1.1 Chemical Compositions

Ternary Al-Mg-Si alloys were provided by Hydro Aluminium Bonn as described elsewhere [8, 13], prepared using pure elements (Al 5N, Mg 4N, Si 5N). Chemical analyses showed that all samples had impurity contents less than 20 ppm, i.e. < 2/5 of the smallest solute content. The compositions are given in Table 2. The designations are given in the format 'x-y', where x stands for the Mg, y for the Si in 1/10 wt.% (at.%).

Table 2. Measured chemical compositions of all samples investigated in both wt.% and (at.%).

alloy designation	Mg	Si
4-4	0.39 (0.433)	0.40 (0.384)
5-5	0.46 (0.510)	0.54 (0.519)
4-10	0.40 (0.444)	1.01 (0.970)
6-8	0.59 (0.655)	0.79 (0.758)
8-6	0.80 (0.887)	0.61 (0.585)
10-4	1.02 (1.131)	0.41 (0.393)

3.1.2 Sample Preparation

The alloys were provided in the form of 3 mm-thick bars. The required thickness (1 mm) was then achieved by cold rolling and grinding. Samples of 10 × 10 × 1 mm^3 size were prepared for both PALS and hardness measurements. The hardness samples were further polished to achieve a mirror surface. The disc-shaped DSC samples are 4.8 mm in diameter, and the surface was ground to ensure a better contact with the Al crucible. Electrical resistivity samples were cut into strips, extruded, stretched and drawn into the form of coiled wires of ~350 mm in length and 0.81 mm in diameter. All samples were cleaned using alcohol prior to the solution heat treatment.

3.2 Heat Treatments

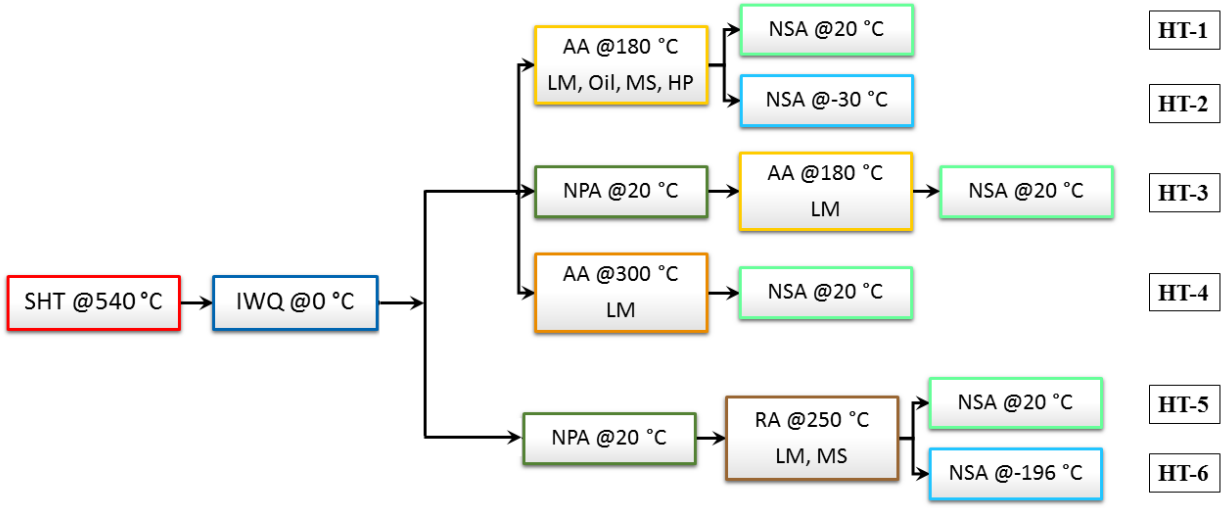

Figure 7. Heat treatments used in the work. SHT - solution heat treatment, IWQ - ice water quenching, AA - artificially ageing, NSA - natural secondary ageing, NPA - natural pre ageing, RA - reverse ageing, HT - heat treatment.

The heat treatments consist of three main steps, i.e. solutionising, quenching, and ageing. The samples were typically solutionized at 540 °C for 1 hour, during which the solute atoms enter into the solid solution. Following the solutionising heat treatment (SHT), the samples were rapidly quenched into ice water (IWQ) to hold these atoms in solution, forming the so-called "supersaturated solid solution (SSSS)". In addition, a considerable amount of quenched-in vacancies are also preserved. Subsequently, as the last step of the heat treatments, the samples were aged at different temperatures as shown in Figure 7, depending on the nature of the experiment. After each artificially ageing (AA) or reverse ageing (RA) step, the samples were IWQ. Details of the ageing treatments applied (HT-1 to HT-6) are given below:

- HT-1: Immediate AA at 180 °C for various times in one of four different media, i.e. liquid metal (LM), silicon oil (Oil), molten salt (MS) and heating plates (HP), followed by IWQ and then natural secondary ageing (NSA) at RT or at -30 °C.
    - Liquid metal: Highly thermally conductive and low-melting-point liquid alloy Bi57Sn43. The samples were kept in motion during ageing to ensure faster heating rate. Hereafter the sample surfaces were controlled by using a light microscope (Figure 8).

Except for the minute amount of LM residuals as shown in Figure 8, the sample surfaces were found to be clean in most cases.

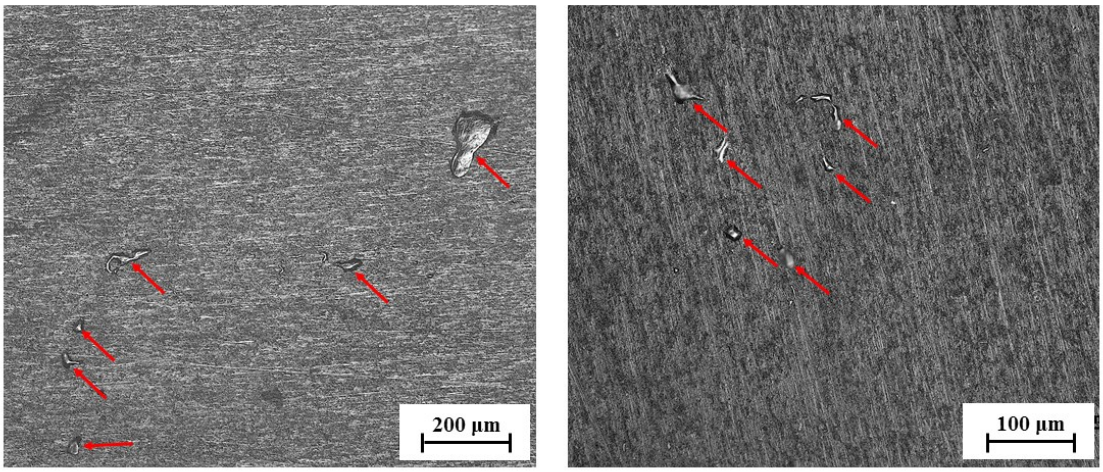

Figure 8. Light microscopic images of alloy 6-8 after artificially ageing (AA) in liquid metal bath (LM) at 180 °C for (a) 2 min and (b) 30 min. The red arrows indicate the rare occurrence of LM residual on the sample surface.

- Silicon oil: Samples were also kept in motion during ageing.
- Molten salt: A molten salt mixture of 53% KNO_3 + 40% $NaNO_2$ + 7% $NaNO_3$ with a low melting point of 142 °C and an operation range of 142 to 500 °C. The samples were kept in a resting position during ageing to ensure a slower heating rate.
- Controlled heating plates: heated at an initial rate of 3 K/s. During heating up, the samples were sandwiched between two Al plates to damp the temperature oscillations caused by the temperature controller.

The properties of the different ageing media used in this work are summarized in Appendix A.1.

- HT-2: Immediate AA at 180 °C for 1 s in LM, followed by cooling down to -30 °C.
- HT-3: Natural pre-ageing (NPA) for 5, 30 or 80 min at RT followed by AA for 1 s in LM. Subsequent NSA was performed at RT.
- HT-4: Immediate AA for a very short time (~0.3 s) at 300 °C in LM, followed by NSA at RT.
- HT-5: NPA for 2 weeks at RT followed by RA at 250 °C for various times in either LM or MS. Subsequently, the samples were aged at 20 °C.
- HT-6: NPA for 2 weeks at RT followed by RA at 250 °C in LM for a given time and then quenched into LN_2Q.

The thermal history of all measured samples as shown in Figure 7 is visualized in Figure 9:

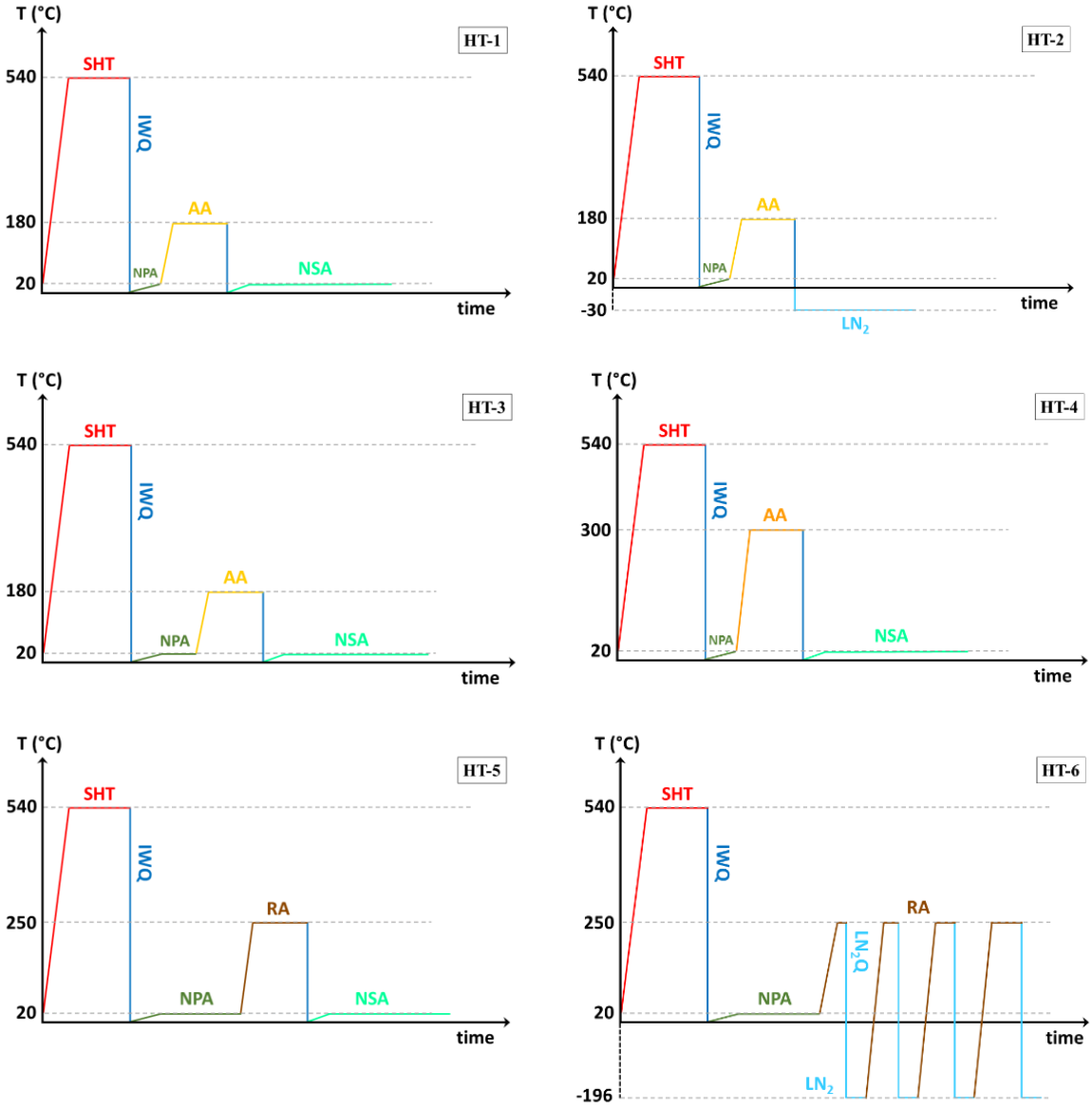

Figure 9. Temperature profiles used in this work. SHT - 1h@540 °C, IWQ@0 °C, NPA - 5, 30, 80 min or 2 w@20 °C, AA - various times@180 °C, AA - 0.3 s@300 °C, NSA@20, -30 or -196 °C, RA - various times @250 °C, LN_2Q@-196 °C.

The heating profiles in the different media used for AA at 180 °C and RA at 250 °C are given in Figure 11. The temperature courses were accurately measured using a k-type thermocouple (Ø 0.5 mm) inserted into holes drilled into the edge of test specimens (see Figure 10). The time required to reach 170 °C is 0.8 s for LM, which we call ‘fast heating’, 6 s for oil and 11 s for MS, which we call ‘intermediate heating’ and 63 s for the HP, ‘slow heating’ (Figure 11a). Regarding

the reverse ageing, the time required to reach 240 °C is 1 s and 15 s for LM and MS, respectively (Figure 11b).

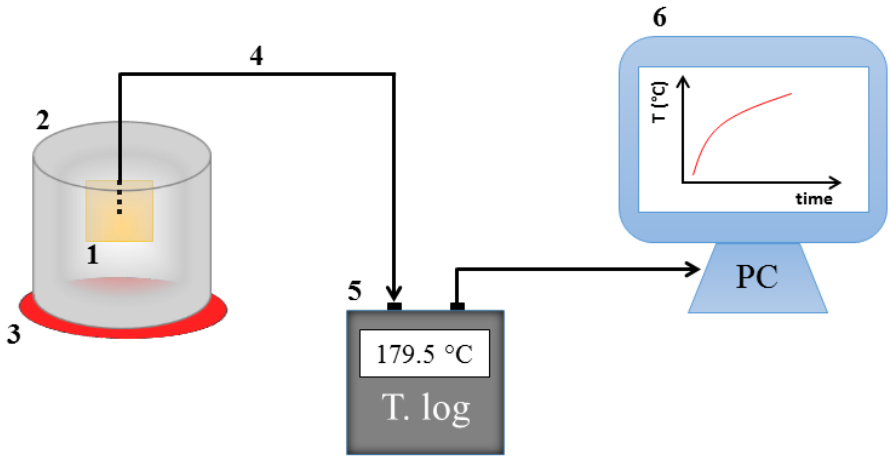

Figure 10. Measurement of the test specimen temperature during AA. A k-type thermocouple (ø0.5 mm) was inserted into the hole drilled into the edge of the sample and the temperature was registered by a temperature logger. 1 - Sample, 2 - ageing media, 3 – heating device, 4 - k-type thermocouple, 5 - temperature logger (T. log), 6 - computer.

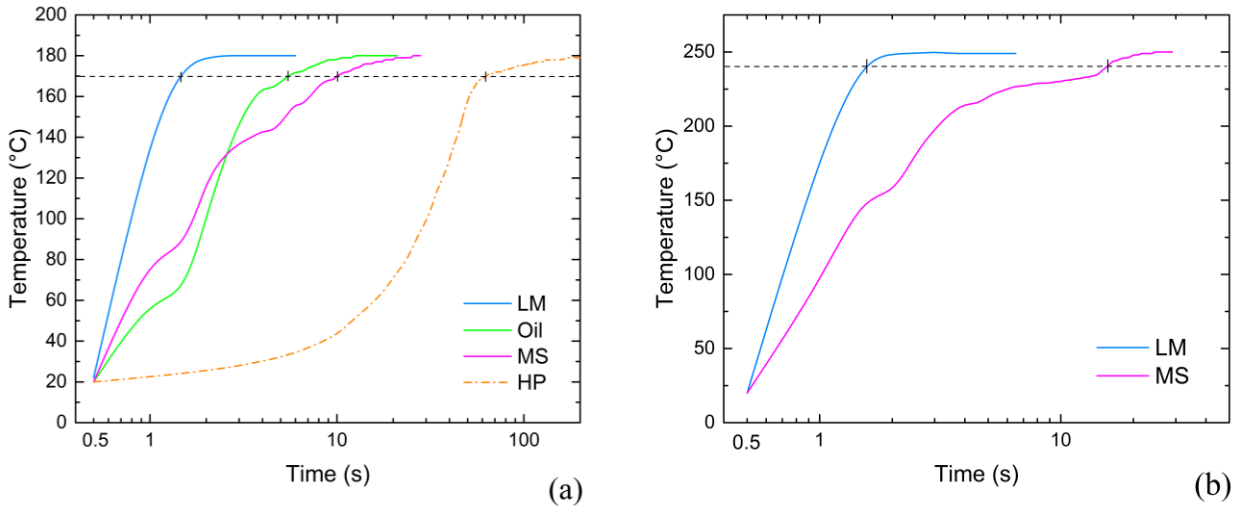

Figure 11. Heating profiles in the 4 different media used for AA at (a) 180 °C, (b) 250 °C. The starting time was set to 0.5 s to be able to use a logarithmic scale. Note that the linear heating ramp of HP in (a) appears as an exponential on this scale. Kinks in the heating curve in salt point at the melting of a crust of solid salt forming upon immersion of a cold sample. In oil some changes of slope are also observed.

3.3 Instruments and Data Analysis

3.3.1 Positron Annihilation Lifetime Spectroscopy (PALS)

Two identical samples were assembled to a "sandwich" with the positron source in between within 2 min. The annihilation signals were collected by the detection system and were further processed by the NIM (nuclear instrumental module)-standard electronics, as shown in Figure 12:

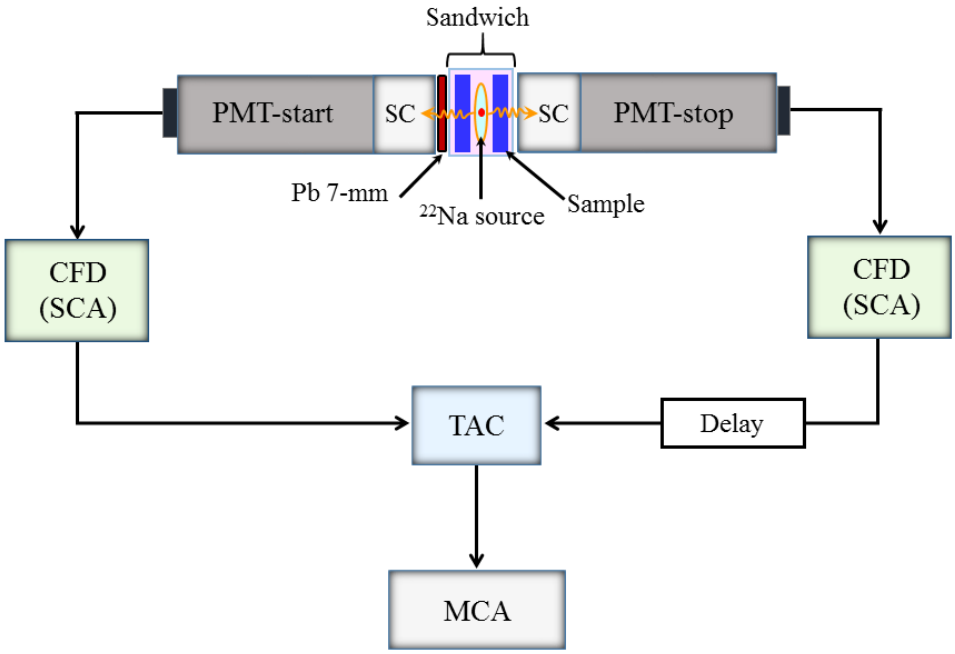

Figure 12. The "fast - fast" coincidence PALS system. SC - scintillator crystals, PMT - photomultiplier tubes, CFD - constant fraction discriminator, TAC - time-to-amplitude convertor, MCA - multi-channel analyzer.

3.3.1.1 Detection System

The detection system consists of Hamamatsu (H3378-50) photomultiplier tubes coupled with either BaF_2 (Ø40 mm × 12 mm) or EJ-232 plastic scintillators (Ø35 mm × 20 mm). Two detectors were placed closely in a co-linear geometry with the sandwich in-between to allow for a maximum count rate.

- Scintillators

Atoms and molecules are excited when incoming gamma rays pass through the scintillator material. As a result of the de-excitation, i.e. the relaxation from the excited state to lower states, the absorbed energy can be re-emitted in the form of scintillation. In this work, barium fluoride (BaF_2) and plastic scintillators were used:

- BaF_2: The high Z (atomic number) material of BaF_2 was used not only due to its precision in fast timing measurements (0.6 ns decay time of the fast scintillation component), but also due to its high efficiency in γ detection. Correspondingly, the pronounced photoelectric peak simplifies the determination of the energy window by using an analog oscilloscope. However, care needed to be taken to avoid the backscattering of the 1.275 MeV photons. To minimize this disturbance, a Pb plate (7 mm thick) was placed in front of the start detector [46, 47].
- Plastics: Plastic scintillator was also used in this work, benefiting from its fairly high light output (8.4 photons/keV [48]) and relatively quick signal (decay time > 1.4 ns [47]). However, instead of the photoelectric peak, the ^{22}Na spectrum is dominated by the Compton scattering, thus, making the energy window selection based on oscilloscope observation difficult.

- Photomultipliers

Whenever incident photons hit the photocathode, electrons are emitted as a consequence of the photoelectric effect. Such electrons are directed by the focusing electrode and accelerated towards the dynodes. Upon striking the dynodes, electrons are multiplied due to the secondary emission. Finally, a considerable amount of electrons reach the anode, resulting in an easily-detectable current pulse at the output. To ensure a high light transmission between the scintillator and the photomultiplier (PMT), silicon grease was used as coupling material.

3.3.1.2 Signal Processing with NIM-Standard Electronics

Output pulses from the PMTs are processed by the NIM-standard electronics, consisting of two constant fraction discriminators (CFD), a time-to-amplitude converter (TAC) and a multi-channel analyzer (MCA) [46]:

- CFD

The Fast ComTec 7029A CFD was used to process the output pulses from the PMTs. The fluctuation in amplitude and/or rise time ("time walk"[46]) of the output pulses could affect the time resolution of the system. Particularly for the signals with equal rise times but different amplitudes, the CF timing technique was applied to generate walk-free timing signals at a constant fraction of the peak height where the trigging time will be no more depends on the amplitude of the signal. In addition, the integrated single-channel analyzer (SCA) provides fast signal discrimination. The incoming signals are identified according to the specified energy windows for the start and stop signals.

- TAC

An Ortec 567 TAC is a unit trigged by the start signal and stopped by the stop signal from the CFDs. It converts the time interval between the start and stop pulses into a new pulse with an amplitude proportional to its duration.

- MCA

The output signals from the TAC are then stored by a Fast ComTec MCA-3A multi-channel analyzer according to their amplitudes (energies, channels). Counts registered in different channels are accumulated to build up the energy spectrum [46].

3.3.1.3 Channel Width Determination

The "delay line" method was applied to calculate the time corresponding to each channel. By using different delay lines (different lengths), a set of peaks of the prompt curve can be measured. The delay time versus the corresponding channel number can be plotted and then the channel width can be determined. In this work, the channel width equals 0.0253 ns/channel.

3.3.1.4 Data Treatments

- Data Acquisition and Processing

The spectrometer equipped with BaF_2 scintillators was mainly used to obtain the course of the one-component (1C) positron lifetime since for this its resolution of 245 ps was sufficient. A ^{22}Na source of ~15 µCi activity was used and the achievable count rate was 350-400 s^{-1}. The second spectrometer with plastic scintillators had a resolution of 193-203 ps and a count rate of about 800 s^{-1} using a stronger source (~45 µCi), which enable the decomposition of the spectra into various components.

Data sets were stored once every minute and later summed up to spectra representing longer times to provide the better statistics needed for lifetime decompositions. Usually, data representing 3-4 min (~10^5 counts) were summed up for one-component analyses, and every 15-30 min for positron lifetime decompositions (~5×10^5 counts), see Appendix A.2. Moreover, a cryostat enabled experiments at low temperatures to suppress the microstructure changes during the measurement [9, 49]. For the experiment in which the sample kept at –30 °C throughout measurement, ~2×10^6 counts were accumulated (count rate 80 s^{-1} due to larger detector spacing in cryostat), see HT-2 in Figure 7.

- Data Analysis

Data analysis was done using programme LT9 [50]. Pure annealed Al was used to obtain the positron source contributions to the spectra, which amount to ~11% with a ~400 ps component from the Kapton foil and the sodium salt [51-53] and <1% with ~3 ns from positronium formation [52, 53]. These source contributions were subtracted from the spectra. Analysis started by fitting only one component, yielding lifetime τ_{1C}. Another component can be added in two-component fits. To ensure the reliability of such an approach, the fitting residual and fit variance were required to improve after the addition of a further component [38, 54]. Moreover, the fitting procedure was required to be stable and independent on the starting conditions in a sensitive way and the average lifetime calculated from the decomposed component was required not to deviate from the one-component lifetime τ_{1C} by more than 10 ps. The good resolution of the spectrometer used allowed

for a two-component analysis with three free parameters (two lifetimes and one intensity) in some cases, more easily for alloy 4-4 than for alloy 6-8.

The measured positron lifetimes are labelled by numbers τ_i in the order of increasing lifetime, the corresponding intensities I_i. As we will later argue that the longer lifetime component contains two (unresolved) components we will adopt the notation τ_1 and τ_{2+3} for the two measured components:

$$I_{2+3} = I_2 + I_3 \,, \tag{3.1}$$

$$\tau_{2+3} = \frac{I_2}{I_{2+3}}\tau_2 + \frac{I_3}{I_{2+3}}\tau_3 \,. \tag{3.2}$$

The former then correspond to annihilation in the reduced bulk, the latter in solute clusters and in vacancy-related defects.

Thus, Eq. (2.12) can be re-written as:

$$\bar{\tau} = \tau_1 \cdot I_1 + \tau_2 \cdot I_2 + \tau_3 \cdot I_3 \,. \tag{3.3}$$

3.3.2 Microhardness

A Vickers microhardness tester (MHT-10) was used applying a testing load force of 100 gf increasing with 10 gf/s and a dwell time of 10 s. 10 indentations were averaged to account for fluctuations due to heterogeneities in the samples.

3.3.3 Electrical Resistivity

About 350-mm long wires were used to make a coil of about 7 turns before heat treatment. Four-point measurements were carried out on the coiled wire of the sample. A constant current of 100 mA was applied while the voltage was measured by a Keithley multimeter.

Two types of measurements were carried out:

In one, the sample coil of previously NPA alloy was RA in liquid metal for a given time, after which it was transferred into an oil bath kept at 20 °C while continuously measuring the resistivity change for 2 weeks.

In another experiment, the NPA coil was RA for a given time, after which it was transferred to liquid nitrogen where the resistivity was measured. Then, RA was repeated for a given time and the process was repeated. Absolute values for electrical resistivity were obtained for the accumulated RA times given by the individual RA treatments using measured wire cross sections and lengths.

3.3.4 Differential Scanning Calorimetry

Thermal analysis was done using a Netzsch 204 F1 Phoenix differential scanning calorimeter. Disc-shaped samples of 4.8 mm in diameter were used for both the alloy sample and the pure aluminium dummy sample put into the reference pan. The DSC chamber was pre-cooled to 0 °C prior to placing the sample inside, after which DSC ran at a constant heating rate of 10 K/min were performed from 0 – 400 °C. A baseline measured using two empty crucibles was subtracted from the measured curve. Still, small offsets and initial slopes were observed. Therefore, a linear slope from 20 °C to 100 °C was determined and subtracted for all the samples that did not show any sign of a reaction in this range.

4 Results

4.1 Artificial Ageing at 180 °C

4.1.1 State Immediately after Artificial Ageing (AA)

4.1.1.1 Lean Alloy 4-4

One-component positron lifetime. The evolution of the one-component positron lifetime (τ_{1C}) versus AA time in different heating media is shown in Figure 13.

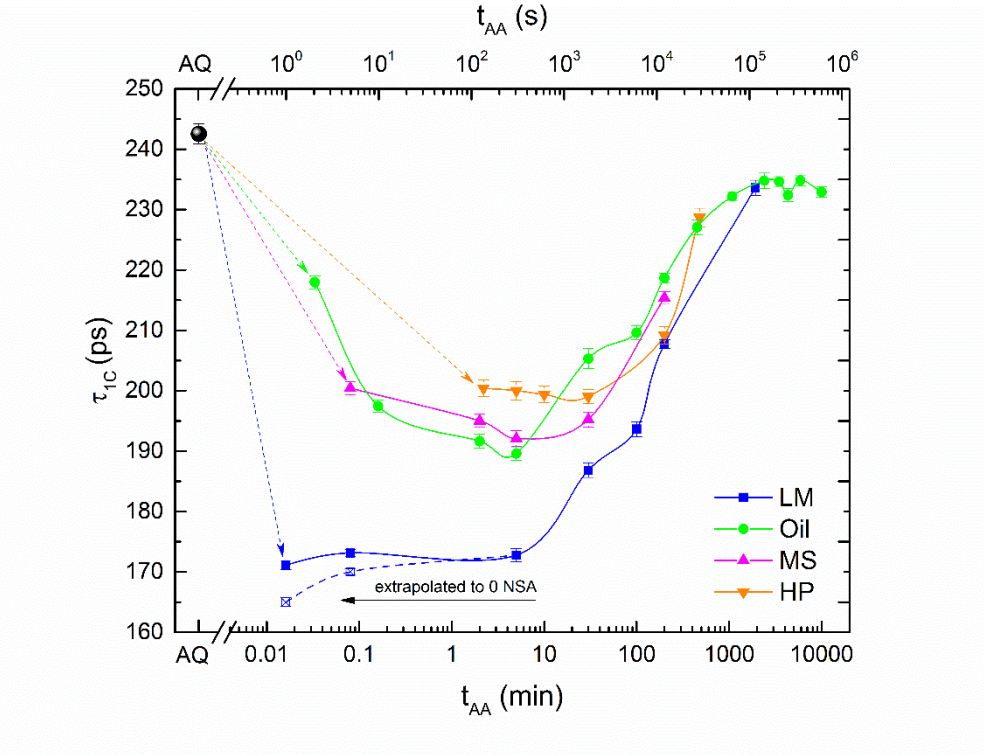

Figure 13. Evolution of the one-component positron lifetime $\boldsymbol{\tau_{1C}}$ in alloy 4-4 as a function of AA time in different heating media. Values represented by a dashed line and open symbols for short AA in LM have been extrapolated to zero NSA time to account for fast initial NSA in these cases during the first minutes of measurement derived from Figure 18.

The black point corresponds to the 'as-quenched' state (more precisely after ~2 min delay at RT due to sample preparation). The course of τ_{1C} depends on the medium used for AA. Fast heating in LM causes the shortest τ_{1C} ~172 ps for very short AA (1 s to 5 min). This is a reduction by 71 ps with respect to the value measured directly after quenching. AA up to 5 min changes τ_{1C} only slightly. In contrast, higher τ_{1C} were measured for intermediate-rate heating in oil with 218 ps and

197 ps after 2 s and 10 s, respectively, with a slight ensuing decrease up to 5 min of AA. The decrease caused by AA is therefore much lower than for fast heating. AA in MS for up to a few minutes yields similar results as AA in oil, and the results of AA for slow heating on the heating plate are also comparable. In all heating media, τ_{1C} starts to increase for longer AA. For 30 min of AA the increase is notable. A stable τ_{1C} is found after long AA time with ~235 ps as it seen for AA in oil.

Two-component positron lifetime. Figure 14a,b shows positron lifetime decompositions into two-components. Due to the good resolution of the spectrometer it was in many (but not in all) cases possible to decompose spectra into contributions (τ_1, τ_{23}) and the corresponding intensities (I_1, I_{23}).

Each value represents the state after AA and is based on data accumulated during NSA up to 15 to 30 min after quenching as long as τ_{1C} remained constant or slowly changing (data accumulation at RT, ~5x10^5 counts, see Sec. 3.3.1.4).

As for τ_{1C}, heating in LM (highest heating rate) leads to a different course than (the intermediate and slower heating rates) either in oil, MS or on the HP. Fast heating: 1 s in LM produces a high τ_{23}=234 ps and low I_{23}=34%. Upon increasing AA time, τ_{23} continuously drops to a minimum of 216 ps after 30 min of AA. At the same time, I_{23} increases to a value of 68%. A re-increase of τ_{23} to 235 ps is observed for even longer AA times accompanied by a slight further increase of I_{23}. τ_{1C} is almost constant for 1 s, 5 s and 5 min of AA (Figure 13 and Figure 15). This is a consequence of a compensation of a reduced τ_{23} (from 234 ps to 222 ps) by an increased I_{23} (from 34% to 40%). Intermediate and slow heating in oil, MS and HP: Short AA times (up to 5-10 min) yield I_{23} values about twice as high as for analogous AA in LM (Figure 14b). In contrast, the measured τ_{23} values are lower after AA than in LM. Most values are between 210 ps and 217 ps except for 5 s in MS (222 ps). Longer AA times (≥30 min) let τ_{23} increase to 235 ps with I_{23} eventually being between 70 and 85%.

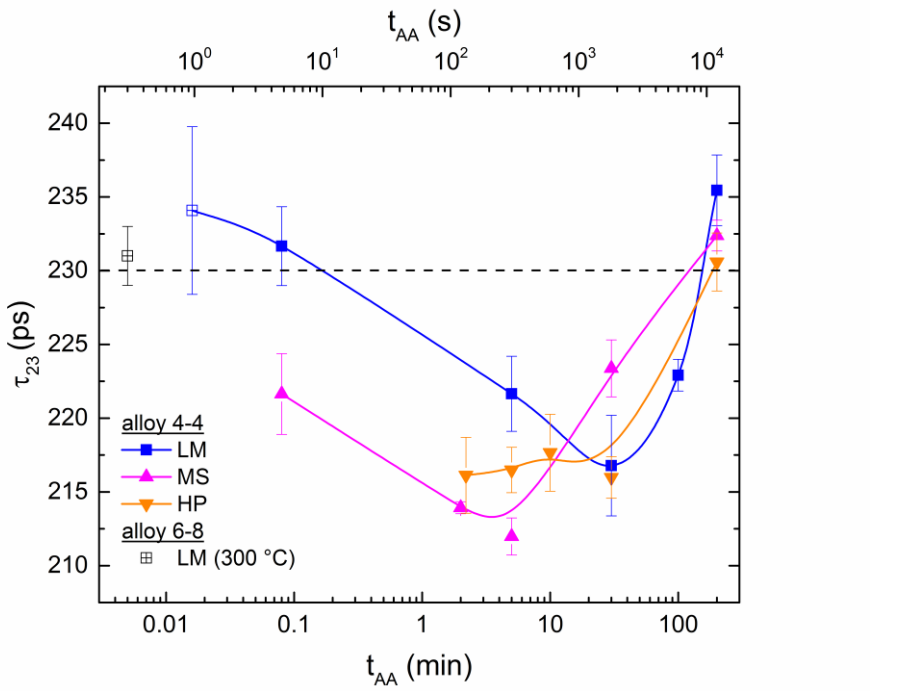

(a)

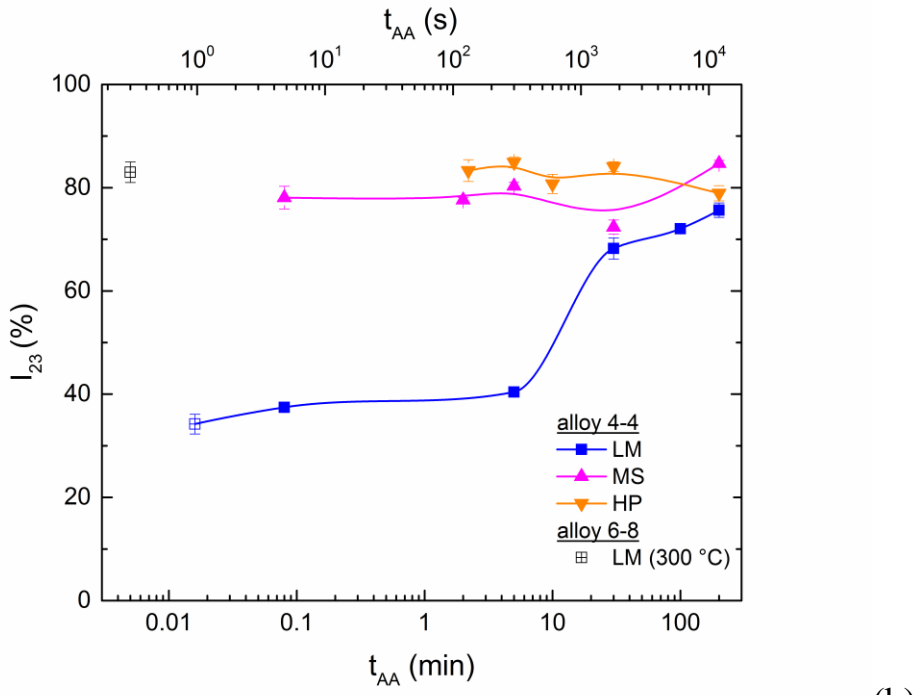

(b)

Figure 14. Trap component '23' as derived from positron lifetime decompositions for alloy 4-4 and 6-8. Different symbols specify the AA medium used. (a) Positron lifetime (b) Corresponding intensity. The value for alloy 4-4, 1 s in LM was measured at –30 °C (open symbols), all others at 'room temperature'. One value for alloy 6-8 and the value after quenching are also indicated.

Hardness. Figure 15 shows the evolution of hardness compared to that of τ_{1C} during AA in oil. A negligible initial change in hardness up to 2 min of AA is followed by an increase to a maximum of 70 HV after ~1000 min of AA. Overageing is observed for longer AA times. The main increase in hardness takes place after 30 min of AA, which is later than the increase of τ_{1C} starting already after 5 min of AA. Over-ageing reduces hardness, but not τ_{1C}.

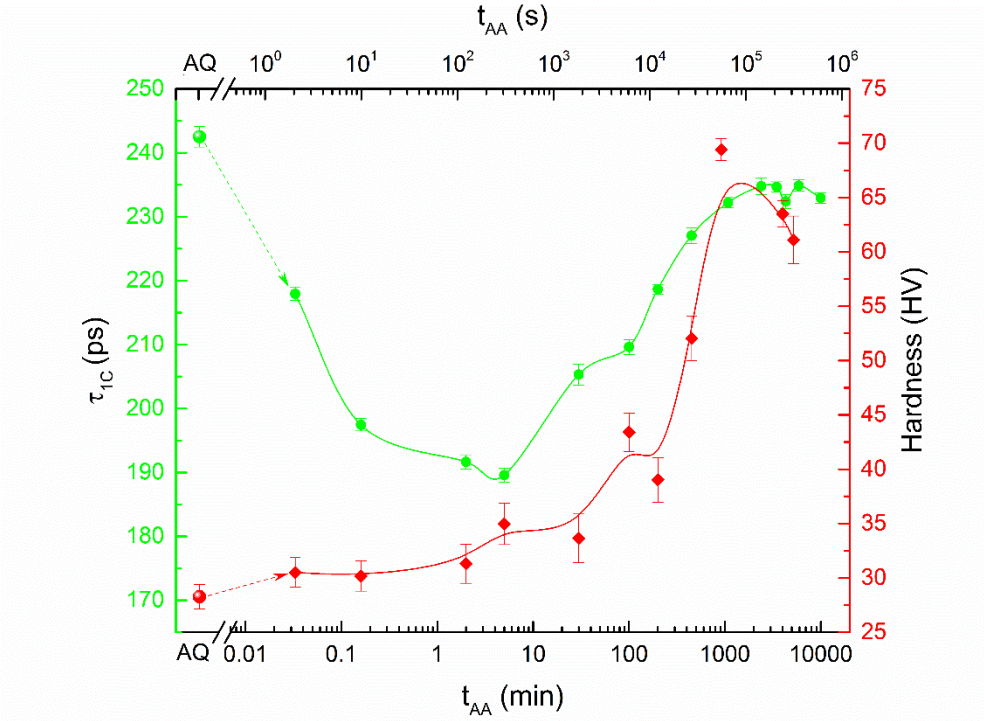

Figure 15. Analogue to Figure 13, τ_{1C} compared to hardness as a function of AA time in oil bath.

4.1.1.2 Concentrated Alloy 6-8

One-component positron lifetime. Figure 16 shows τ_{1C} of alloy 6-8 measured after AA in two media (LM and oil). 1 s of AA in LM decreases τ_{1C} by 32 ps compared to the AQ state, while for AA in oil for 2 s, τ_{1C} is reduced only by ~10 ps. Increasing the AA time leads to a continuous increase to 213 ps after 2 min AA in LM followed by a slight decrease to a minimum of 211 ps after 30 min AA, while a continuous decrease to a minimum of 209 ps after 30 min AA in oil is observed. Longer AA times (~3.5 days) cause an increase of τ_{1C} to a maximum of around 235 ps as in alloy 4-4.

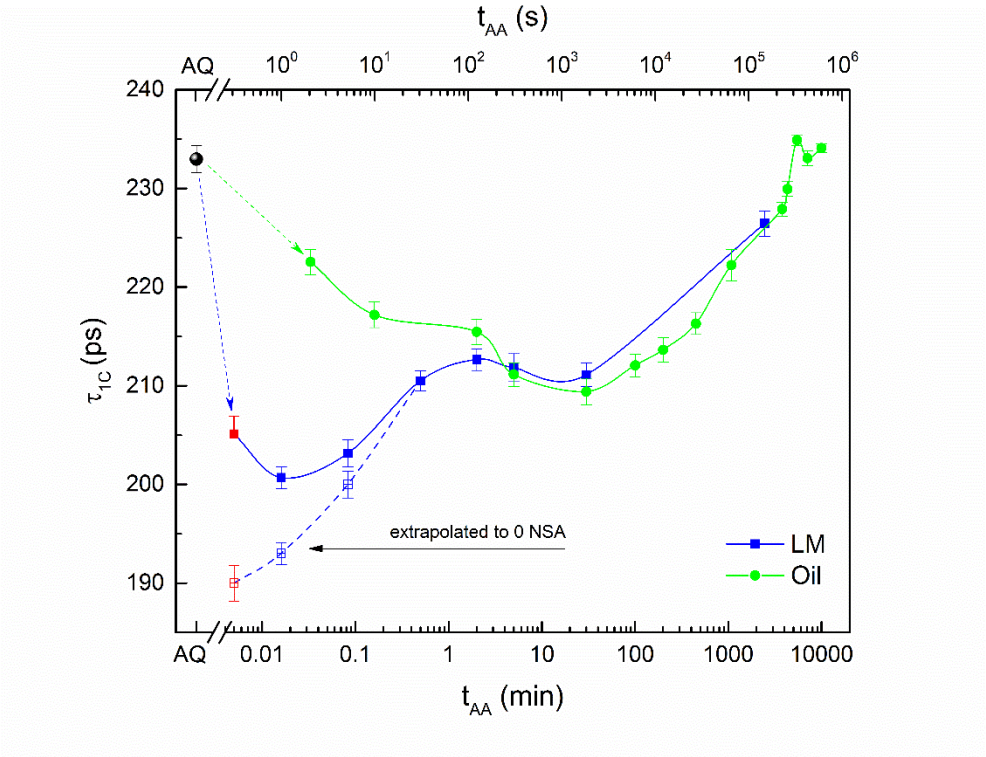

Figure 16. Evolution of the one-component positron lifetime τ_{1C} in alloy 6-8 as a function of AA time in different heating media. Values represented by a dashed line and open symbols for short AA in LM have been extrapolated to zero NSA time to account for fast initial NSA in these cases during the first minutes of measurement derived from Figure 21. The red symbols correspond to 0.3 s ageing at 300 °C.

An extra experiment was carried out by dipping a sample into LM held at 300 °C for ~0.3 s in order to achieve an even higher heating rate than in LM at 180 °C. The end temperature in this experiment was estimated to be around 200-230 °C. τ_{1C} after this treatment was shown to be slightly higher than after AA for 1 s at 180 °C (red points in Figure 16).

Two-component positron lifetime. Lifetime decompositions in alloy 6-8 are more difficult than in alloy 4-4, most likely because positron trapping is closer to saturation in most cases. Only in one case a lifetime decomposition satisfied the criteria given in Sec. 3.3.1.4: After AA for 0.3 s in LM at 300 °C a trap component τ_{23}= 231 ps, I_{23}=83% could be determined, see Figure 14a,b. The average lifetime using $\tau_1 = 70$ ps was 204 ps in this case, close to τ_{1C}= 202 ps.

Hardness. The hardening response (Figure 17) shows a negligible change during the first 2 min of AA in oil followed by a slight increase after 5 min AA. The further increase of hardness to 93 HV coincides with a minimum of τ_{1C} after 30 min of AA. A maximum of hardness was achieved after 100 min AA, followed by a plateau ranging between 109 and 114 HV up to ~15 h AA. Hardness

therefore peaks earlier than τ_{1C}, which takes 3.5 d of AA. Overageing for long AA times is pronounced.

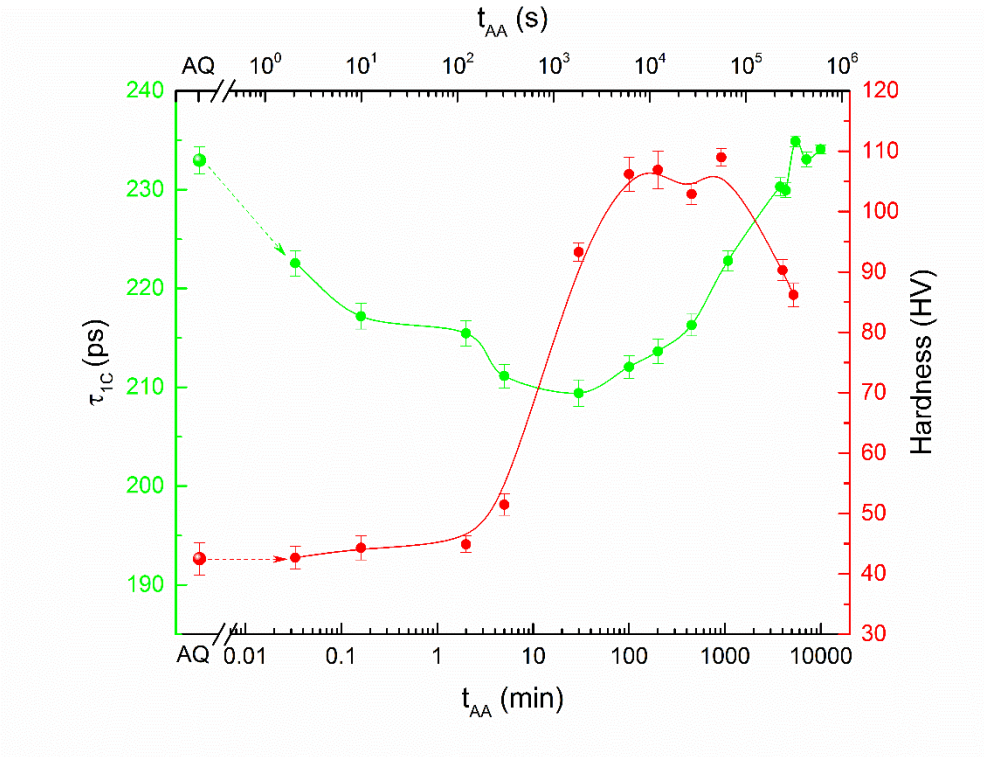

Figure 17. Analogue to Figure 16 τ_{1C} compared to hardness as a function of AA time in oil bath.

4.1.2 State during Natural Secondary Ageing (NSA)

4.1.2.1 Lean Alloy 4-4

One-component positron lifetime. Figure 18a-d shows the evolution of the one-component positron lifetime τ_{1C} during NSA after treating the samples in different AA media. τ_{1C} as it evolves during NA after quenching without any AA is given for comparison (black lines). The first values for short NSA reflect the data in Figure 13. Besides the similarities of the NSA evolution between the different AA media, the results differ in some details.

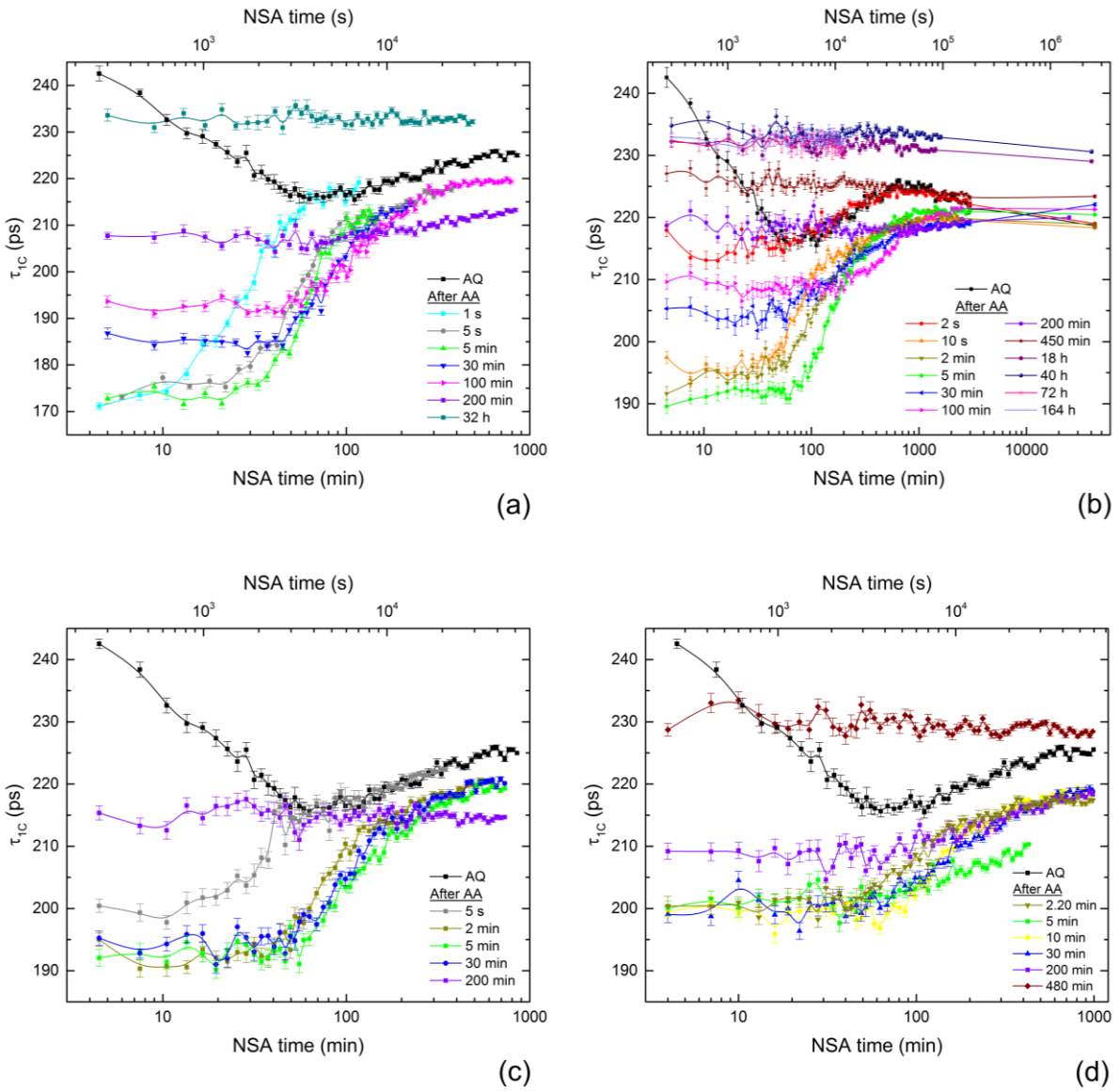

Figure 18. Evolution of τ_{1C} in alloy 4-4 during NSA after AA for various times in different heating media. (a) Liquid metal, (b) Oil bath, (c) Molten salt and (d) Heating plate. 'AQ' refers to the evolution of τ_{1C} during NA without preceding AA.

An increase of τ_{1C} during NSA was observed for samples aged up to 100 min in oil and MS, and for times up to 200 min in LM and HP. It is preceded by an incubation time during which the lifetimes increases only weakly, after which the increase sets in (as seen best on a linear time scale, not shown). The period of incubation varies according to the AA medium and AA time. For 1 s and 5 s of AA in LM, the incubation period can be as short as ~20 min during which there is a slight slope. Therefore, one can back-extrapolate to zero NSA time and obtain the values given in Figure 13. For 200 min of AA the incubation time is about 10 times longer. For intermediate and

slow heating in oil, MS and on the HP the incubation periods are about twice as long as for fast heating. In general, the incubation periods are difficult to determine precisely as the transition is spread out in time.

For 2 s of AA in oil, a maximum value is reached (long enough measurements available only for oil) after ~700 min, after which a slight decrease is observed. For intermediate AA times, τ_{1C} remains largely the same after 2 days up to 4 weeks. Longer AA times (≥450 min) in oil lead to a slight decrease of τ_{1C} by ~4 ps after long NSA time (from 1 day to 1 month).

The sample NA directly after quenching shows some similarity to the NSA experiments: the increase after the minimum and the decrease of τ_{1C} for long NA times. The initial decrease roughly corresponds to the incubation time of NSA.

Two-component positron lifetime. Figure 19 shows the decomposition of the measured positron lifetime into different components during NSA after 1 s AA in LM. Each point corresponds to 8 h of data accumulation time at −30 °C. This ensured a more reliable two-component composition into τ_1 and τ_{23}. The initial point immediately after AA (2 min NSA) and quenching has been explained previously (see Sec. 4.1.1.1). After 10 min of NSA, τ_{23} has increased to from 234 ps to 242 ps, while I_{23} remains the same. I_1 shows a slight decrease and τ_1 is stable. 30 min of NSA and even more 80 min of NSA reduce I_1 and τ_1, while τ_{23} decreases to 230 ps and I_{23} markedly increases.

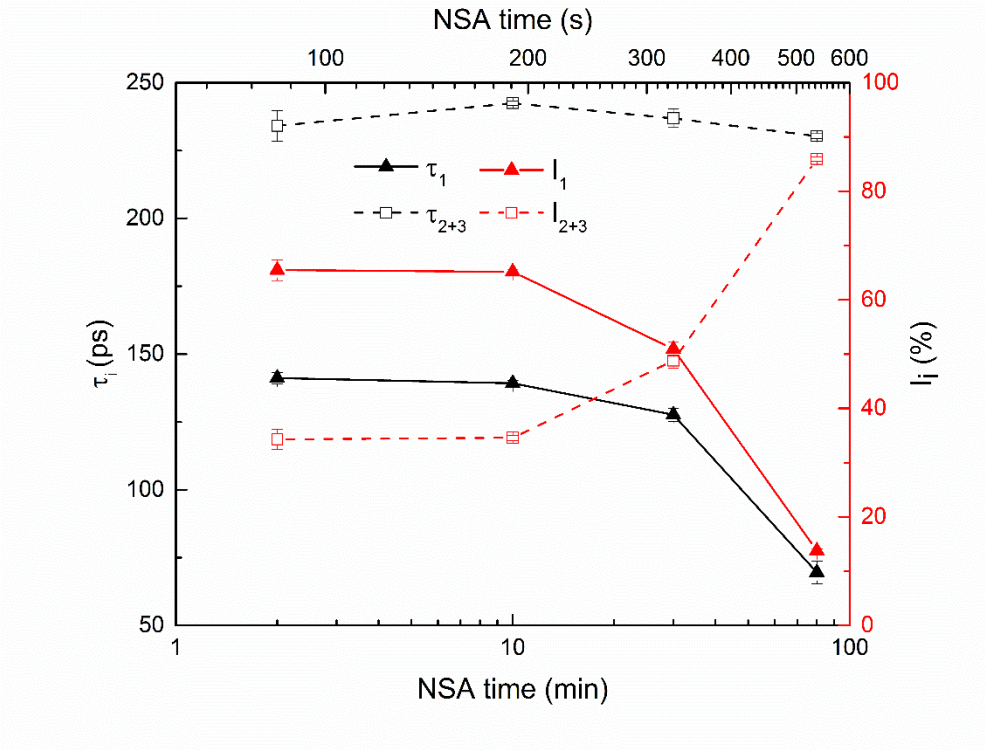

Figure 19. Measured positron lifetime components and corresponding intensities in alloy 4-4 during NSA after 1 s AA in LM. All the data were measured at –30 °C. NSA was done by heating the samples to 'room temperature' between measurements. The first NSA value (2 min) reflects the time needed to assemble the sandwich at 'room temperature'.

Hardness. Figure 20 shows the evolution of hardness during NSA after AA in an oil bath for different times. Hardness increases during NSA, which is the reason for the term 'secondary ageing'. Incubation times for hardening exist but are hard to determine precisely due to the small hardness changes and the experimental scatter. For different AA times, the incubation times lie between 100 and 1500 min during NSA. For up to 5 min AA, the hardness curves eventually are similar to the hardening curve without any AA (black line). For AA times between 30 – 200 min, the hardness curves start at higher values (caused by AA) and increase after, ending at similar values as for hardening without AA. After 450 min AA, hardness is further increased and no NSA is observed any more as for τ_{1C}.

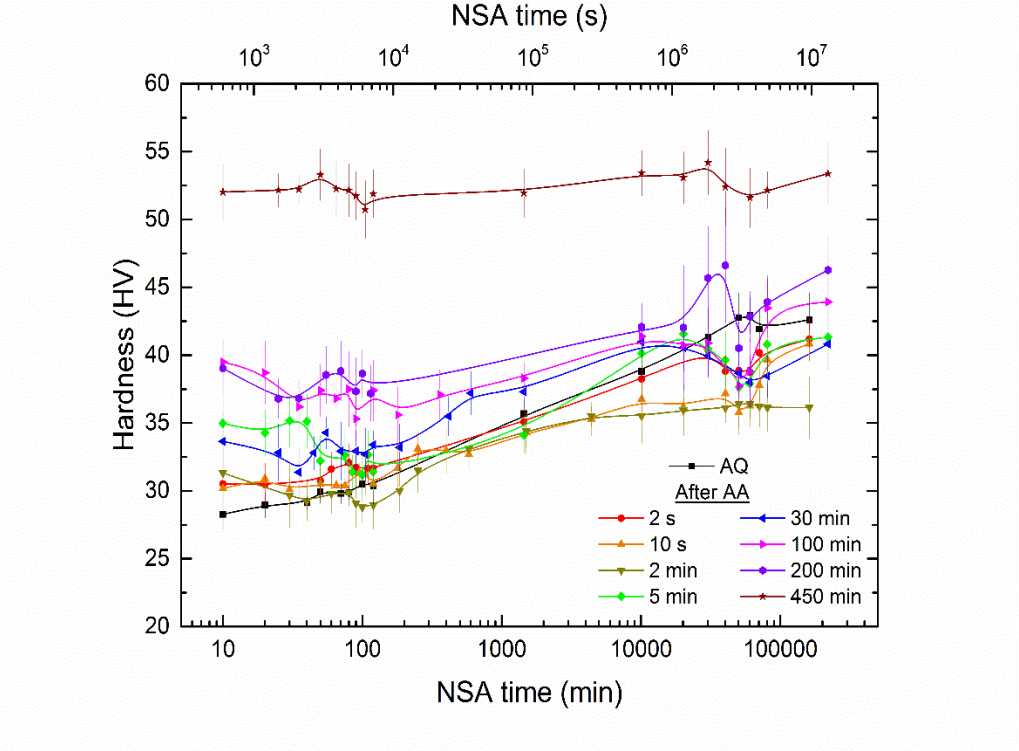

Figure 20. Hardness evolution in alloy 4-4 during NSA after different AA times in an oil bath.

4.1.2.2 Concentrated Alloy 6-8

One-component positron lifetime. The evolution of τ_{1C} in alloy 6-8 during NSA is presented in Figure 21a,b for two AA media (LM, oil) together with the reference curve for pure NA without prior AA. It differs markedly from those given for alloy 4-4 in Figure 18.

For 2 s AA in oil (Figure 21b) and even more AA for 1 s, 5 s, 30 s in LM (Figure 21a) (also in alloys 8-6, 4-10, 10-4 see Sec. 4.1.2.3), a pronounced increase of τ_{1C} to 231 ps (LM) and 225 ps (oil) is observed. The incubation time for AA in oil is very short (10 min), in LM, no incubation time can be resolved. A maximum is reached 20 to 30 min after AA. This increase is much faster and stronger than any increase observed for alloy 4-4. Compared to the NA curve (no AA, black), an overshoot is observed, i.e. the NSA curve not just simply approaches the NA curve but crosses it. The curves for short AA show a pronounced slope at the shortest NSA time given (caused by the time needed to prepare the sample and to acquire data) unlike in alloy 4-4 where the slope is smaller (Figure 18) and unlike for longer AA. τ_{1C} has been back-extrapolated to zero NSA time on a linear time scale and the corresponding values have been added to Figure 16 to express the state directly after AA.

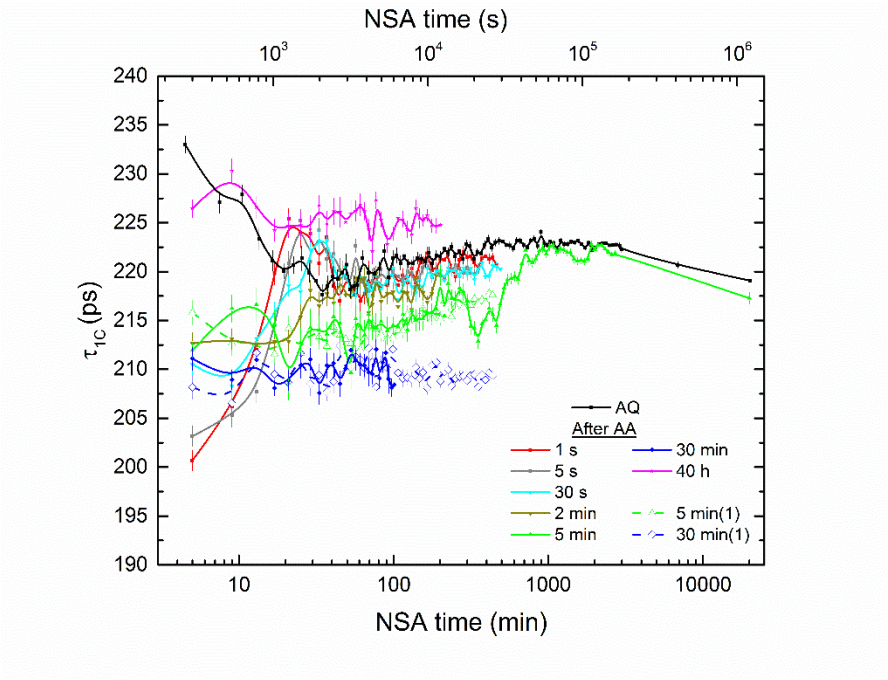

(a)

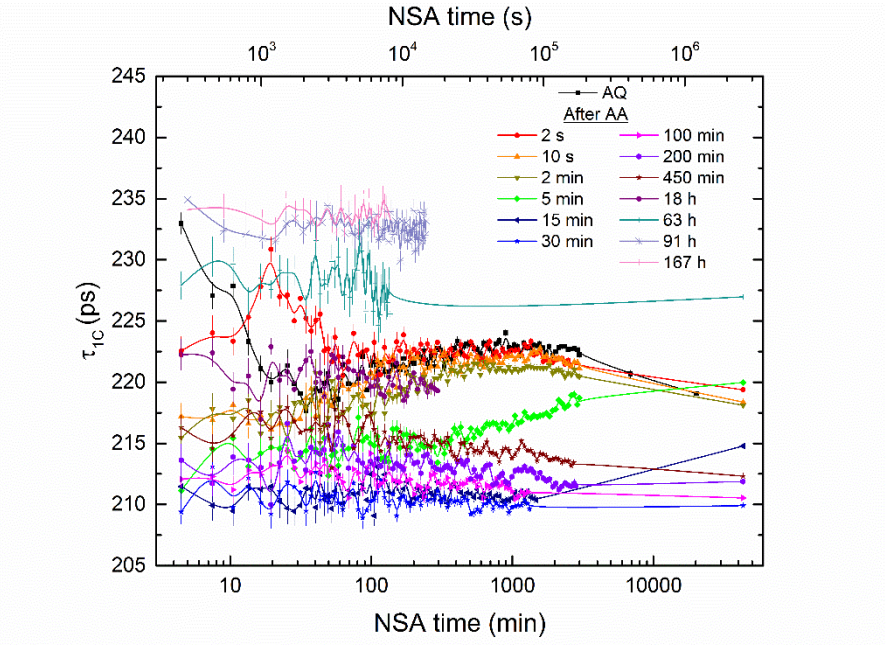

(b)

Figure 21. Analogue to Figure 18 for alloy 6-8. Two different heating media. (a) Liquid metal, (b) Oil bath. In (a), repetitions of 5 min and 30 min AA are shown as a check of reproducibility.

After dipping a sample into LM at 300 °C for about 0.3 s, the τ_{1C} value extrapolated to zero NSA as described in Figure 16 is slightly lower than after 1 s in LM at 180 °C. During subsequent NSA, however, τ_{1C} increases rapidly reaching a peak at 228 ps in just 13 min (see Figure 22). After the

peak has been reached, there is a decrease and a slight re-increase after in all these cases. The NSA curves eventually merge with the NA curve of the AQ sample.

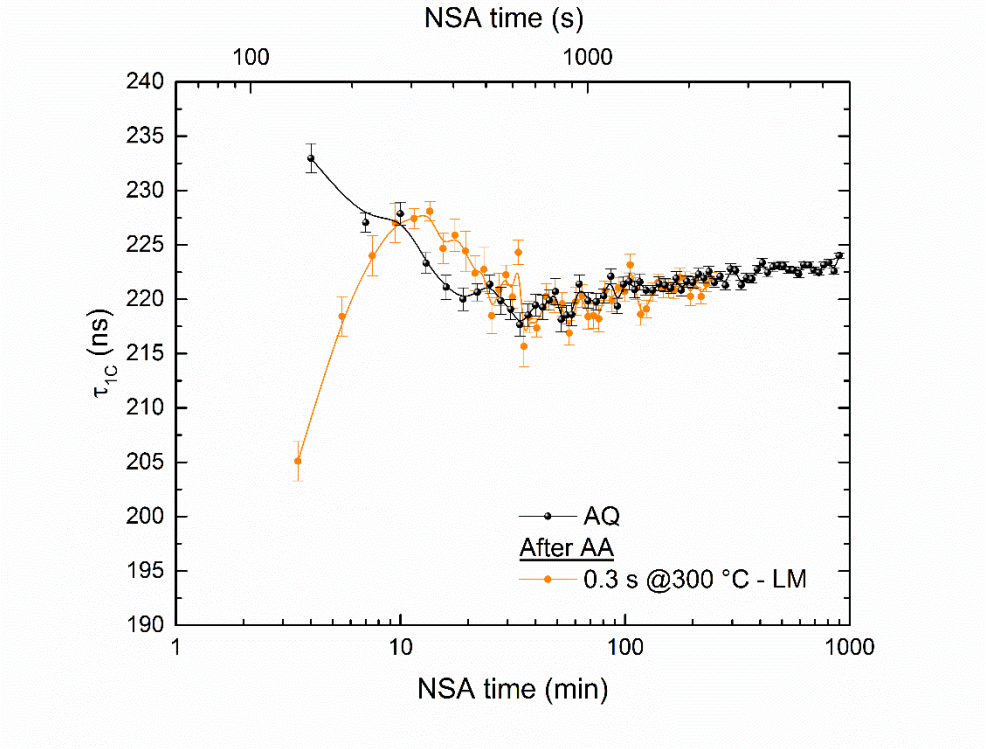

Figure 22. Evolution of τ_{1C} during NSA after 0.3 s AA in LM at 300 °C (orange). Curve for NA only (black) is given for comparison.

For longer AA times, 10 s to 5 min AA in oil and 2 min to 5 min AA in LM, no such fast increase is observable. Instead, after an incubation time, slow NSA is observable during which τ_{1C} approaches the NA curve. Moreover, NSA for AA in oil and LM is almost the same for AA times longer than 2 min. The rate of change of τ_{1C} during NSA slows down rapidly with increasing AA time by a factor of 12 from 10 s to 5 min (unlike in alloy 4-4 where slowing down is much less pronounced). After 30 min of AA in oil, no NSA is observed within a month.

Two-component positron lifetime. The only reliable two-component lifetime decomposition was that of the sample AA for 0.3 s at 300 °C, see Sec 4.1.1.2. During NSA, the trap component I_{23} rises from 83% after 5.5 min of NSA to 92% after 10 min of NSA. After 30 min of NSA, saturated trapping occurs (I_{23} ~100%).

Hardness. Figure 23 shows the hardness response for alloy 6-8 during NSA after various AA times in an oil bath. The sample AA for 2 s shows a similar behaviour as the sample NA without AA,

namely a stage of increase within the first 100 min, a slowing down (even on the log. scale) after and an approach to the final hardness of ~72 HV. A prolongation of AA from 10 s to 2 min increasingly leads to a stage of incubation (slower hardness increase) within the first 100 min, but to a similar slope after. 5 min of AA have already slightly increased the initial hardness. Subsequent NSA resembles the course for 10 s to 2 min AA. Even longer AA times let the NSA curve start at even higher hardness levels. During NSA, hardness scatters around an approximately constant value up to 1 year of NSA.

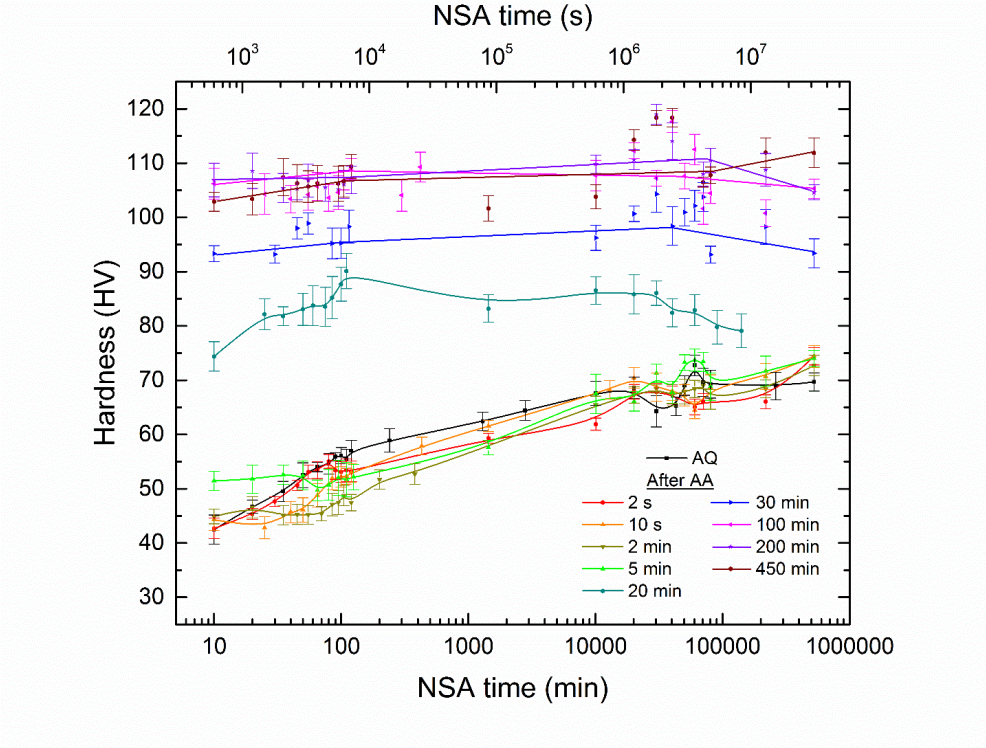

Figure 23. Analogue to Figure 20 for alloy 6-8.

4.1.2.3 Other Alloys (4-10, 5-5, 8-6, 10-4)

Figure 24 compares the course of τ_{1C} during NSA after 1 s AA in LM for various alloys with different Mg and Si contents. The data for alloys 4-4 and 6-8 from Figure 18b and Figure 21b are reproduced. Alloy 5-5 shows a similar trend as alloy 4-4, but the initial τ_{1C} is higher and NSA faster. No overshoot is observed. In the higher-solute content alloys 4-10 and 8-6 the evolution is very similar to alloy 6-8. Overshoots after 20 to 30 min are observed. The overshoot is most pronounced in alloy 8-6. Alloy 10-4 shows a very late increase of τ_{1C} after an incubation time of ~30 min and a peak only after 80 min. All the high-solute alloys start from initial τ_{1C} values

between 196 ps and 200 ps. For all the alloys, the curves merge after prolonged NSA at values of 222 ps to 225 ps. Phenomenologically the alloys with the lowest Si content (0.4%) show the latest increase of τ_{1C}, followed by alloy 5-5 (0.5%) and the other alloys (≥0.6%).

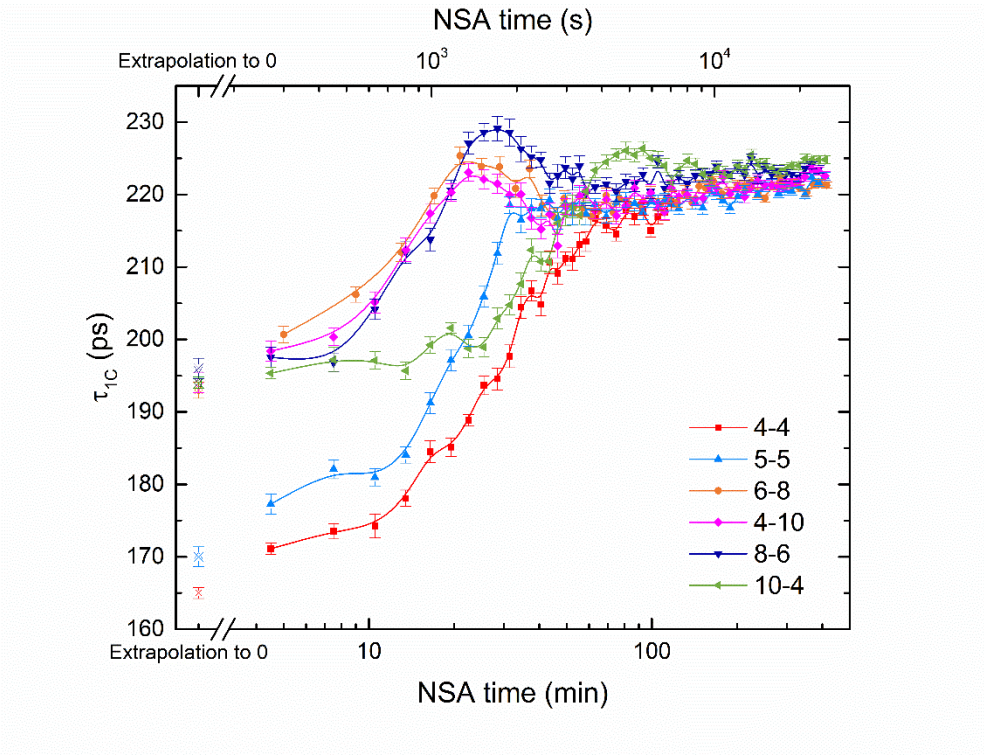

Figure 24. Evolution of τ_{1C} during NSA after 1 s AA in LM. (a) In different alloys with different Mg and Si contents. Data for alloys 4-4 and 6-8 is the same as in Figure 18a and Figure 21a, respectively.

4.1.3 Influence of a Natural Pre-Ageing (NPA) Step before AA

Figure 25 presents the evolution of τ_{1C} in alloy 4-4 during NSA after a combination of a NPA step (5, 30, or 80 min) and short AA for 1 s in LM. The curves corresponding to pure NA (black) and 1 s AA without prior NA (red) were added for comparison. 5 min of NPA leads to an increase of the initial τ_{1C} immediately after AA by ~5 ps compared to the AA only curve. Only after 25 min NSA, the curves merge together. 30 min of NPA have a stronger effect on the AA and NSA response. τ_{1C} is now 193 ps after AA, 21 ps higher than without NPA. The curve merges with that without NPA after 40 min. 80 min of NPA have the largest impact. The initial τ_{1C} after AA is equal as for 30 min of NPA, but the subsequent response to NSA is much slower. All the curves except for 80 min NPA merge with the NA curve after ~70 min NSA, while the curve for 80 min NPA will possibly merge outside the range of the experiment.

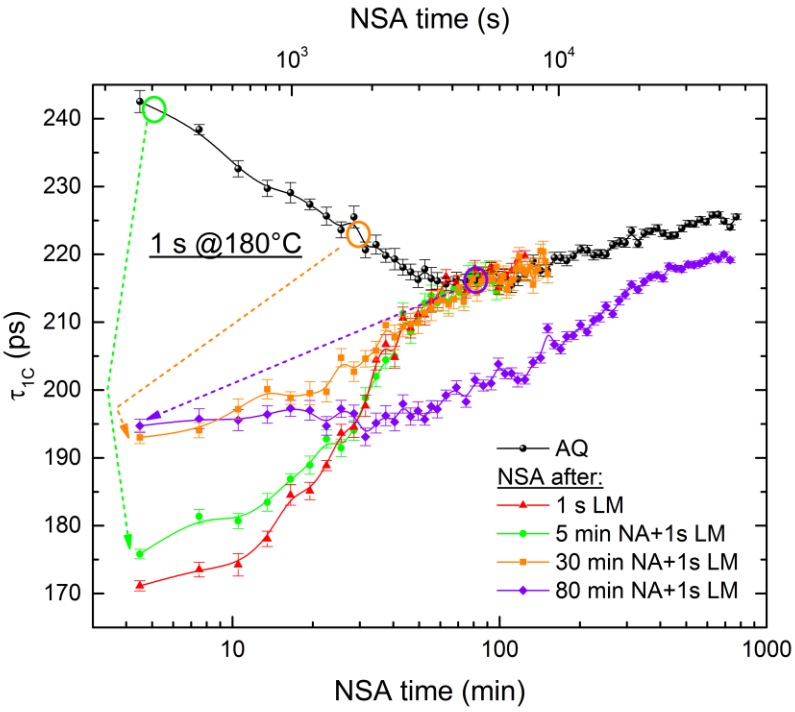

Figure 25. Evolution of τ_{1C} during NSA in alloy 4-4 after NPA step (5, 30 or 80 min) and 1 s AA in LM. Curves for NA only (black) and NSA after AA only (red) are given for comparison. Dashed lines indicate changes during AA.

4.2 Reverse Ageing at 250 °C

4.2.1 Hardness (HV)

Vickers hardnesses as measured directly after RA and during NSA are given in Figure 26, Figure 27 and Figure 28, respectively.

Hardness after solutionising and quenching is about 42.5 HV. 2 weeks of N(P)A increase hardness to 68.5 HV (Figure 26) . This is the starting point for RA experiments (dotted horizontal line in Figure 27 and Figure 28).

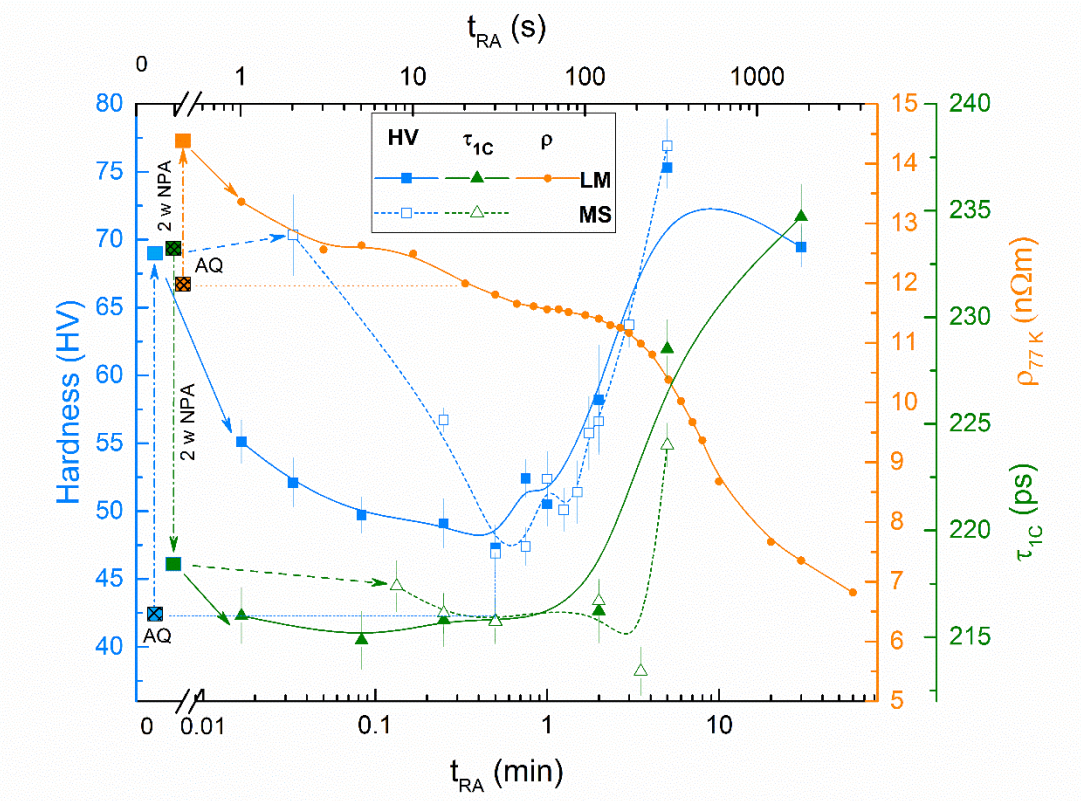

Figure 26. The evolution of hardness (blue, left axis), electrical resistivity (orange, right axis) and one-component positron lifetime (green, right axis) as a function of RA at 250 °C for various times. The two HV and $\boldsymbol{\tau_{1C}}$ lines, solid and dashed, correspond to RA in liquid metal and molten salt, respectively. The electrical resistivity measurements were carried out 'ex-situ' at liquid nitrogen temperature. The values for $\boldsymbol{\tau_{1C}}$were calculated by averaging the values for less than 100 min NSA in Figure 29 and Figure 31. The HV values are the initial data points (each corresponds to 10 indentations) immediately after RA and quenching in Figure 27 and Figure 28. The AQ-state (hatched symbols) and the state after 2 weeks of NPA (full squares) are also given.

4.2.1.1 Liquid Metal

The sample RA for 1 s shows a decrease of 13 HV upon RA compared to the NA state (Figure 26). During subsequent NSA, hardness is largely constant for about 2 weeks, after which it increases (Figure 27). 2 to 5 s RA further decrease hardness. During NSA, hardness is constant for ~1 week and ~500, respectively, after which it starts to increase. 15 – 30 s RA further decrease hardness and a minimum is reached after 30 s RA. The NSA hardness response is the highest, featuring a ~14 (~18) HV increase during 2 weeks of NSA. The increase is preceded by a stage of constant hardness for ~300 (~95) min. After 2 min RA, hardness is larger than after 30 s. Hardness during NSA increases from this elevated level to almost the NA hardness after an incubation time of ~120 min.

5 min RA has further increased the HV. During 2 weeks of subsequent NSA the value no longer increases.

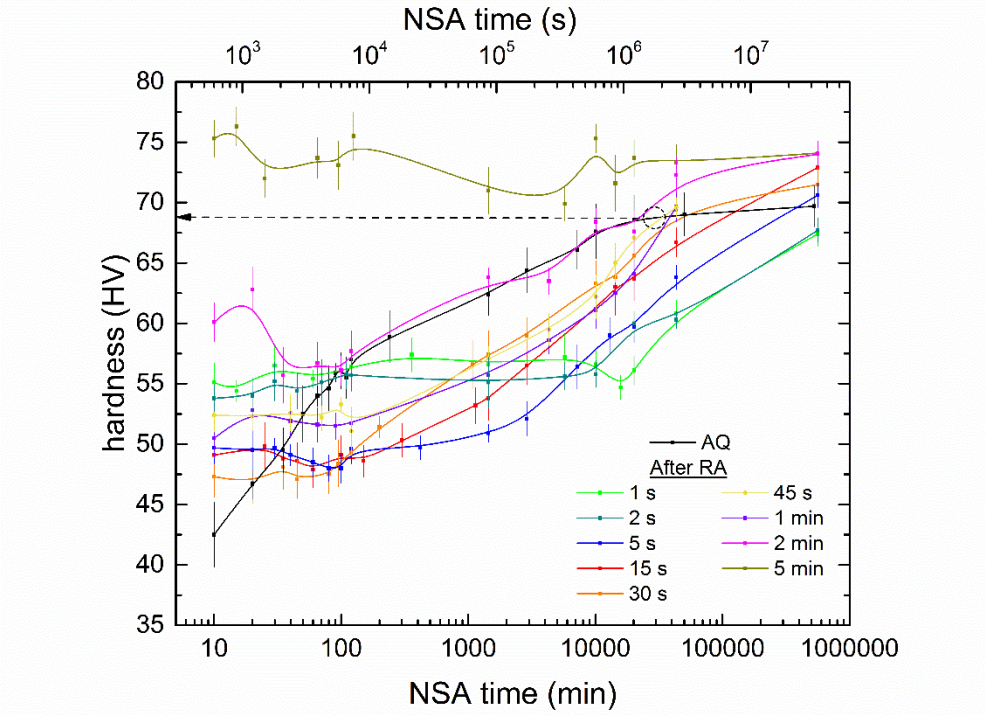

Figure 27. Course of hardness evolution during NSA after RA for various given times in liquid metal. Black curve 'AQ' refers to NPA without prior RA. The horizontal dotted arrows indicate the states after 2 weeks of NPA which serve as starting points for the RA experiments.

4.2.1.2 Molten Salt

After 2 s of RA, hardness has slightly increased (Figure 26), but no changes are observed during NSA (Figure 28). 15 s RA has decreased HV. Still, no NSA is observed. 30 s RA has decreased HV to a minimum and NSA is now observed. A prior 'incubation' time is observed, but no exact period of the incubation can be given due to fewer measured points during NSA. 1 – 2 min RA have increased HV. During NSA, hardness increases to a value of ~67 HV after 2 weeks, which is close to the value of the NPA sample without prior RA. 5 min RA has further increased hardness to a value above the AQ-state. No more NSA response is observed.

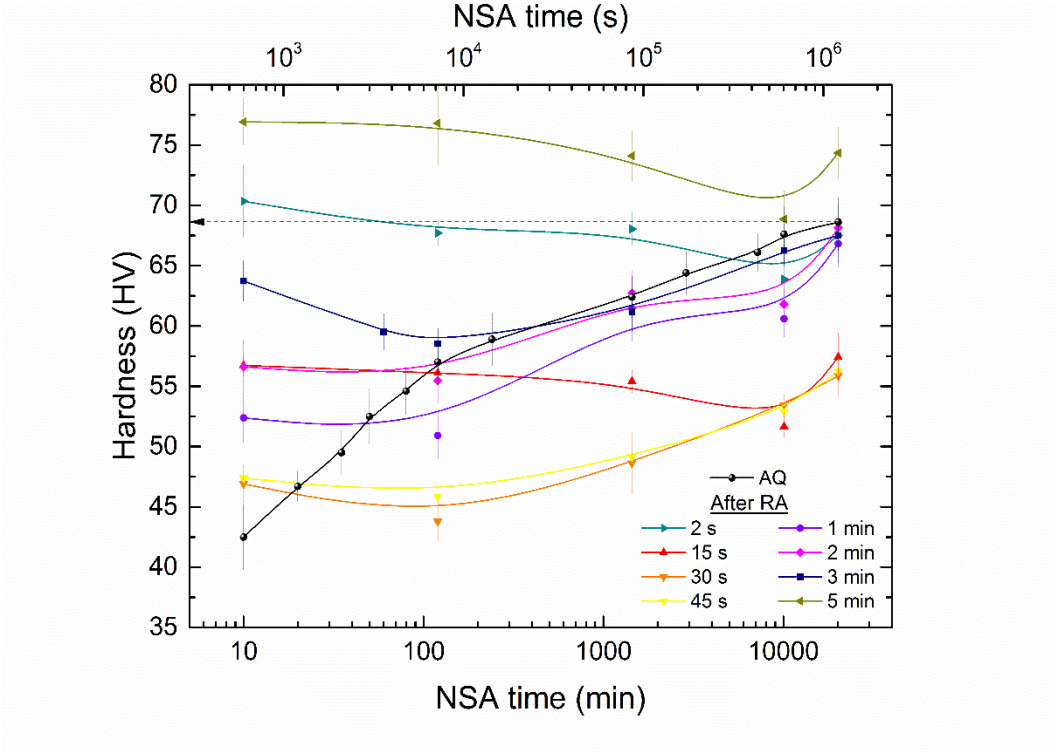

Figure 28. Analogue to Figure 27 in molten salt.

4.2.1.3 Comparison

For short RA times (2 s and 15 s) slower heating to 250 °C in MS yields pronounced differences to the curves aged in LM. For 30 s RA the difference is quite small.

The hardness increase in the AQ sample shows a similar slope as the samples RA for 30 s to 2 min in both baths for NSA times longer than ~120 min. Before this time, the strong and fast resistivity increase in the AQ sample is unmatched by the samples RA for any time.

4.2.2 One-component Positron Lifetime

The one-component positron lifetime after RA is shown in Figure 26, the evolution during NSA in Figure 29 and Figure 31. During NPA after solutionising and quenching, τ_{1C} varies in a complex way starting from a high value of 232 ps, decreasing within 45 min to 218 ps, re-increasing within 700 min to 224 ps, after which another decrease leads to a τ_{1C} = ~219 ps after 2 weeks at 'room temperature'. This is the starting point for subsequent RA treatments (horizontal dashed lines in Figure 29 and Figure 31). After 20 months of NPA the lifetime decreases slightly by another 1 ps (not shown in figure), which seems to be an asymptotic value.

4.2.2.1 Liquid Metal

After 1 s RA, τ_{1C} has decreased to a value below ~216 ps (Figure 26). No or only very slight changes are observed during 2 weeks of NSA (Figure 29). 5 to 15 s RA have reduced τ_{1C} to ~215 ps. A slight increase during NSA is observed after ~1000 and 600 min, respectively. After 30 s to 2 min RA, τ_{1C} still ~216 ps, while NSA now leads to a pronounced increase and then decrease of τ_{1C}. A maximum of τ_{1C} is observed after 1600 min (1200 min) of NSA for 30 s (2 min) RA, respectively, with τ_{1C} values of 221 ps (224 ps). The 2 min curve has merged with the NPA curve at its maximum, while the 30 s curve is lower by ~3 ps. After the maximum has been reached, a stage of re-decrease in a similar trend of the AQ-state during NPA is observed. In both cases there is an incubation time for the increase of τ_{1C}: 250 min for 30 s RA and 150 min for 2 min RA. Longer RA time (>5 min) increase τ_{1C} and no more changes are found during NSA for 2 weeks. For 30 min RA, τ_{1C} ~235 ps exceeds the AQ value.

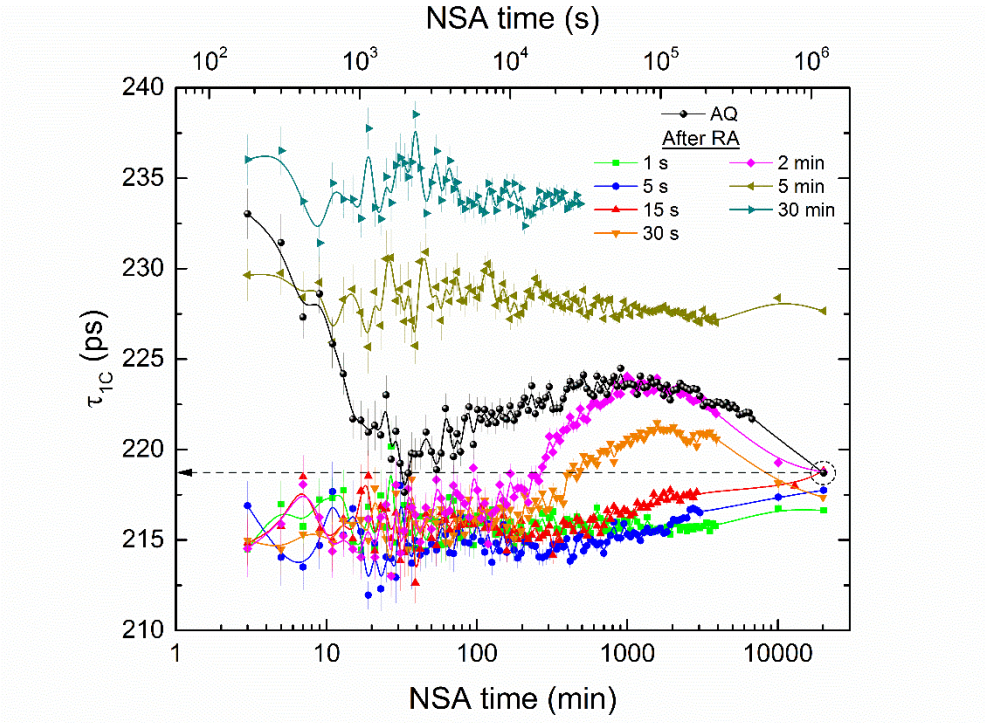

Figure 29. One-component positron lifetime (τ_{1C}) evolution during NSA after RA for various given times in liquid metal. Evolution of τ_{1C} during NPA without prior RA is referred to as "AQ". The horizontal dotted arrows indicate the states after 2 weeks of NPA without prior RA that are the starting points of the NSA experiments.

Figure 30 shows that τ_{1C} (T) measured at low temperatures shows a differing temperature dependence. It is rather weak in the NPA state, increases to a maximum directly after 2 min RA, after which it goes back to the originally weak dependence during NSA for up to 2 weeks.

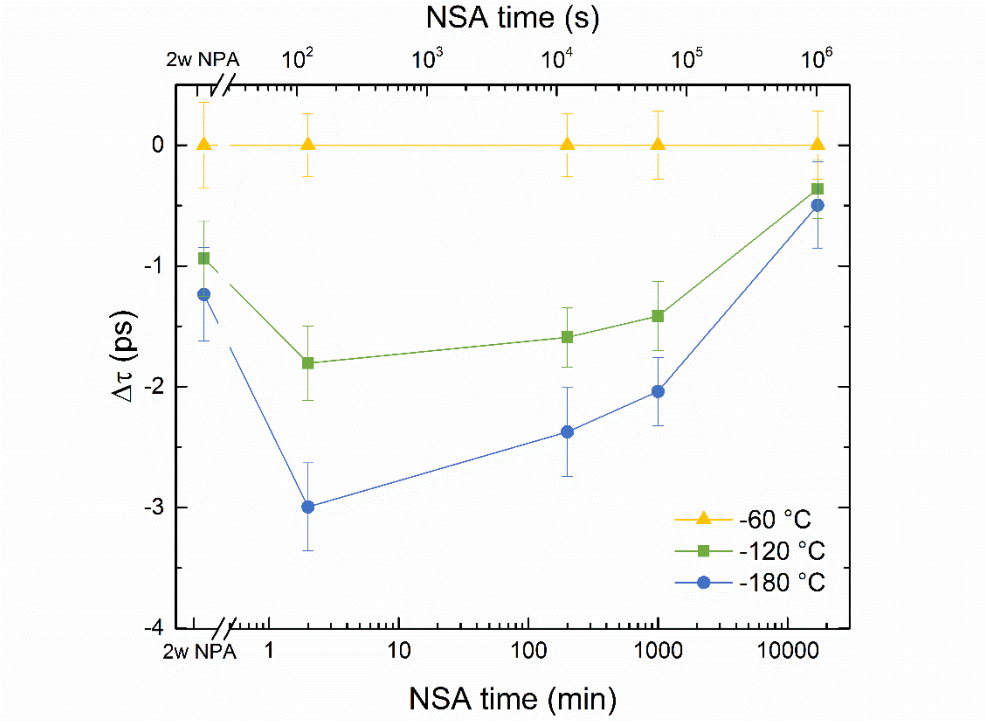

Figure 30. Temperature dependence of $\boldsymbol{\tau_{1C}}$ at 3 different temperatures in 5 different ageing states. First point corresponds to the state of 2 w NPA without prior RA. The following points correspond to the state after 2 min RA at different NSA times (first point corresponds to stage immediately after RA and ice water quenching, plus 2 min at RT for sample preparation). During NSA between low-temperature measurements, $\boldsymbol{\tau_{1C}}$ was measured continuously at room temperature. The temperature dependence of the measurements is shown as a relative change with respect to the reference temperature -60 °C, i.e. $\Delta\boldsymbol{\tau_{1C}}\,(\boldsymbol{T}) = \boldsymbol{\tau_{1C}}(\boldsymbol{T}) - \boldsymbol{\tau_{1C}}(\boldsymbol{-60\ °C})$.

4.2.2.2 Molten Salt

After 8 s of RA, τ_{1C} is similar (~217 ps) to τ_{1C} after 2 weeks NPA without prior RA. During NSA, τ_{1C} is stable. 15 s RA decrease τ_{1C} slightly to 216 ps. There is still no change during NSA. 30 s to 2 min RA lead to a similar behaviour as in LM: the initial value after RA is 216 ps but after an incubation time of ~300 min and ~120, respectively, τ_{1C} increases and goes through a maximum. After 3.5 min RA, τ_{1C} fluctuates up to 300 – 400 min NSA, then starts to increase to a maximum of 220 ps after ~2000 min. The re-decrease stage observed for 30 s – 2 min RA is now replaced by a constant stage. 5 min RA increases τ_{1C} and no more NSA response is observed. The transition time between the increase in NSA and the end of NSA response is ~3.5 min RA.

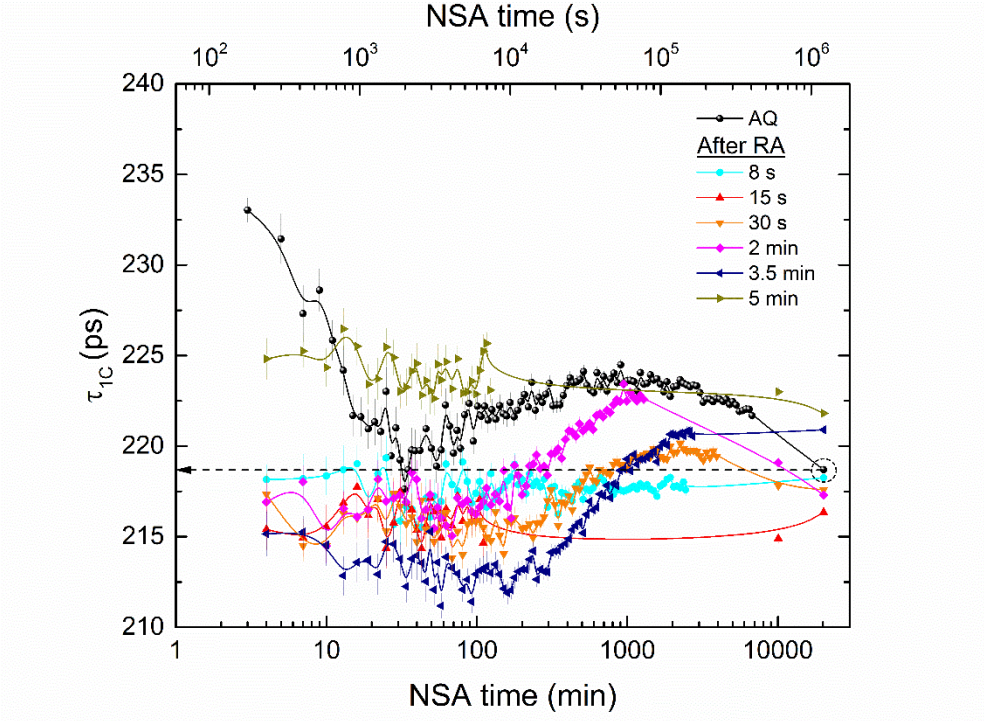

Figure 31. Analogue to Figure 29 in molten salt.

4.2.3 Differential Scanning Calorimetry (DSC)

The DSC curves obtained directly after quenching (AQ) exhibit an exothermal two-stage signal up to 125 °C (1,2), various endothermic troughs from 165 °C and 230 °C (4-6) and two exothermic precipitation peaks after (7,8), Figure 32.

After NPA for 2 weeks, a small exothermic peak around 120 °C (3), a two-stage endothermic dissolution trough between 150 °C and 245 °C (4,5) and two exothermic peaks at 263 °C and 300 °C (7,8) are found.

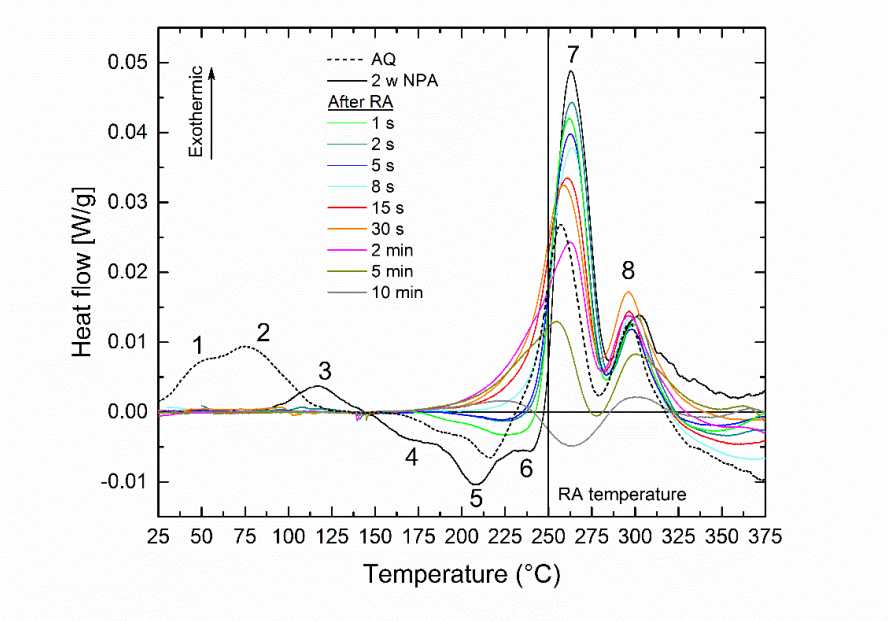

Figure 32. DSC curves of samples after RA in liquid metal. The black curves corresponds to sample measured after solutionising and quenching (AQ) and after 2 weeks NPA without prior RA.

4.2.3.1 Liquid Metal

Figure 32. 1 to 2 s of RA remove the exothermic signal (3) observed for the NPA sample and decrease the size of the dissolution trough (4,5). After 8 s RA the dissolution trough (3) has gone and the first exothermal signal (7) sets in continuously. Up to 30 s RA, the second exothermic peak (7) increases, after which it decreases again. Up to 2 min of RA, the onset of the continuous formation of (7) moves to lower temperatures, the height of the peak decreases but at a stable position. For longer than 5 min RA, both exothermic peaks (7,8) start to disappear.

4.2.3.2 Molten Salt

The effect of reversion is slower in MS than in LM associated to slower heating to 250 °C (see Figure 33). Thus, the change in the DSC signal is slower. Even the shortest RA removes the first exothermic peak (3) at 125 °C One can see the step-like decrease in the dissolution trough (4,5) with increasing the RA time. Up to 15 s RA the dissolution trough (4,5) has continually decreased. The exothermic peak (7) has also decreased in height with increasing RA time while the position is almost stable at 265 °C. 30 s to 2 min of RA eliminate the dissolution trough peak (4,5) and further decrease the exothermic signal (7) and slightly shifted it on the x-axis. Longer RA times have eliminated the exothermic peak (7) and replaced it by an endothermic signal.

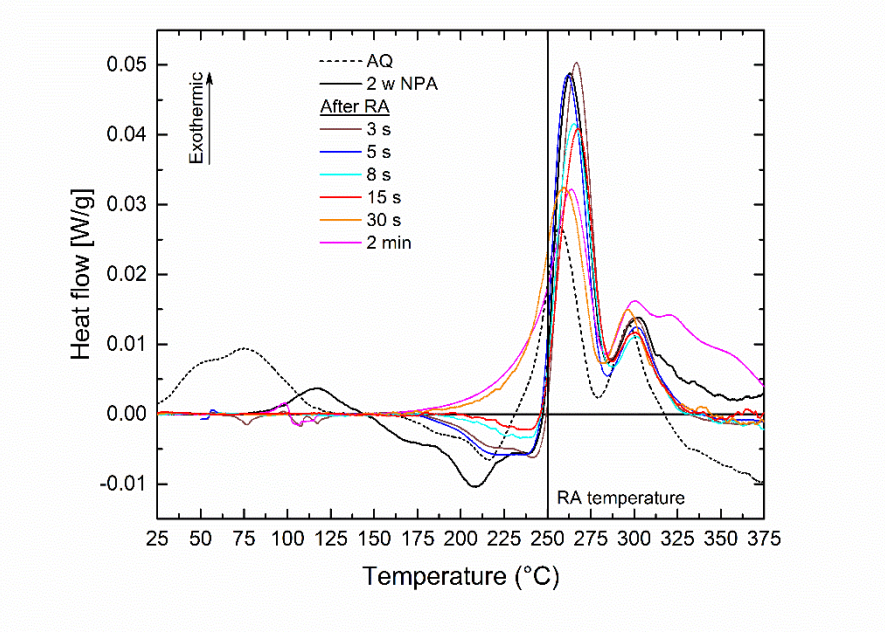

Figure 33. Analogue to Figure 33 in molten salt.

4.2.4 Electrical Resistivity

The resistivity measured ex-situ at 77 K after given RA times is displayed in Figure 26. The change of resistivity during NSA after RA measured at 20 °C is given in Figure 34.

4.2.4.1 Ex-situ Measurements

The values ρ_{77K} measured at 77 K temperature after various RA treatments at 250 °C are represented in Figure 26 by orange dots. The values for the state immediately after solutionising and quenching and after 2 weeks of NPA without prior RA are also given. There is an increase of ρ_{77K} by 19% during 2 weeks of NPA at 77 K (7% for $\rho_{20°C}$, see below). 1 s of RA decreases ρ_{77K} by 1 nΩ·m and the decrease continues for longer RA. It takes 20 to 30 s of RA to reduce ρ_{77K} to a value close to the state after quenching. With further increasing RA time, the electrical resistivity continuously decreases. On the logarithmic time scale, there appear to be 2 ranges: the first up to 2 to 5 min of RA with a moderate negative slope of ρ, and a stage after with a higher slope.

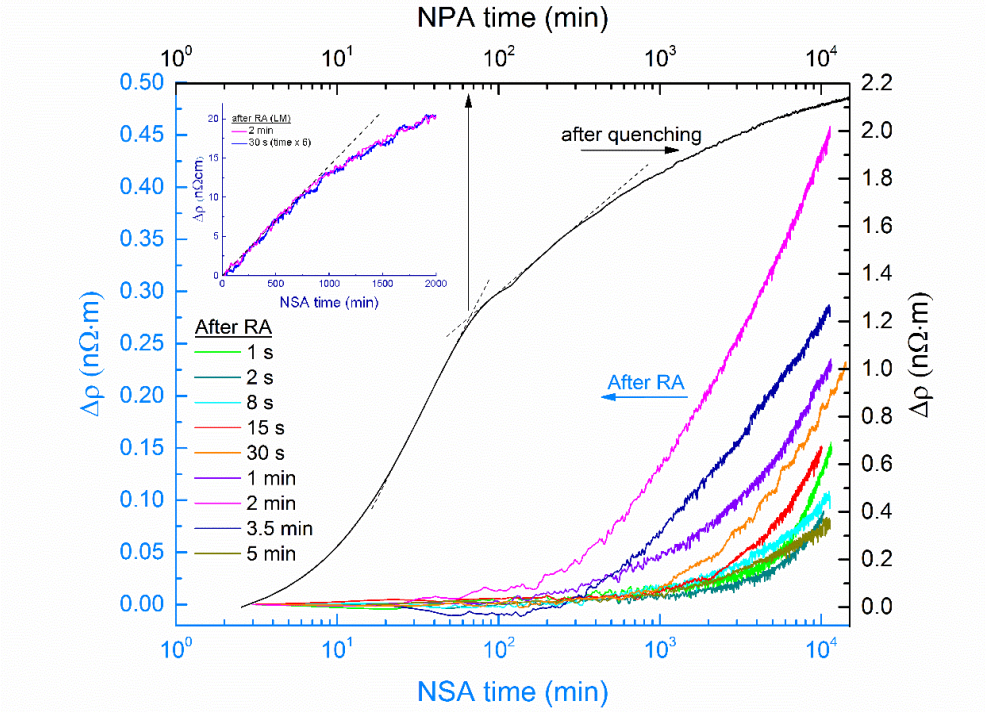

Figure 34. Electrical resistivity evolution measured in-situ during NSA at 20 °C after RA in LM for various given times. The black line corresponds to the AQ state without prior RA treatment. The inset shows the resistivity evolution for 30 s and 2 min RA on a linear time scale. Broken lines are tangents used to define changes in slope.

4.2.4.2 In-situ Measurements

Directly after solutionising and quenching, the resistivity ρ20° C evolves in various stages defined by an approximately S-shaped curve on the logarithmic time axis. After 2 weeks the increase is still measurable. The absolute value after quenching is ~3810 nΩ·cm, therefore the total increase is about 7%. The little kink at 150 min NA time is an artefact.

After RA, the initial resistivity increase is much smaller than after quenching, see coloured lines in Figure 34 that have been expanded by more than 4 compared to the AQ value. The increase is initially linear (no incubation time) and then slows down as can be seen on a linear time scale in the inset of Figure 34 for two RA times. RA time determines the rate of resistivity increase and how early it increases. For 1s to 15 s of RA, the resistivity change is slow. From 15 s to 2 min of RA the rate of resistivity increase gets larger and peaks for 2 min of RA. 3.5 to 5 min RA lead to a decrease of resistivity response after RA.

5 Discussion

5.1 Interpretation of PALS Signals

Positron lifetimes in rather complex systems such as Al-Mg-Si alloys that contain different precipitates are rarely caused by positron annihilation in just one kind of trap. Instead, competitive trapping into different traps is likely. It is useful to first review the various possible ways a positron can annihilate and then define a few simplifying assumptions.

Positrons can annihilate in the free bulk without being trapped. In case all positrons annihilate in this way their corresponding measured lifetime will be around 160 ps [44, 45]. If some positrons annihilate in traps, a reduced bulk lifetime ($0 \leq \tau_1 < 160\ \mathrm{ps}$) is measured according to the trapping model [38].

Positrons trapped in mono-vacancies have a lifetime around 245 ps to 250 ps [45]. If vacancies form a complex with either Mg or Si it has been estimated that the lifetime is modified only marginally (1-3 ps increase for Mg, 1-2 ps decrease for Si) [55, 56]. If vacancies are surrounded by more Mg and Si atoms (vacancy-cluster-complex), there is no reliable data for the corresponding lifetime. Buha assumes a typical lifetime of 221 ps in such complexes [10]. However, this value might vary with the chemical composition of a cluster and since it was derived from one-component spectra it is not clear whether this value is correct.

Vacancy-free clusters of Mg and Si atoms, with possibly some Al in between, can also trap positrons. A lifetime of 200 ps [8], 214 ps [10] or 215 ps [9] has been postulated. Binding between positrons and vacancy-free traps is much weaker than with vacancy-containing traps. Therefore, positrons can be detrapped at high enough temperatures. As a consequence, the contribution of such a trap in competition with a vacancy-related trap depends on the measurement temperature [9]. The binding energy of a positron with a precipitate will depend on its size. Coherent GP zones and β” precipitates are expected to give rise to positron lifetimes slightly lower than the clusters formed during NA, e.g. 210 ps [10, 57, 58]. As precipitates become semi- or incoherent during prolonged ageing, the associated positron lifetime increases [58, 59].

Divacancies and clusters of vacancies would lead to higher positron lifetimes than one vacancy, probably 270 ps or more [45]. In the alloys presented here, we neglect divacancies unlike in binary and more diluted alloys [60]. Dislocations (formed during quenching) may also trap positrons, the associated lifetimes being 210-240 ps [36]. We neglect this contribution in the current work since free dislocations should be shallow traps and contribute little at RT, whereas dislocations associated to vacancies should contribute with a vacancy-like lifetime, i.e. 240 ps [49, 61] or more.

In this work, we assume that positrons have only three ways to annihilate: either in the bulk, giving rise to a lifetime of < 160 ps [45], in vacancy-free solute clusters or GP zones where the lifetime is typically around 215 ps [10], or in defects containing a vacancy (245 ps) [45]. We neglect the fact that clusters and zones (both with or without an attached vacancy) might have a range of different sizes and compositions which in turn would lead to a range of positron lifetimes and that annihilation in vacancies would be modified by the site occupation around the vacancy. Currently, there is no way to measure such lifetime distributions. In many cases we measure a one-component positron lifetime τ_{1C} only and have to deduce indirectly what might have changed it value during ageing.

From the fact that positrons can annihilate in 3 different ways, changes of the average of the three partial lifetimes, approximately expressed by the one-component lifetime can be explained by an increase or decrease of one of the three contributions as listed in Table 3. In some cases a change can have different reasons and additional information is required.

The evolution of τ_{1C} during NA after solutionising and quenching has been studied previously [8] and is also given in Figure 18 and Figure 21, where the first τ_{1C} value measured after quenching is 243 ps in alloy 4-4 and 233 ps in alloy 6-8. Earlier work has shown that in alloy 4-4, at least 85% of the positrons annihilate in vacancy-related traps in this as-quenched (AQ) state [9]. The initial value in alloy 6-8 is 10 ps lower in accordance with Ref. [8]. This is not due to NA after quenching since experiments in which the sample was quenched to 77 K directly from SHT and PALS was carried out at low temperature have yierded the same results [9]. It is rather suspected that during quenching clustering sets in and the corresponding positron trapping component with a typical lifetime around 215 ps reduces the average measured lifetime. The existence of clusters (containing Cu and Zn) in freshly quenched alloys has been shown for AA 7012 alloys as well [62].

During NA, τ_{1C} may first remain constant or even slightly increase (stage I, not visible here), then markedly decrease to a minimum (stage II), re-increase to a maximum (stage III), and then decrease again for about 2 weeks (stage IV, not shown here). This behaviour has been discussed in the literature [8, 9].

5.2 Artificially Ageing at 180 °C

5.2.1 Microscopic Model for Phenomena during Short AA

The different effect of short AA in oil/MS/HP on the one hand and LM on the other must be related to the different heating rates applied. In oil and even more in MS and on the HP, the sample spends a few seconds more at temperatures lower than 180 °C while the temperature is ramping up. It takes the centre of the sample ~6 s to reach 170 °C in oil, 10 s in resting salt, 1 min on the HP, but less than 1 s in LM, see Figure 11a. We propose the following microscopic model and provide evidence in the following sections.

Vacancy migration is thermally activated and its velocity scales with an Arrhenius law, governed by a migration activation energy of $H_{\mathrm{V}}^{\mathrm{mig}} = 0.62$ eV (59.8 kJ/mol) [23]. The formation enthalpy can be neglected because excess vacancies are already present after quenching from 540 °C. The diffusion coefficient for a vacancy can be written as [23]:

$$D_{\mathrm{V}} = \frac{\lambda^2}{6}\, \nu_D\, e^{\frac{S_{\mathrm{V}}}{k}}\, e^{-\frac{H_{\mathrm{V}}^{\mathrm{mig}}}{kT}}, \qquad (5.1)$$

where the jump width λ is 0.28 nm in Al, the Debye frequency ν_D=5×10^{13} s^{-1} and the entropy factor $e^{\frac{S_{\mathrm{V}}}{k}}$~2. Vacancy-solute binding energies are in the range of some tens of meV [63], i.e. in the range of thermal energies at RT. Thus binding rapidly weakens as the temperature increases and the lifetime of a vacancy-solute complex decreases. The same holds for solute clusters, just that the lifetimes of a cluster-vacancy complex approximately scales with the number of atoms in the cluster [25]. Clusters are therefore stronger pinning points for vacancies than individual solute atoms.

At RT, vacancies move slowly through a solid solution, assist in forming clusters before eventually getting irreversibly trapped by a vacancy sink (dislocation or grain boundary). Therefore, the longer

the samples remain at RT or moderately above, the more clusters can be formed. At a higher temperature, vacancies moves faster and spend less time at solutes and clusters. One could say that the solid solution becomes more permeable for a vacancy as T increases.

Thus, when heating slower to an end temperature, more clusters can be formed and excess vacancies will be lost later to sinks than when heating fast. In this case, once a temperature has been reached at which solute atoms no longer bind vacancies, clusters will already have formed that can retain vacancies at this temperature and above due to the higher binding energy between vacancies and clusters. Eventually the vacancies will be liberated and migrate to sinks but the clusters will remain. In contrast, when heating fast, more excess vacancies diffuse to sinks and get lost there before assisting clustering. The vacancy site fraction will approach the much lower value of the thermal equilibrium.

As a consequence, an alloy contains more clusters after slow heating and more positrons annihilate there with a lifetime of 200-215 ps. This brings τ_{1C} closer to such values. After heating fast, fewer clusters have formed and many more positrons annihilate in the bulk, which is why τ_{1C} is closer to the lifetime in the bulk.

5.2.2 Interpretation of Positron Lifetimes after AA and Verification of Model

5.2.2.1 General Procedure

The interpretation of positron lifetime spectra is based on the observation that 3 distinct contributions contribute to the measured spectra. This has been shown using a spectrometer with a very high resolution [9]. In this work, we could resolve the lifetime spectra into 2 components (in some cases only one). One of these components, τ_1 is short and represents reduced bulk annihilation (<160 ps). The second contribution contains a mixture of annihilation in clusters (τ_2 around 215 ps) and vacancy-related defects (τ_3 ~ 245 ps). The average is called τ_{23} here and lies in the range between these extremes. Assuming the validity of the two-state trapping model, we can calculate the total site fraction of positron traps associated to τ_{23} (clusters + vacancy-related) [38]:

$$x_{23} = \frac{I_{23}}{\mu \cdot I_1}\left(\frac{1}{\tau_1} - \frac{1}{\tau_{23}}\right), \tag{5.2}$$

where μ is the effective trapping rate depending on the type of traps involved. For a monovacancy, a value of $\mu = 2.5\times10^{14}$ s^{-1} has been given [43, 64]. For clusters, more effective trapping is likely. We use the observation, that clusters have a value four times higher than vacancies [65].

If τ_{23} is closer to 245 ps than to 200-215 ps, we can conclude that most traps are vacancy-related, if τ_{23} is closer to 200-215 ps, clusters dominate. This is shown by the horizontal dashed dividing line in Figure 14a. From the value of τ_{23} we can therefore derive a rough estimate of I_2 and I_3:

$$I_2 = \frac{245\ \text{ps} - \tau_{23}}{245\ \text{ps} - 210\ \text{ps}}\, I_{23}\ , \quad I_3 = I_{23} - I_2\ , \tag{5.3}$$

From these estimated intensities we calculate an effective trapping rate of $\mu = \frac{4I_2+I_3}{I_{23}} \times 2.5 \times 10^{14}\ s^{-1}$ to be used in Eq. (5.2).

In the solutionised state (before quenching) the vacancy site fraction should be 1.4×10^{-4} [66]. After quenching but before AA, the excess vacancy density is still high and some clusters might have formed during quenching [9]. Calculations of the initial vacancy site fraction after quenching, x_v^{AQ}, predict 6×10^{-5} for a Al-0.4Mg-1Si alloy and very fast quenching [67], i.e. about 50% of the vacancies have gone to vacancy sinks (surfaces, GBs, dislocations) during quenching.

5.2.2.2 Lean Alloy 4-4, Fast Heating

After fast heating and short AA (1 s and 5 s) in LM, the site fraction of traps has dropped to less than 1/15 x_v^{AQ} (Figure 35) and τ_{23} is 232 ps or more (Figure 14a), indicating that most traps are vacancy-related and only few clusters have formed. The majority of positrons, however, annihilate in the bulk as I_{23} is just 38% or below (Figure 14b). The traps therefore have a low density. Therefore, the above postulated scenario of quick vacancy losses to sinks (however, possibly not of all excess vacancies) and limited cluster formation upon fast heating is supported by the positron annihilation data.

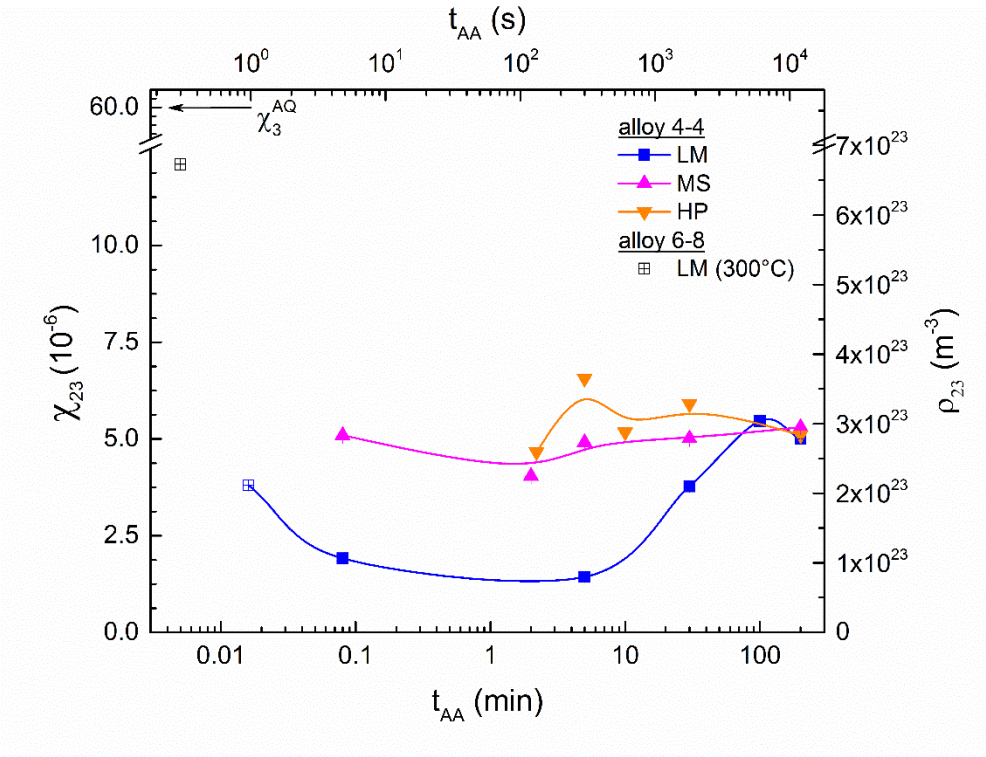

Figure 35. Analogue to Figure 14. The site fraction.

The observation that AA for 1 s can eliminate a large part of the vacancies needs to be further discussed. Applying Eq. (5.1) one can calculate the vacancy diffusion coefficient D_v at 180 °C and from this the vacancy diffusion range $x = \sqrt{6D_v t}$. We obtain x = 1 µm for t = 1 s. The grain size of the alloy is of the order 0.5 mm [8]. Thus, most vacancies cannot reach the grain boundaries in 1 s. However, jogs at dislocations formed during quenching (through quenching stresses) can also trap vacancies. Their density should be of the order 10^{12} m^{-2} (mean spacing 1 µm) to explain the observed massive vacancy annihilation in 1 s. This mechanism has been discussed and modelled in the literature [7]. Such dislocation densities appear realistic, for example 5×10^{13} m^{-2} in quenched Al-10Mg alloy [68]. Therefore, it is plausible that the positron lifetime can drop from 245 ps to 165 ps in just 1 s of AA in LM.

According to calculations, it takes 50 s to reduce the excess vacancy density to 10% the original value after quenching at 1000 K/s and further 50 s to reach the equilibrium vacancy site fraction at 180 °C, $x_v^{180°C} = 7 \times 10^{-8}$ (however, in an alloy with a higher Si content and after 2 min of NPA) [67], a value too low to influence the positron lifetime spectra. Ageing up to 5 min should therefore remove all excess vacancies and the equilibrium vacancy site fraction should be reached [67]. The

total trap fraction is now $x_{23} = 1.5 \times 10^{-6}$ (Figure 35). The measured τ_{23} = 222 ps shows that the cluster fraction relative to the vacancy fraction has increased. τ_{1C} remains almost the same, which is a cancellation effect of the replacement of vacancies by clusters (decreases τ_{1C}) and a decrease of bulk annihilation by 6% (increases τ_{1C}).

Subsequent longer AA increases the site fraction of positron traps (GP zones, β" and β' precipitates), see Figure 35. For 30 min of AA, τ_{23} is smallest (217 ps), for 100 min and 200 min AA, it is larger again (223 ps and 235 ps, resp., Figure 14a). Therefore, the character of the positron traps changes upon AA. For 30 min of AA, coherent precipitates dominate but for longer AA a different trap must be involved. A vacancy-related trap cannot be the reason for the increased lifetime since prolonged AA does not increase the density of such traps any more as all vacancies are in thermal equilibrium. In accordance with Ref. [58] we assume that additional open volume associated with the partial incoherency of the precipitates formed at this stage causes the increase of τ_{23}. The precipitation sequence involves a transition from early GP zones to β" and eventually β' precipitates and the degree of lattice mismatch and eventually incoherency increases in this order. As I_{23} increases up to 76% concomitantly with τ_{23}, τ_{1C} is notably increased to almost 235 ps (Figure 13). The precipitates density for 200 min of AA is 3×10^{23} m^{-3} (right axis in Figure 35), a value notably higher than measured by TEM for the same or similar alloys, for example, 1.9× 10^{21} m^{-3} for 36 h of AA [69] and 1.6× 10^{22} m^{-3} for 18 h AA [70]. Partially this discrepancy could be the consequence of coarsening during prolonged AA but it is also possible, that positrons annihilate in traps that are not detected in the TEM.

5.2.2.3 Lean Alloy 4-4, Intermediate and Slow Heating

After slower heating (in oil, MS, HP), the positron traps are much more densely distributed and fewer positrons annihilate in the bulk and more in traps. For example, traps contribute about 79% to annihilation after just 5 s AA in MS, whereas it is just 34% after fast heating, see Figure 14b. The values for the trap site fraction x_{23} are also higher than for fast heating, for example ~2.5 times for 5 s AA in MS. This indicates that more clusters are formed during slower heating (in absolute numbers). τ_{23} is 222 ps in this case (compared to 232 ps for LM, see Figure 14a). This indicates that more (about 2/3) positrons annihilate in clusters and not in vacancy-related defects already after short AA unlike after short ageing in LM (where it is just about 1/3).

For 2 s AA in oil, the highest temperature reached is 130 °C. We do not have two-component decompositions for this measurement but assume that here some excess vacancies still contribute to the lifetime spectrum, which is why τ_{1C} is still as high as 219 ps.

During prolonged AA up to 5 min in MS, x_{23} remains mostly constant, while τ_{23} initially slightly decreases (Figure 14 and Figure 35). As excess vacancies are lost quite fast, their loss cannot be the only reason for the decrease of τ_{1C}, which eventually leads to such low values as 190 ps for 5 min in oil that a small increase of bulk annihilation seems likely (which, however, does not show in Figure 14b). A possible scenario is: Residual vacancies are quickly lost after a few tens of seconds of AA. Of the clusters formed during heating to 180 °C, which helped to retain vacancies, the smaller ones dissolve within 5 min. This gives rise to some bulk annihilation and the minimum of τ_{1C}. Formation of GP zones takes place in with a delay, first slowly as reflected by an only small increase of hardness from 27 to 33 HV only in oil perhaps due to small GP zone size (Figure 15), but eventually precipitation leads to a re-increase of τ_{1C} within 30 min of AA as bulk annihilation vanishes. The even slower heating on the HP leads to higher values of τ_{1C} than oil and MS due to increased clustering during heating.

For even longer AA (200 min), τ_{23} increases (Figure 14a). As for fast heating, this points at the generation of incoherency between precipitates and matrix as discussed above. For such long ageing times the positron annihilation results are the same for all the heating rates. The site fraction of traps x_{23} is still at the same level as for shorter AA times (Figure 35). Therefore, clusters are seen to transform into a state, where they create stronger lattice strains and eventually more incoherency without much coarsening. This also leads to a notable hardness increase from 33 to 70 HV after 16 h of AA.

Applying Eq. (5.3) one can estimate all three contributions to the positron lifetime by decomposing τ_{23}. Figure 36 shows the results for short AA times and heating in LM and MS in a ternary diagram displaying $\bar{\tau}(I_1.I_2.I_3)$ with $I_1 + I_2 + I_3 = 1$. Starting from the AQ state with a high vacancy site fraction (‘vacancy corner’), the lifetime spectrum moves towards the ‘bulk corner’ with some simultaneous clustering taking place, after which clustering dominates positron annihilation and the decomposition moves towards the ‘cluster corner’. The difference between

fast and slower heating is how much the ‘bulk corner’ is approached, reflecting different kinetics of vacancy loss and precipitation.

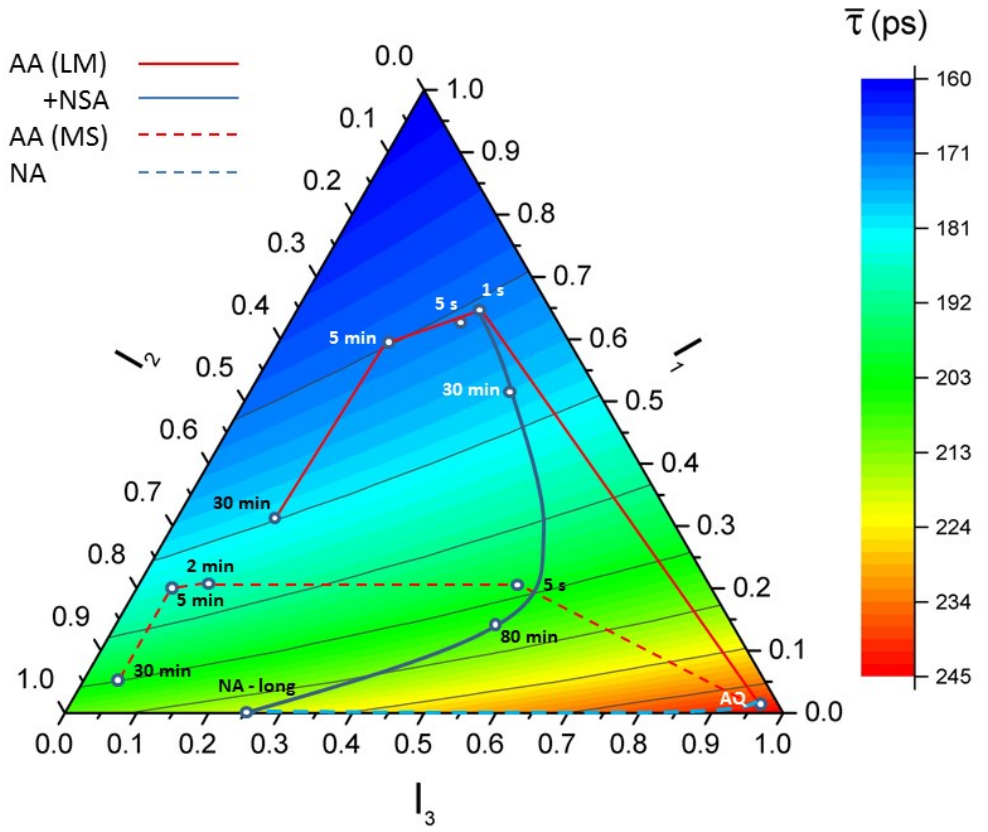

Figure 36. Schematic changes of positron lifetime components in alloy 4-4 in a diagram showing the relative contributions of three positron annihilation mechanisms: bulk ($\boldsymbol{I_1}$, τ_1≤160 ps), clusters or precipitates ($\boldsymbol{I_2}$, τ_2 =210 ps) and vacancy-related defects ($\boldsymbol{I_3}$, τ_3 = 245 ps). Starting with the as-quenched state (AQ), AA in LM and MS is shown up to 30 min (for longer times, lifetime τ_2 increases and the diagram can no longer be used). Values for the intensities were derived from Figure 18a,b and Eq.(5.3) except for 30 min in MS, where only $\boldsymbol{I_1}$ was taken from two-component decomposition and τ_{1C} used as a measure for $\bar{\tau}$ to locate the point in the diagram. The colour coded $\bar{\tau}$ was calculated assuming the three-state trapping model, calculating τ_1 from τ_2, τ_3, $\boldsymbol{I_2}$, $\boldsymbol{I_3}$ and averaging after. For 1 s in LM the NSA curve is shown based on Figure 19 and Eq.(5.3). Direct NA after quenching is also shown. The lines connecting individual points are guides fro the eye and not based on any model.

5.2.2.4 Concentrated Alloy 6-8, Fast Heating

To further verify the interpretations presented we now compare alloys 4-4 and 6-8, both for fast heating. As mentioned in Sec. 5.1, the lower τ_{1C} value after solutionising and quenching given in Figure 16 for alloy 6-8 as compared to alloy 4-4 (Figure 13) reflects the fact that preexisting clusters have formed during quenching. These clusters interact with the migrating vacancies during heating

and delay their delivery to sinks. These diffusing vacancies give rise to further precipitation. This happens even when the alloy is heated fast and extrapolated τ_{1C} values no lower than 190 ps are observed after heating for 1 s at 180 °C and 0.3 s at 300 °C in LM. This shows that pre-existing clusters limit the lifetime decrease observed in alloy 4-4.

Even for short AA (≤ 30 s), positron trapping is close to saturation and reliable two-component decompositions are difficult to obtain. Flash ageing at 300 °C produces a bulk contribution of 16%, and a trap component τ_{23}= 231 ps. Eq.(5.3) indicates that I_2 = 34% and I_3 = 50% in this case. Compared to alloy 4-4 (1 s in LM), this is a much lower bulk contribution (there: 66%) but a twice/thrice as strong vacancy/cluster signal, respectively. Due to bulk annihilation, τ_{1C} is below 200 ps for 1 s and 5 s of AA. The increase of τ_{1C} for 1 s, 5 s and 30 s of AA from 193 ps to 210 ps must be related to the disappearance of the bulk component and the concommitant formation of precipitates. Precipitation during AA is therefore faster than in alloy 4-4 (where it occurs mainly between 5 and 30 min of AA, see Figure 13). There are two possible (non-exclusive) reasons for this: (i) The site fraction of excess vacancies is still above the equilibrium value for up to 1 min of AA. This corresponds to calculations predicting an equilibration time of 100 s [67]. (ii) The solute supersaturation is still high after short AA as only few clusters have formed. This provides a fast driving force for further precipitation during AA.

Between 2 min and 30 min of AA, τ_{1C} shows a slight decrease or constant value, the reason for which is not entirely clear. Perhaps some of the small clusters formed during quenching dissolve. For AA ≥100 min, τ_{1C} increases again to values above 215 ps. Saturated trapping into increasingly semicoherent precipitates can be held responsible for this as in alloy 4-4. However, the increase actually takes place at a later time than in alloy 4-4. This appears unexpected at first sight since hardness increases more in alloy 6-8 than in alloy 4-4 at around 5 min of AA (Figure 15, Figure 17) and thus the faster appearance of semicoherent precipitates might be expected for alloy 6-8. However, it has been found that in alloys with a high Mg+Si content (comparable to alloy 6-8) the peak aged state contains mainly β" precipitates, whereas in low Mg+Si alloys (comparable to alloy 4-4) predominantly β' precipitates are formed without first forming β" precursors [71, 72]. As β' is less coherent with the matrix than β", positrons trapped there could have a longer lifetime. The asymptotic values for long ageing are the same in all cases for all the alloys and AA media (~235 ps). Thus, the end point of ageing is a distribution of semi-coherent particles dense enough

to trap most positrons. Overageing for 1 week at 180 °C lets precipitates coarsen and hardness correspondingly decrease but the value for τ_{1C} remains high. Apparently even the coarsened particles trap all positrons efficiently and prevent the appearance of a bulk component that would reduce τ_{1C} again.

5.2.2.5 Concentrated Alloy 6-8, Intermediate Heating

Slower heating in oil modifies the course of τ_{1C} during short AA compared to fast heating. τ_{1C} decreases from an initial value of 223 ps (2 s AA) to 210 ps (30 min AA). Staab et al. report a similar decrease for alloys 6013 and 6061. (206 ps to 203 ps and 213 ps to 208 ps, respectively) [58]. They do not specify the type of AA treatment but moderate heating, e.g. in oil, is likely. The same applies to Buha et al., who measure a decrease 214 ps to 205 ps for a 6061 alloy [10]. The amplitude of change τ_{1C} is smaller in both studies than in the current work. Banhart et al. measure a decrease from 209 ps to 204 ps for alloy 6-8 aged at 180 °C in oil [54]. Thus, both the amplitude and the absolute values are lower than given here. The latter might be due to different adjustments of the spectrometers used. No interpretation for the decrease is given in Refs. [54] and [58]. In Ref. [10], the formation of GP zones is held responsible for the decrease.

For 2 s of AA, the end temperature of 180 °C is not reached in the sample. As heating is rather slow clustering can proceed and limit vacancy annihilation. The total trap density is close to saturation, which is why we cannot decompose into 2 components. τ_{1C} is therefore between the values of cluster and vacancy-type defects. Accepting the above mentioned idea that in alloy 6-8 the equilibrium vacancy concentration is reached in about 1 min, the further decrease to 215 ps is explainable. The ensuing decrease to 210 ps is similar to the situation in alloy 4-4 just that the decrease does not go so far. This points at positron trapping into a much denser distribution of clusters or precipitates. The minimum of τ_{1C} roughly coincides with the maximum of hardness as already noted by Staab et al. [58].

The increase of τ_{1C} for longer ageing times is caused by the formation of semicoherent precipitates as discussed for fast heating. The spectra could not be resolved into 2 components as reported by Staab et al. [58] for long AA times (interpreted by appearance of the long lifetime component in semi-coherent precipitates). The increase is also much more pronounced in this study than in other work [10, 58].

5.2.2.6 Lean Alloy 4-4, Additional NA before AA

In order to verify the idea that clusters formed in alloy 6-8 during quenching before AA (unlike in alloy 4-4) limit the loss of vacancies and the associated decrease of τ_{1C} during AA, we carried out experiments in alloy 4-4 in which natural pre-ageing (NPA) was performed before AA, see Sec. 4.1.3, to form clusters as well. As discussed in Ref. [9], during NA (called NPA here and represented by black line in Figure 25) clusters grow continuously and vacancies are slowly lost. 5 min of NPA already have a small influence on the extent 1 s of AA in LM decreases τ_{1c}. After 30 min or 80 min of NPA; the post-AA value is comparable to the one measured in alloy 6-8 after short ageing in LM. Thus, even though the clusters are formed during NPA here, their effect is similar to the clusters formed in alloy 6-8 during quenching. Banhart et al. [13] carried out experiments with similar setup using oil as AA medium. They found increase in the PLT after NPA and AA (in oil) in similar manner as in the current study.

5.2.2.7 Lean Alloy 4-4, Different Quenching Rates

In a previous study, the positron lifetime in alloy 4-4 directly after quenching was studied for different quenching rates (no AA involved) [9]. Slow quenching was found to lead to a lower initial τ_{1C} than fast quenching. One can argue that slow quenching allows the alloy to age more during cooling and is equivalent to a short NA or AA treatment during which some initial clusters or precipitates are formed. The longer this extra ageing, the lower the value of τ_{1C}. This is in line with the argument in the previous paragraphs.

5.2.3 Natural Secondary Ageing (NSA)

During NSA at ‘room temperature’ after not too long AA, natural ageing takes place as directly after solutionising and quenching, just that the starting conditions are different. If the matrix around the precipitates formed during previous AA is still supersaturated, decomposition and cluster formation will set in. The rate and extent to which this happens will depend on: (i) the degree of solute supersaturation in the matrix and, (ii) the site fraction of available vacancies. The rate of NSA should be proportional to vacancy density, the minimum value of which is the equilibrium density at 180 °C since the samples were quenched after AA. Excess vacancies above this level could still exist for short AA times. From the characteristics of NSA, we attempt to deduce

information about the AA state. As two-component lifetime decompositions during NSA are available only in few cases, the following discussion will be based in parts on interpretations of the one-component positron lifetime τ_{1C}.

5.2.3.1 Lean Alloy 4-4

Samples AA for up to 100 min (oil) or 200 min (LM, HP) show a pronounced increase of τ_{1C} (Figure 18a-d) approaching an end value of ~220 ps for long NSA. The reason for this increase of τ_{1C} is linked to changes of one or more of the three principle contributions to PLT described in Sec. 5.1: (i) As vacancies cannot be created at RT and their density will rather decrease they cannot be responsible for increases of τ_{1C}. (ii) In contrast, cluster nucleation (in addition to the precipitates already formed during AA) and growth could increase τ_{1C} because positrons trapped in such clusters have a lifetime of typically 215 ps, which is higher than the values of τ_{1C} directly after short AA in most cases. After NSA, the end value of $\tau_{1C} = 220$ ps is slightly higher than expected from a pure cluster population, pointing at the existence of some vacancies or an effect of Mg enrichment, (iii) Any decrease of positron annihilation in the bulk (shortest lifetime) would also increase τ_{1C}. Such a decrease would be caused by new clusters formed in the solid solution. Indeed, two-component decompositions of the lifetime spectra during NSA indicate that bulk annihilation decreases in the course of NSA. In the samples heated in LM, the high bulk contributions after short AA (i.e. 65% after 1 s, Figure 14b) are reduced to 10-20% during NSA, see Figure 19. In the samples heated in MS, the bulk contribution of initially ~20% (Figure 14b) decreases to about half this value or less (not shown).

The increase in hardness (see Figure 20) confirms that clustering is one important reason for the increase of positron lifetime during NSA since clustering causes hardening. The time for hardness to increase to half the maximum value is about 10 times higher than the analogous time for τ_{1C}. Therefore, as discussed in Sec. 5.2.2.3, we observe that clustering does not immediately lead to a hardness increase because a minimum cluster size is required.

In order to quantify the kinetics of NSA, we use the time $t_{1/2}$ needed for half the total increase of τ_{1C}, see Figure 37. One can note that, (i) This time gets larger with increasing AA time, i.e. NSA kinetics slow down with longer AA, (ii) The kinetics are faster for fast quenching in LM than for the other quenching media. However, all these differences are not large. Between 100 and 900 min

of NSA time in Figure 18d, the slope of τ_{1C} is very similar for all AA times and even for the samples not AA at all (black line).

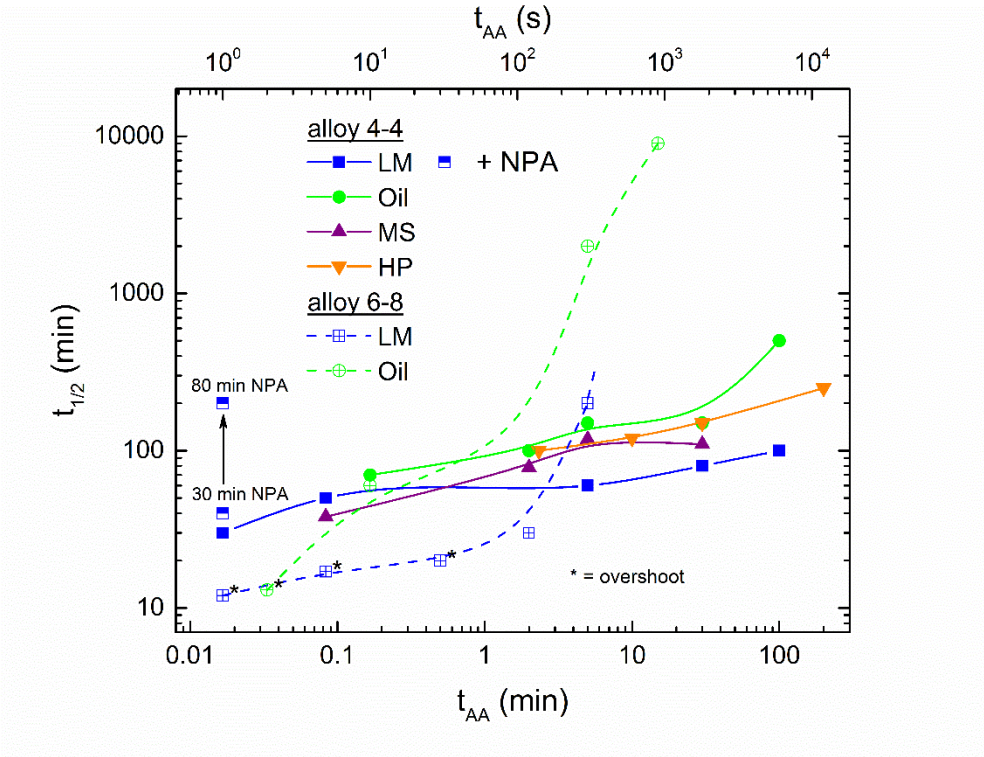

Figure 37. Time $t_{1/2}$ needed for $\boldsymbol{\tau_{1C}}$ to increase from the lowest to the highest value in Figure 18, Figure 20 and Figure 25. Asterisks denote curves that show a sharp overshoot after 15 to 30 min. In this case the rise-time to half the overshoot value is given.

For AA in LM, strong bulk annihilation takes place and causes τ_{1C} to be low. As outlined in Sec. 5.2.2.2, very short AA in LM produces a state of very low cluster density and reduced but still measurable excess vacancy contribution (about 3×10^{-6}, Figure 35). Low cluster density implies high solute supersaturation. This must be the prime reason for fast ageing after 1 s at 180 °C. Alloy 5-5 that contains 20% more Si and Mg consequently shows a 50% lower $t_{1/2}$ (and 5 ps higher τ_{1C} initial after AA), see Figure 24. Longer ageing in LM for up to 5 min increases the cluster population and hence decreases solute supersaturation. At the same time the vacancy contribution is reduced, Figure 36. Both effects slow down NSA, as actually seen in Figure 37.

For slower heating, for example in MS, bulk annihilation is much smaller than for AA in in LM, Figure 14b, and more positron traps (clusters + vacancies) are present, see Figure 35. More clusters

imply lower solute supersaturation and slower NSA in MS than in LM. This is actually observed in Figure 37.

After 30 min and 100 min of AA in LM, the bulk component is notably reduced, reflected by a clear increase of τ_{1C} caused by pronounced precipitation. Still, NSA kinetics is slowed down only slightly. This is also observed for AA in other media, see Figure 37. This point is not entirely understandable: Although NSA kinetics slow down by a factor of 3 from the shortest AA time to the longest where NSA is still observed, this appears less from what one would expect for a much higher reduction in solute supersaturation and vacancy concentration.

The increase of τ_{1C} and hardness is observed after an incubation time, during which τ_{1C} is almost constant or only slowly increasing. For fast heating in LM, the incubation time is shorter (about ½) than for slower heating in the other media in accordance with the above discussed time $t_{½}$. The existence of an incubation time for τ_{1C} is not easy to understand. It seems unlikely that the microscopic state of an alloy after AA remains unchanged for 20 to 100 min, after which suddenly clusters start to form. Rather, one would expect a continuous development, i.e. cluster formation already takes place during the incubation time without changing the positron lifetime. There are two possible explanations for this: (i) the initial clusters are so small that positrons are not trapped in them because they are too shallow. Only after the incubation time, the clusters have grown enough to allow for positron trapping at RT unlike after quenching from 540 °C, when clustering almost immediately leads to a decrease of τ_{1C}, see black line in Figure 18a. The reason for the formation of such small clusters could be the lower solute supersaturation after AA compared to the as-quenched state. (ii) The lifetime increase associated to clusters formed during the incubation time (provided that τ_{1C} is above 215 ps) is largely compensated by a decrease caused by another component. This can only be the vacancy component, see Table 3, but this is unlikely since excess vacancies are largely annealed out after minutes of AA.

Table 3. Underlying mechanism governing the change of the averaged ($\bar{\tau}$) or one-component positron lifetime (τ_{1C}). + and – denote an increase or decrease of a specific contribution.

	Decrease of $\bar{\tau}$ or τ_{1C}	Increase of $\bar{\tau}$ or τ_{1C}
245 ps		
	–V: vacancy loss	+ Mg: addition to clusters
	+ C: cluster formation	– C: reduction in clusters
	+ B: increasing empty space	+ Open volume (incoherency)
		–B: reduction of empty space
215 ps		
	–V: vacancy loss	+ C: cluster formation
	– C: reduction in clusters	–B: reduction of empty space
	+ B: increasing empty space	
160 ps		

The incubation time is similar to the 80 min duration of stages I+II in samples only naturally aged after quenching, see Sec. 5.1 and Refs. [8, 13]. It therefore seems as if the incubation time mainly represents the absence of stages I and II (strong clustering of mainly Si atoms), whereas secondary ageing is the analogue to stage III in NA samples (addition of Mg to existing clusters). The sample aged in oil even shows the maximum of τ_{1C} after ~700 min and a slight decrease after, i.e. stage IV of the NA curve.

Supporting information comes from Figure 25: If NPA takes place before short AA, the kinetics of NSA is slowed down. The corresponding halftimes $t_{1/2}$ are included in Figure 37. 80 min of NPA before AA actually slows down kinetics of NSA more than long AA. The reason could be that after 80 min of NPA most of the Si solute atoms have been locked up in clusters due to the three times faster diffusion of Si than Mg at 'room temperature' [34]. AA for 1 s does not dissolve these Si-rich clusters and subsequent clustering is dominated by slow Mg diffusion as in stage III of direct NA.

An incubation time for hardness also exists, Figure 20, but is difficult to determine precisely due to the small hardness changes. The reason for the incubation time for hardness could be that clusters have to reach a certain size to influence hardness notably.

The amplitude of τ_{1C} increase is largest for fast heating in LM ($\Delta\tau_{1C}$ up to 47 ps), only about half this value is found for heating in oil and HP. This lower amplitude is due to the higher starting value after AA because the end value is always around 220 ps in all the quenching media.

For AA times of 200 min or more no more increase of τ_{1C} during NSA can be observed. There are several possible reasons for this: (i) significant further clustering might not take place any more after long AA since the supersaturation of the solid solution has decreased too much. (ii) AA already produces a τ_{1C} of 220 ps or more and clustering can no longer change this value very much because it contributes a lifetime component of ~215 ps. (iii) bulk annihilation is small at this stage and large reductions are no longer possible (which would increase τ_{1C}).

5.2.3.2 Concentrated Alloy 6-8 and other Alloys

The basic reasons for the changes of τ_{1C} variations during NSA must be the same as for alloy 4-4, i.e. cluster growth and annihilation within at the cost of annihilation in vacancies and the bulk. Two-component decompositions are difficult as trapping is almost saturated in alloy 6-8. Only for 0.3 s ageing at 300 °C in LM the bulk component can be estimated: 17% for 5.5 min of NSA and 8% for 10 min. For 20 min of NSA, it can no longer be detected. Altogether, this supports that clustering sets in and τ_{1C} increases mainly because the bulk component is replaced by the cluster component. The observation of hardening, Figure 23, also supports the idea of clustering during NSA.

What is special in alloy 6-8 is that the samples heated fast to 180 °C and kept there for up to 30 s and the sample aged in oil for 2 s show a fast change of τ_{1C} which is a very different behaviour from the other heat treatments and from alloy 4-4. These experiments are marked by an asterisk in Figure 37. This fast NSA is possibly related to the fast AA observed in alloy 6-8 (Figure 16) for the first 1 min, see Sec. 5.2.2.4, which is also absent in alloy 4-4 (Figure 13).

A two-component analysis of the experiment with 0.3 s ageing at 300 °C using Eqs. (5.2) and (5.3) yields a high trap site fraction of 16×10^{-6} after 5.5 min of NSA, a good part of which are vacancies. The reason for this high vacancy concentration are the pre-existing clusters in alloy 6-8 that retain vacancies during heating up and the ageing time too short to notably increase cluster site fraction and to reduce solute supersaturation.

The increase of τ_{1C} to values up to 230 ps shows the predominance of vacancies even after 15-30 min of NSA. As in alloy 4-4, the bulk contribution is replaced by cluster growth but in alloy 6-8 the increase surpasses the typical range for clusters (215-220 ps) due to the still high vacancy site fraction. Trapping of positrons by vacancies must peak near the maximum of τ_{1C} for reasons not exactly known. After the maximum τ_{1C} has been reached in Figure 21, the bulk contribution has gone and saturated positron trapping starts. Further clustering then leads to a reduction of τ_{1C} towards the value for clusters. The sample treated for 0.3 s at 300 °C showed almost similar initial τ_{1C} as the one AA for 1 s at 180 °C, but NSA was even faster. This can be explained by the fact that even more vacancies are still in the sample after dipping into LM at 300°C and quenching. The sample AA for 2 s in oil also shows fast NSA and an overshoot of τ_{1C}, which is explainable by the high vacancy concentration retained by a moderate concentration of clusters as postulated in Sec. 5.2.2.5.

All the four alloys with a high total solute concentration (about 1.4%) show the same initial value of τ_{1C} after AA around 195 ps as alloy 6-8, Figure 24, indicating that clustering have taken place during quenching. However, alloy 10-4 exhibits an extended incubation time and a τ_{1C} increase that is similar in kinetics to alloy 4-4 and only a very slight overshoot. A possible reason is the low Si content in this alloy. Diffusion of Si is 3 times faster than that of Mg at 'room temperature', whereas at higher temperatures the difference is smaller. Therefore, during quenching both Mg and Si would diffuse and form clusters (and consume solute) but during NSA the low Si content would slow down clustering. Thus, it is predominantly a high supersaturation of Si that leads to rapid NSA.

For longer AA, the kinetics of NSA rapidly slows down. From 2 min to 5 min AA this is very notable and for 30 min AA, no more NSA can be observed. This corresponds to the end of the rapid precipitation stage represented by the increasing τ_{1C} in Figure 16. Thus, the driving force for NSA has been compromised by the consumption of solutes by previous precipitation. Figure 37 shows that corresponding times $t_{1/2}$ for heating in LM that show a pronounced increase. For AA in oil, these times are even longer. Comparing AA for 2 min and 5 min in oil, the initial τ_{1C} after AA are very similar, but the kinetics of NSA has dropped a lot to 5 min, most likely due to lower solute supersaturation after 5 min of AA.

Buha et al. [10] studied NSA in 6061 alloys for AA times from 1 min to 15 h. After AA for 1 min, they find an increase of τ_{1C} from 214 ps to 220 ps within 450 min and explain this by clustering of solute atoms. This is in line with our measurements. After 5 min AA, no more NSA is observed up to 850 min after which the measurement was stopped.

NSA has been studied before in Al-Cu-Mg alloys [11] and Al-Zn-Mg alloys [12]. In both cases an increasing τ_{1C} is first measured during NSA, after which τ_{1C} decreases again. The increase was interpreted by the aggregation of Mg to the clusters, while the decrease was attributed to the aggregation of Cu or Zn. Possibly, this interpretation has to be revised because an important reason for the rather fast increase of τ_{1C} is the disappearance of the bulk component of positron annihilation.

5.3 Reverse Ageing at 250 °C

5.3.1 Natural Pre-Ageing (NPA)

5.3.1.1 Hardness and Electrical Resistivity

Throughout NPA, hardness increases continuously with decreasing rate as clustering of atoms from the supersaturated solid solution sets in (black line in Figure 27 and Figure 28). Two hardening stages can be distinguished based on a representation on a logarithmic time axis on which a higher and a lower slope can be observed with a transition around 100 min [13, 73]. However, within these two stages the hardening rate continuously decreases as can be seen on a linear time axis. The transition at 100 min is therefore a slowing down of the rate of hardening (second derivative) and not just of hardening (first derivative).

Similar to hardness, resistivity increases continuously throughout NPA. The stages observed on a logarithmic time axis resemble the stages of hardness also in terms of the transition times [13]. The postulated “fast” and “slow” reactions appear clearly only on a logarithmic time scale [19, 74, 75]. As for hardness, the change of rate must be related to a change of mechanism, the origin of which is not exactly known.

The transition around 100 min of NA has to be associated to a change of the clustering mechanism that would slow down clustering or a change of cluster composition that would, for example,

decrease the hardening efficiency of clusters. Unfortunately, there is no general theory describing cluster hardening in terms of cluster size, density and chemical composition, see discussion in Refs. [76, 77]. We shall adopt the viewpoint that the slower diffusion of Mg compared to Si gives rise to a rate change, see below. The observed linearity on a logarithmic time scale has been discussed in terms of a simple model in Ref. [25].

The continuous decrease of the vacancy site fraction and the consumption of solutes and the associated lower solute supersaturation is responsible for the general slowing down of hardening. Figure 38 shows how the rates of resistivity and hardness increase evolve during NPA and NSA. For both resistivity and hardness, the rate from 10 min to 1 week of NPA after quenching drops to less than 0.001 after 4 weeks and 2 weeks of NA, respectively (black symbols and lines).

Both hardness and resistivity can be thought to depend on the volume of clusters v formed during natural ageing. The exact relationship is not known but should be monotonic, perhaps even approximately linear. The rate of precipitation is proportional to the vacancy density x_{vac} as vacancies transport solute atoms to the emerging clusters and act independently. Another factor influencing clustering rate is solute supersaturation x_{sol}. Again, there is probably no linear relationship between solute supersaturation and clustering rate, rather a monotonically increasing function f that defines the rates:

$$\frac{d_\rho}{dt} \propto \frac{dHV}{dt} \propto \frac{dv}{dt} \propto x_{vac} \times f(x_{sol}) \,, \tag{5.4}$$

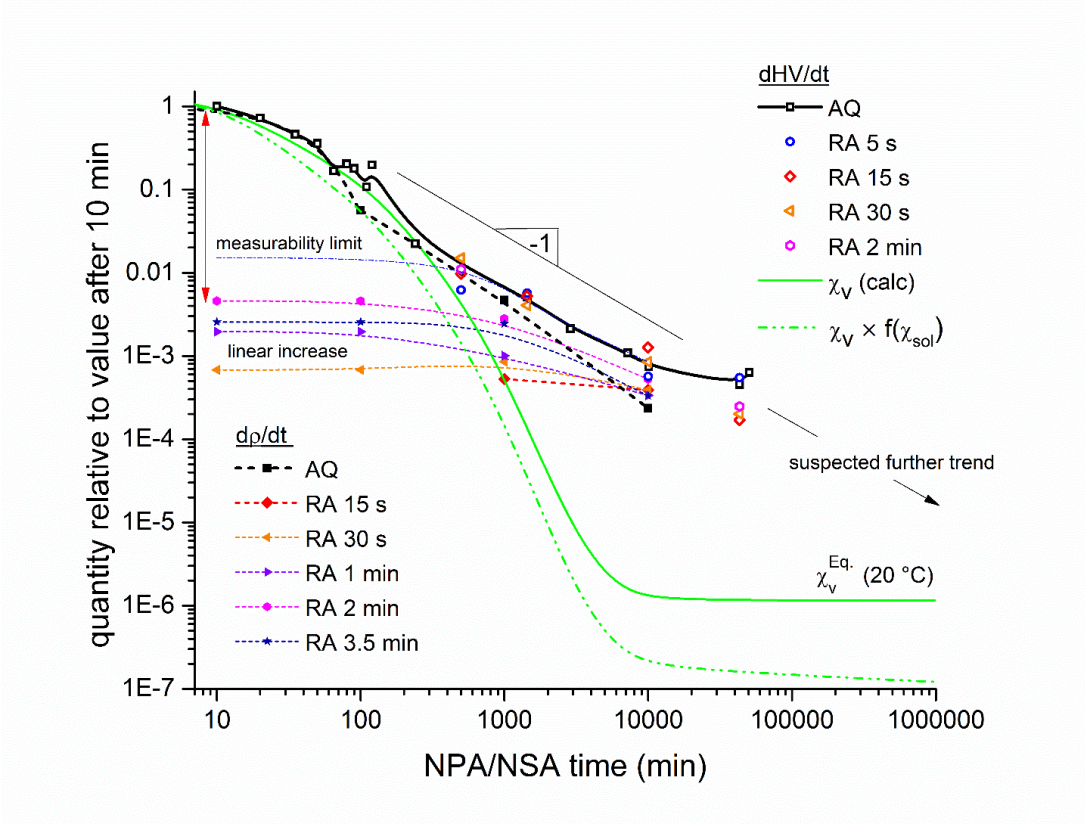

Figure 38. Rate of change of resistivity and hardness for samples after quenching (NPA) or after RA (NSA). The vacancy site fraction x_v as calculated by Falahati for an alloy Al-1Si-0.4Mg [67] is also given. Values for AQ and x_v have been normalised so that initial values for 10 min of NPA/NSA are 1. Values for NSA after RA have been normalised by the same factor. Green dashed line: expected course of resistivity and hardness rate based on calculated vacancy fraction and a simple assumption of decreasing solute supersaturation.

For illustration and qualitative discussion one can assume that solute content in the matrix x_{sol} is zero directly after quenching and goes down to some residual value a after long NA. As in Eq. (5.4), we assume that resistivity scales with cluster volume and that solute used for clustering decreases x_{sol} , hence:

$$x_{sol} = \frac{\rho_\infty - \rho_{(t)}}{\rho_\infty - \rho_0} + a\,, \tag{5.5}$$

Using experimental values for ρ(t) and a = 0.1 in Eq. (5.5) and setting $f \equiv 1$ in Eq. (5.4) we obtain the broken green line in Figure 38. Obviously, the measured rates of hardness and resistivity increases follow the calculated line approximately only for a few 100 min of NPA but deviate after.

This implies that ageing is primarily vacancy-dominated in the first stage and solute depletion does not primarily influence kinetics. As vacancies go to sinks, clustering slows down about 2 orders of magnitude within a few hundred minutes. In even later stages, however, the resistivity and hardness increase is far above what one would expect from the calculated equilibrium vacancy density which reaches the thermal equilibrium at 'room temperature' after a week.

The reason for this discrepancy must be trapping of vacancies in clusters that is not accounted for in the calculation. The more clusters are formed the more vacancies are temporarily absorbed, after which they are released and transport solutes to other clusters again. The density of vacancy sinks (dislocation jogs and rings) is too low compared to cluster density in this stage. Therefore, clustering continues for a much longer time, see arrow 'suspected trend' in Figure 38.

5.3.1.2 Positron Lifetime

The course of τ_{1C} evolution during NPA after solutionising and quenching (Figure 29 and Figure 31) has been studied previously [8, 54, 78]. The initially high τ_{1C} after quenching (~233 ps) decreases to a minimum (~218 ps) after ~40 min NPA. Subsequent increase and re-decrease to a value of ~219 ps after 2 w NPA are observed.

Immediately after quenching, vacancy-related defects (e.g. free vacancies or vacancy-solute complexes) dominate but some clusters have already formed during quenching (about 25% intensity, [39]). During NPA, more clusters form, grow and become more effective positron traps that increasingly dominate positron annihilation as the influence of vacancy-related defects fades from the positron signal. τ_{1C} reaches a minimum value of ~218 ps at the end of what has been called 'stage II' [8]. Atom probe analysis shows that the clusters formed contain both Mg and Si [34, 79]. At this stage, the calculated free vacancy site fraction according to Falahati is $x_v = 1.5\times10^{-6}$ [67] and could therefore contribute to τ_{1C} taking account of typical measured cluster densities (2.4 to 10) × 10^{23} m^{-3} after 100 min or 3 h of NA [34, 79] corresponding to a cluster site fraction x_c = (4 to 17) × 10^{-6}. The typical τ_{1C} in a cluster could then be slightly below this value (e.g. 215 ps as argued in Ref. [9]). A small influence of trapping in dislocations is also likely [60, 80], however constant in time, which is why it is not further considered here.

The increase of τ_{1C} by 5 ps in subsequent 'stage III' has been explained by Mg in-diffusion into existing clusters and a corresponding increase of the typical annihilation lifetime τ_2 within. According to calculations, fcc clusters of Mg in Al lead to a much higher positron lifetime than clusters of Si [81] and for mixed clusters of Mg and Si, although no calculations are available, an increase of τ_2 with Mg content appears plausible. Other arguments supporting this are the absence of stage III in alloys low in Mg [39], NMR spectroscopy measurements [78] and some APT measurements of cluster compositions than show an increasing Mg:Si ratio with NA time [82]. However, other APT investigations do not confirm a Mg increase [34, 83] and positron Doppler measurements rather show an increasing Si environment around the positron annihilation sites for longer NA times [54, 81]. In another study, APT yielded a constant average Mg:Si ratio as NA proceeded but the increase of cluster number density was more pronounced for clusters with Mg/Si>0.4 than for Si-rich clusters, the number density of which remained constant [79]. Cizek et al. show a slight increase of τ_2 from 215 ps in stage II to 222 ps at the end of stage III. Therefore, the increase of τ_{1C} in stage III is at least partially caused by the increase of τ_2 and this increase could be explained by an increasing number of clusters rich in Mg.

An alternative explanation would be that of cluster coarsening and a corresponding increase of the relative importance of annihilation in vacancy-type defects. According to Falahati, the free vacancy site fraction at the maximum of τ_{1C} (after 1000 min) is as low as 4×10^{-9} [67]. This would be below the sensitivity of PALS. Only if a significant number, i.e. $>10^{-7}$, of vacancies remained trapped in clusters (which Falahati did not consider in their calculations but which could be the case considering the discussion of Figure 38) could these contribute. So if clusters merged to larger ones while the vacancies trapped in theses clusters were preserved, τ_{1C} would also increase.

The final decrease of τ_{1C} in stage IV could be caused by a reduction of trapped vacancies (if existing in sufficient quantities) as well as by a slight coarsening of clusters to values below the saturation trapping threshold (10^{-4}). As hardness and resistivity are still increasing at this stage, this effect cannot be very pronounced. Another possibility is a reduction of the annihilation lifetime of positron in clusters τ_2 caused by internal changes of structure such as ordering. The decrease of τ_{1C} does not continue indefinitely and slows down after a few weeks.

We can now describe the state after 2 weeks of NPA, which is the starting state of the reversion experiments. The τ_{1C} value of ~219 ps indicates that most positrons are trapped by clusters and only few by trapped vacancies.

APT investigations of the NA state after different NA times and for different alloys consistently point at a cluster density of 1 to 3 × 10^{24} m^{-3} for a variety of concentrated alloys and 2 weeks of NA. This includes the clusters detectable by APT only. PALS has revealed that after 5 min of NA in an alloy lower in Mg and Si the cluster density is 2.4 × 10^{25} m^{-3} [9] which indicates that positrons get trapped by clusters smaller than the detection limit of APT. This high number explains why positron trapping is saturated in the T4 state.

The equilibrium vacancy density after 2 weeks NA is very low and not detectable by PALS but the question is, how many vacancies are trapped in clusters after 2 weeks. If the reduction of τ_{1C} from 219 to 216 ps caused by short RA was caused by the annihilation of trapped vacancies, the signal corresponding to vacancy-related defects would be around 10% in the PALS spectrum (assuming 245 ps lifetime in such defects and 215 ps in clusters). In this case, the trapped vacancy fraction could higher than the equilibrium vacancy fraction at 250 °C, 7×10^{-7}, see Table 4.

Table 4. Typical site fractions of clusters, vacancies and positron traps discussed in the work.

quantity	source	site fraction (1 = 6 × 10^{-28} m^{-3})
clusters detected by APT after 2w NA	[34, 79, 84-87]	1.6 – 5 × 10^{-5}
clusters that trap positrons after short NA	[9]	5 × 10^{-4}
equilibrium vacancies at 20°C	calc.*	6 × 10^{-12}
equilibrium vacancies at 250°C	calc.*	7 × 10^{-7}
equilibrium vacancies at 540°C	calc.*	1.4 × 10^{-4}
trapped vacancies in clusters after 2w NA	estd.	1.6 × 10^{-6} to 5 × 10^{-5}
saturation limit for positron annihilation	[38]	~10^{-4}
detection limit for positron annihilation	[38]	~10^{-7}
typical density of vacancy traps	estd.	8 × 10^{-9}

* using vacancy formation enthalpy = 0.67 eV and $e^{S/k}$=2

5.3.1.3 Differential Scanning Calorimetry (DSC)

After quenching and 2 weeks NPA, the DSC curve shows only a small exothermic peak ~120 °C. Longer NA for 15 months (not shown) leads to the elimination of this peak. This has to compare

with DSC in the AQ-state, where pronounced clustering takes place during heating (Figure 32 and Figure 33). With increasing NPA time, the clustering peak continuously decreases [88] indicating that clustering takes place already before DSC. The endothermic “dissolution trough” from 140 °C to 250 °C reflects dissolution of the clusters formed during NPA. In the AQ sample dissolution of the clusters formed before during DSC causes a trough, however with a smaller area. Another exothermic peak (~260 °C) represents formation of β'' precipitates, the exothermic peak at ~300 °C the formation of the also metastable phase β' [89-91].

5.3.2 Reversion Annealing (RA)

5.3.2.1 First stage of Reversion (RA time ≤ 30 s)

Already the shortest RA has a strong effect on hardness, resistivity and DSC. The effect is stronger for RA in LM for short times than in MS. 1 s in LM reduces hardness from 68.5 HV to 55 HV, which is half the entire hardening occurred during 2 weeks of NPA. The end temperature reached in this case is 244 °C. 2 s in MS have little effect which must be associated to the lower end temperature reached, 182 °C. 15 s in MS lead to an end temperature of 240 °C and the decrease of hardness has set in. Thus, the process leading to the reversion of hardness requires high temperatures. 30 s in LM and MS lead to the same decrease of hardness down to 47 HV which is the minimum achieved.

Electrical resistivity also decreases most in the first second of RA in LM and then continues to decrease after at a lower rate until it reaches the value of the as-quenched state after about 20 s. After 30 min of RA, resistivity is slightly lower than in the AQ state.

Since clustering increases both hardness and resistivity, the decrease of both during reversion must be associated with the dissolution of clusters. The idea of cluster dissolution is correlated by the DSC curves. The pronounced dissolution trough measured for the NA state (Figure 32 and Figure 33) disappears with increasing RA time since fewer clusters are present. No dissolution signal is observed any more for 15 s RA in LM and for 30 s in MS, reflecting slower dissolution in MS due to the slower increase of temperature mentioned above. The dissolution signal is superimposed by the positive precipitation signal, which is why dissolution appears to terminate faster in the DSC measurements than in hardness and resistivity.

τ_{1C} is also reduced by RA. While in the NA state τ_{1C} is around 219 ps (Figure 26), RA reduces it by about 3 ps except for 8 s in MS where the decrease is only 1 ps. As τ_{1C} is fairly constant for up to 2 min of RA, cluster dissolution is not the reason for this decrease. Possible reasons are the loss of trapped vacancies or preferential out-diffusion of Mg in the initial stage of reversion, after which saturated trapping of positrons in clusters continues to dominate positron annihilation.

The very fast dissolution of clusters in just 1 s at 250 °C requires some discussion. As for the formation of clusters many solute atoms have to diffuse in one specific direction towards one point but the dissolution of a cluster requires the movement of solute atoms in any direction away from the cluster the rate of dissolution can be expected to be higher than the rate of formation. Still, dissolution as the formation of clusters requires the presence of vacancies. Two types of vacancies are candidates for the fast dissolution observed. Vacancies trapped in the clusters after 2 weeks of NA and equilibrium vacancies created in the sample during RA at 250 °C. As discussed above and listed in Table 4, the site fraction of trapped vacancies could be between and 30 times higher than that of equilibrium vacancies accepting the loss of trapped vacancies an explanation for the reduction of τ_{1C} during RA.

The source of equilibrium vacancies in turn are the points in the lattice that have absorbed vacancies during natural ageing, namely grain boundaries, jogs at existing dislocations and Frank loops [7]. The former source can be neglected due to the large grain size in the materials investigated here (hundreds of µm). Assuming a (quite high) dislocation density of 10^{12} m^{-2} and a jog line density of 1/50, the density of vacancy sources is 10^{12} m^{-2}/(50 d) = 5×10^{19} m^{-3} (d=0.404 nm is the lattice constant), with a corresponding site fraction of x_{jog}=8×10^{-10}. This is 5 orders of magnitude lower than the vacancy density immediately after quenching, which is why each vacancy sink must contain thousands of vacancies. It is also 3 orders of magnitude lower than the equilibrium concentration at 250 °C, see Table 4.

From an arbitrary point in the lattice a vacancy can reach a jog in N=4/(3x_{jog}) random jumps. The jump frequency of a vacancy is $\Gamma = \nu_D \, e^{\frac{S}{k}} e^{\frac{-H_{m,v}}{kT}}$. Using $e^{\frac{S}{k}} = 2$ and the vacancy migration energy $H_{m,v}$=59.8 kJ/mol, Γ=108 s^{-1} at 250 °C. The time needed for N jumps is identical for a typical reverse path for a vacancy diffusing from a jog to an arbitrary point in the matrix: t = N/ Γ = 17 s. This rough estimate shows that trapped vacancies could help to explain initial fast cluster

dissolution, but only if vacancies can be generated by vacancy sinks in the large numbers in which they were absorbed during NA.

5.3.2.2 State of Maximum Reversion (RA time ≈ 30 s)

30 s RA puts the hardness to a minimum of ~47 HV in both media. Still, the AQ-state is ~4 HV lower (Figure 26), indicating that either not all clusters have dissolved or/and new precipitates have already started to form in this stage. It is difficult to distinguish between clusters and newly formed precipitates at this stage. Both contribute to hardness. Positron annihilation in clusters and in precipitates will be governed by a similar lifetime as long as the latter are coherent with the matrix [10, 58]. In the DSC curves, the effects of cluster dissolution and precipitation are superimposed.

Clustering increases resistivity and over-compensates the effect of solute depletion from the matrix (that would reduce resistivity). This so-called anomalous resistivity effect has been attributed to strong scattering of clusters peaking at cluster diameters of typically 0.8 nm (about 30 atoms) [92] which is smaller than usually measured by APT measurements for long NA [34, 79, 93]. Once coherent and semicoherent precipitates such as GP zones or β" and β' are formed at elevated temperature, resistivity decreases since particles are too large and solute depletion from the matrix too strong.

As resistivity has dropped below the AQ value in the state of maximum hardness reversion (30 s RA) and will continue to drop with longer RA, it is plausible to assume that some solute has already been removed from the solute solution and has been added to new precipitates that do not contribute to resistivity as clusters do.

Moreover, it is also of great interest and importance to investigate the strength response of the alloy during AA after RA. For doing this, we used samples which have been naturally aged for 2 weeks and then reverse aged for 30 s (the maximum reversion), see Figure 39. Compared to the as-quenched sample (blue curve), the achievable increase in hardness during AA and after the maximum RA is considerably smaller and lower (pink curve), pointing at a lower concentration of mobile vacancies and/or a lower degree of solute supersaturation. Further experiments on samples with different RA times should be carried out to clarify this point.

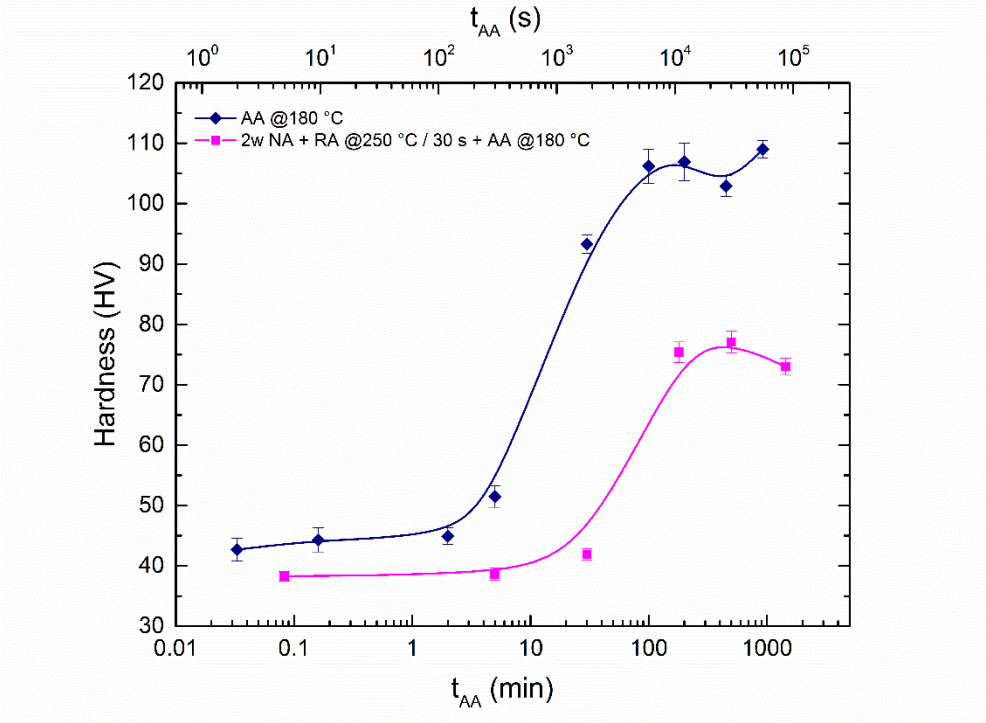

Figure 39. Hardness evolution in alloys with/without (NA + RA) as a function of AA time.

5.3.2.3 Beyond Maximum Reversion (RA time > 30 s)

For 2 min RA, hardness has increased by ~10 HV to 56 to 58 HV, which indicates the presence of the newly formed precipitates formed during the RA. Resistivity has further decreased but relatively less than hardness. τ_{1C} remains unchanged compared to 30 s RA, indicating that positron trapping into clusters/precipitates is still saturated. Therefore, precipitate density might have increased but its structure is still the same.

This changes after 5 min or longer RA. Precipitation of β" has progressed, as evidenced by hardness value of ~75 HV that exceed the fully natural aged state (~68 HV). Moreover τ_{1C} has values of 230 ps (225 ps) after RA for 5 min in LM (MS). This cannot be caused by new vacancies since their concentration cannot change any more after such a long time at 250 °C. The increase rather points at a change of the nature of precipitates. More open volume must have formed that gives positrons a higher lifetime. The appearance of lattice mismatch between the precipitates and the matrix is the most likely explanation [58].

The τ_{1C} value of 235 ps reached after 30 min points at pronounced incoherency of the most likely β’ precipitates formed in this stage of overageing (hardness decreasing) and very low resistivity.

After longer than 2 min of RA, the exothermic DSC peaks (Figure 32 and Figure 33) of the main hardening phase β" and the β' phase are increasingly reduced in height as RA progresses. This indicates an acceleration in β" and β' precipitates formation during RA. After 10 min of RA, not much precipitation is observed any more during DSC.

5.3.3 Natural Secondary Ageing (NSA)

5.3.3.1 Characteristics of NSA

After RA, electrical resistivity starts increasing immediately during NSA with the highest rate in the beginning, after which the rate of increase slows down, Figure 34 (inset). Hardness and τ_{1C}, in contrast, show a different behaviour which is best seen on a linear time scale, see Figure 40. The values do not clearly increase for a while ('incubation time') after which an increase sets in with the highest value initially and a gradual levelling off after.

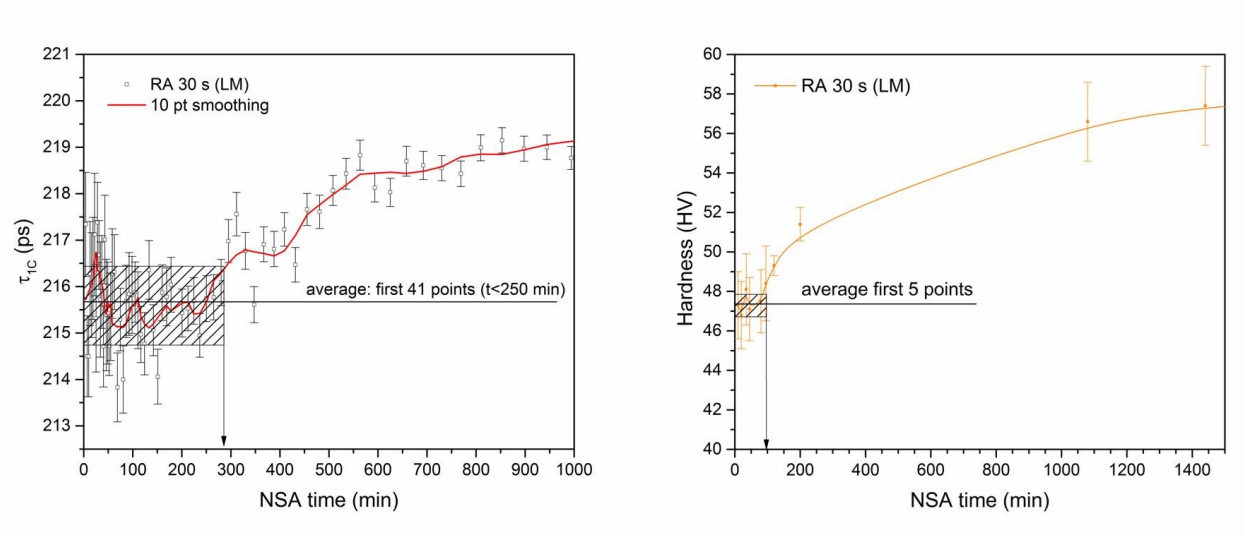

(a) (b)

Figure 40. Incubation for hardness (a) and τ_{1C} (b) after 30 s of RA in LM. The hatched box represents ±SD of the data averaged over the first N points and allows one to estimate the incubation time for the two cases.

The changes of hardness and resistivity indicate that the microscopic reasons are the same as for NA without prior RA, namely the formation of small clusters that give rise to the anomalous resistivity effect and hinder dislocation movement.

The fact that resistivity increases immediately after RA shows that clustering sets in after RA at the highest rate. The incubation times are not the same for hardness and positron lifetime. This points at a sensitivity issue: the initial clustering processes are able to increase resistivity but too small to affect hardness. One possibility is that very small clusters are formed in between larger ones that have a measurable effect on resistivity since their size is close to the 0.8 nm diameter where clusters have the largest effect but do not hinder dislocation movement since hardness is mainly affected by cluster size. During subsequent growth of the clusters, hardness also increases. This different behaviour of resistivity and hardness has been discussed by [94].

The evolution of τ_{1C} also exhibits similarities with the evolution during NPA (increase followed by decrease). What is different is the rate of change and that some of the stages of evolution during NA are missing. In (Figure 27 and Figure 28), (Figure 29 and Figure 31) and Figure 34 one can observe that up to a certain NSA time (called 'early stage') the behaviour is different from that in the 'late stage', namely:

quantity	early stage	late stage
electrical resistivity ρ	linear increase	more than logarithmic increase
hardness HV	no change detected	logarithmic increase
positron lifetime τ_{1C}	no change detected	increase and decrease

The task is to explain these differences.

The slope of electrical resistivity $\frac{d\rho}{dt}$ in early stages (NSA time < a few 100 min) and after 1000 min and 10000 min of NSA is given in Figure 38 for 5 different RA times for which the slope was large enough to be determined in a reliable way. How the slope for short NSA depends on RA time will be discussed in the next paragraph. Here we note that the slope gradually decreases for all the RA times and eventually even crosses the slope of the resistivity increase during NPA.

The slope of hardness $\frac{dHV}{dt}$ after RA could only be estimated for NSA times longer than 500 min because of the rather low number of measurements in Figure 27 and Figure 28. For shorter NSA times, the scatter of hardness values is too large to determine a slope in a reliable way. It is impossible to verify a possible slope of ±1 HV within 100 min from this data, which defines the measurability limit defined in Figure 38. Possibly, the course of $\frac{dHV}{dt}$ is similar to that of $\frac{d\rho}{dt}$ but the

hardening rate might also be much smaller than that of resistivity. In any case, after a few 100 minutes of NSA, the values merge with those of hardening after quenching and NPA irrespective of RA time. The slope is approximately -1, i.e. HV $\propto$ 1/t.

Therefore, the observation is that after quenching and different RA treatments of the NA state the initial hardness and resistivity rates are very different for some 100 minutes, expressing the pronounced difference in vacancy concentration. In a later stage, however, all the trends are quite similar.

The reason why hardness and resistivity drop so slowly in the early stage could be that even after maximum reversion (30 s or 2 min) the alloy still contains enough clusters and early precipitates in relation to the vacancy density to retain vacancies temporarily and to prevent them from going to sinks, whereas after quenching from 540 °C the cluster density in relation to the very high vacancy density is much lower so that vacancies can diffuse much more easily to sinks.

This idea is actually supported by the positron lifetimes given in Figure 26. τ_{1C} is constant here for RA from 1 s to 2 min and the value is 215 ps. This points at saturated trapping in clusters or precipitates and a marginal influence of vacancies and annihilation in the bulk. If reversion had completely dissolved all clusters at any reversion time, the positron lifetime would have dropped below 215 ps.

5.3.3.2 Extent of NSA Effect for Different RA Times

NSA after RA changes hardness, resistivity and positron lifetime in a distinct way. A convenient measure for the average change of resistivity is the value after 1 week of NSA or the initial slope during short NSA as given in Figure 38. Hardness is evaluated after 1, 4 and 60 week of NSA.
For positron lifetime, we use the time of onset of τ_{1C} increase after the observed incubation time as a measure of how much NSA is observed.

In Figure 41 these quantities are compared. Some similarities and differences in the behaviour of hardness, resistivity and positron lifetime during NSA are obvious. These are the features to be discussed:

1) Starting from short RA times, NSA increases with RA time, reaches a maximum and then decreases again (to a low value).
2) The hardness change reaches a maximum value after 30 s of RA. Resistivity increases most for 2 min of RA. Positron lifetime shows the earliest increase and also pronounced increase after 2 min of NSA.
3) Hardness comes very close to the hardness after NPA, whereas resistivity reaches only about 20% of the value after 1 w. However, resistivity is still increasing and might reach higher values after. Even though, hardness appears the quantity exhibiting the highest dynamics during NSA.

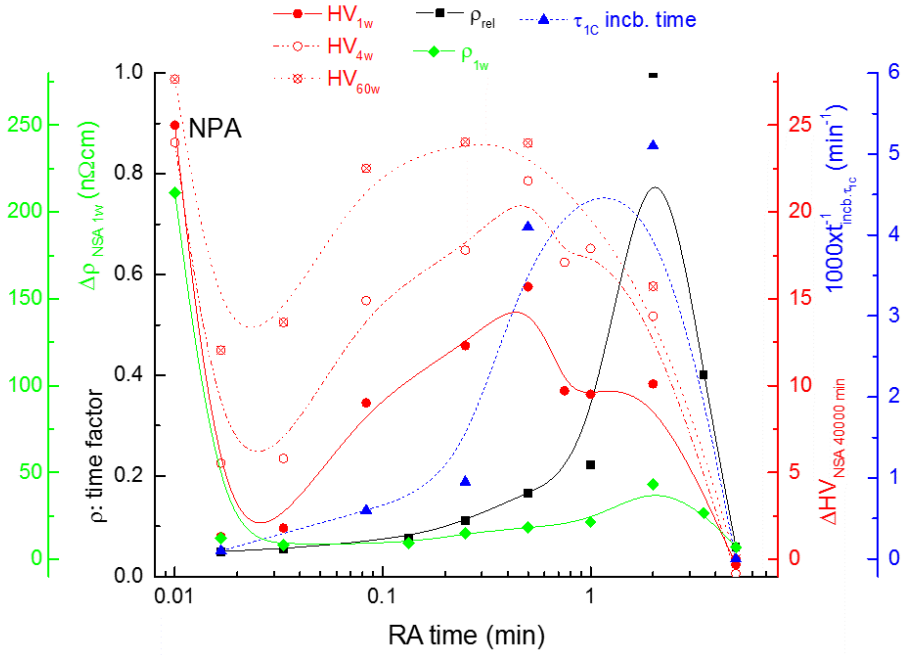

Figure 41. Change of hardness after 1, 4 and 60 weeks and resistivity after 1 week of NSA. For hardness, the values measured within 100 min of NSA in Figure 27 were averaged to set a reference value. For resistivity, the first measured value was taken as a reference value. The points labelled 'NPA' are values taken without any RA. The response of positron lifetime is characterized by the inverse of the incubation time (defined as the time τ_{1C} has increased by 0.75 ps above the average of the values of the first 100 min of NSA in Figure 29.

The rate of clustering expressed by the increase of cluster volume fraction v can be represented by Eq. (5.4) using the vacancy density after quenching from 250 °C as x_{vac}.

A further complication is that observables such as hardness and resistivity not only depend on cluster volume fraction but also on cluster size, size distribution and chemical composition. As no quantitative descriptions of these dependencies are known, the discussion will remain qualitative in nature.

We apply Eq. (5.5) again to calculate the relative amount of solute x_{sol} in the first 30 s of RA using the assumptions described earlier, experimental values for ρ(t) given in Figure 26 and that 50% of the solutes are still in solid solution after 2 w of NPA. These values are given in Figure 42 in the dotted grey-triangular. We further assume that after maximum reversion x_{sol} decreases again (black symbols).

We represent the rate of clustering by the slope of electrical resistivity at the beginning of NSA as given in the inset of Figure 34 for 2 selected RA times (red line and symbols).

The resulting values exhibit a sharp maximum at 2 min RA time. Now the relative vacancy concentration is calculated for 0 to 30 s RA using Eq. (5.4). For RA>30 s, x_{sol} and x_v are unknown but we know that x_{sol} has to decrease and that x_v will go to an equilibrium value. This restricts the way x_{sol} and x_v can vary and the course given in Figure 42 is obtained.

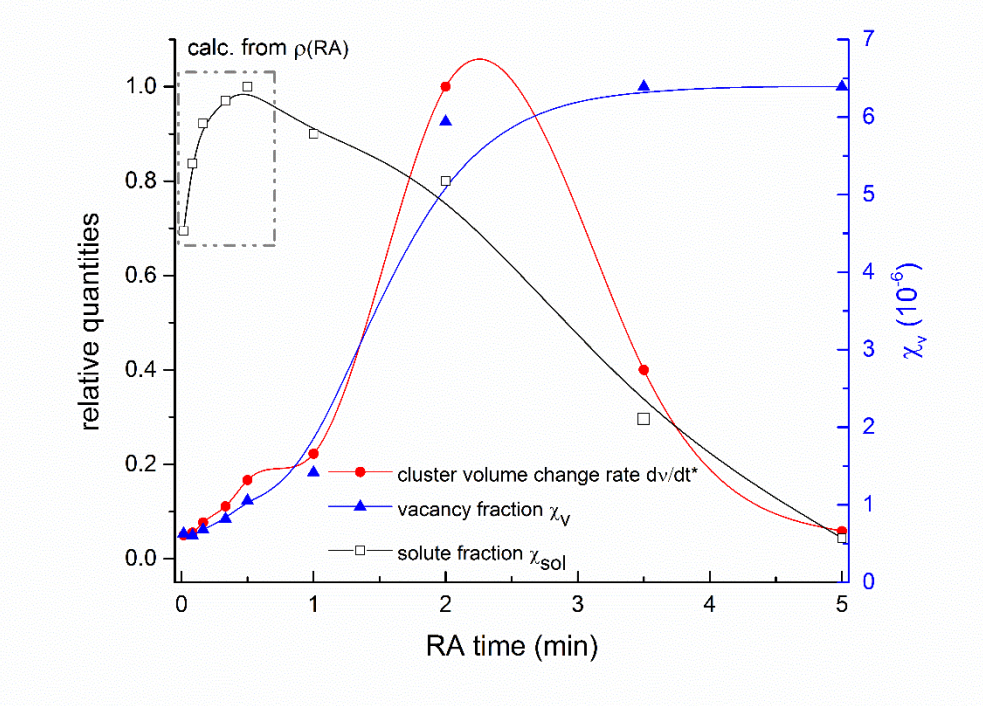

Figure 42. Dependence of various quantities on RA time. Red: rate of cluster volume change derived from slope of resistivity change during first 100 min of NSA, black: cluster volume derived from resistivity after RA, blue: vacancy fraction calculated from Eq. (1) or estimated using knowledge on asymptotic behaviour.

Accordingly, the vacancy site fraction after short RA is higher than at 20 °C but only about 5% of the equilibrium site fraction at 250 °C, pointing at few trapped excess vacancies. While this is possible the initially (< 1 min) slow and then very fast (1 to 2 min) increase seems unreasonable.

The problem is that maximum resistivity increase is found for 2 min RA at a stage when precipitation has set in already and x_{sol} is below its maximal value. This leads to the requirement of a very fast increase of x_{vac} before 2 min RA. This should also lead to a slight increase of positron lifetime between 1 and 2 in of RA, which is not observed in Figure 26.

After 2 min of RA, x_{vac} must be close to the equilibrium value at 250 °C. Taking the slopes of resistivity dρ/dt from Figure 34 for short NSA time (10 min) for both 2 min of RA and AQ, their ratio is ~0.0044. Assuming the same solid supersaturation this ratio must be same as the ratio between the vacancy site fractions at 540 °C and 250 °C, which is the case, see Table 4. This ratio is also found in Figure 38, see red arrow.

As the effects observed cannot be consistently explained by the vacancy and solute site fraction alone, we try to extend Eq. (5.4) to Eq. (5.6) assuming that during RA the two types of solutes Mg and Si are not released in equal fractions but that one species might be released first, the other later. Therefore,

$$\frac{dv}{dt} \propto x_{\mathrm{vac}} \times f\left(x_{\mathrm{Si}}, x_{\mathrm{Mg}}\right), \tag{5.6}$$

The resistivity increase during NPA is influenced by both the Mg and Si content. An increase of Mg and Si accelerates the resistivity increase if the other species is kept constant [94]. In order to find out how different ratios Mg/Si influence resistivity at equal Mg+Si contents, 4 alloy with compositions Al-xMg-ySi and Al-yMg-xSi were compared. x/y had values of 10, 5, 2.5 and 1.33, x+y 0.55, 0.6, 1.4 and 1.4, respectively (see Figure 43).

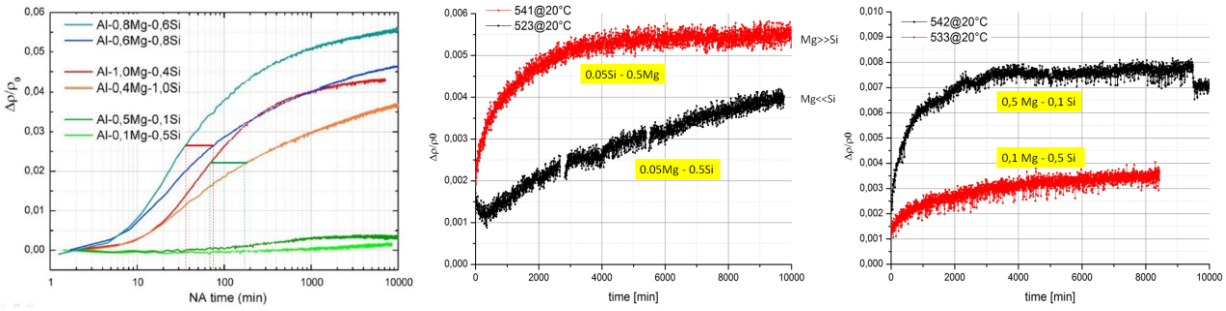

Figure 43. Resistivity during NA for different Al-Mg-Si alloys with mirrored Mg and Si contents [95].

In all cases the alloy with the higher Mg composition showed a much more pronounced increase in resistivity. The difference is larger for the low Mg and Si contents.

Thus, assuming that during RA, Si is released first, followed by Mg would imply that the Mg/Si ratio in the supersaturated solid solution would increase and in this way one would not have to assume the sharp increase of x_v between 30 s and 2 min of RA. The peak of the positron lifetime, see Figure 41, would also be explained since the effect is due to in-diffusion of Mg into existing clusters and this would be accelerated by a high Mg concentration in the solid solution.

For hardness the situation is less clear. Measurements indicate that in the Mg+Si=1.4 alloy the Mg-rich alloy shows a slightly slower hardness increase than the Si-rich variant within the first 1000 min (see Figure 44). However, there are also sources showing the opposite trend.

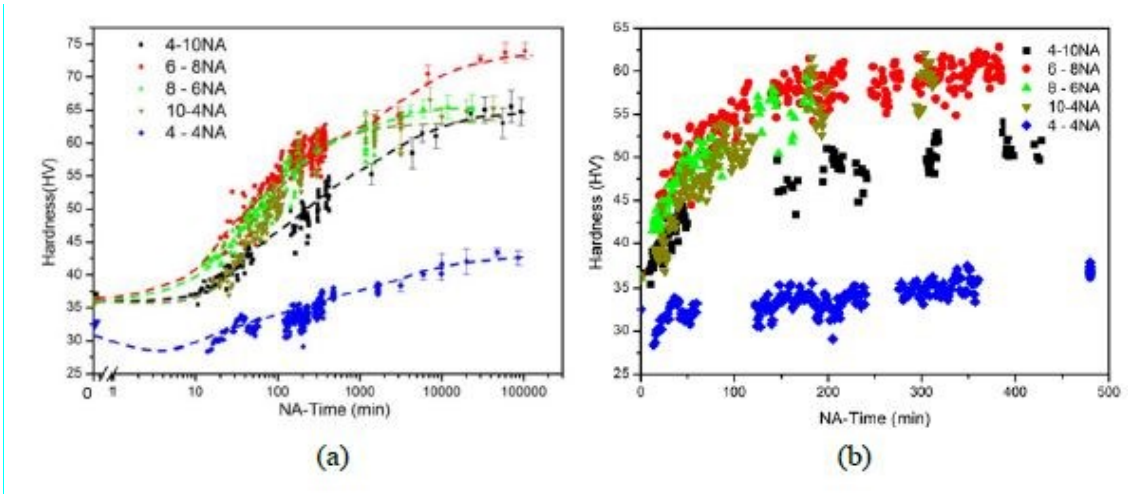

Figure 44. Hardness evolution during NA in various alloys with mirrored concentrations. (a) Logarithmic scale; (b) linear scale for NA 500 min. Broken curves are to guide lines [96].

In conclusion, it is not entirely clear which change of solute content and composition exactly influences the rate of hardening. Any direct measurement, e.g. by APT, would help to establish a model.

6 Conclusions

The underlying microscopic processes during and after artificially ageing (AA) at 180 °C and reverse ageing (RA) at 250 °C in Al-Mg-Si alloys were investigated by positron annihilation lifetime spectroscopy (PALS), Vickers hardness (HV) measurements, electrical resistivity measurements and differential scanning calorimetry (DSC). The main findings are:

- **AA at 180 °C**

AA of solutionized and quenched Al-Mg-Si alloys of different compositions lowers the one-component positron lifetime τ_{1C} measured after AA. How much τ_{1C} is reduced depends on the alloy (lean alloy: more), the heating rate to 180 °C (fast heating: more), natural pre-ageing before AA (if yes: less) and the quenching rate after solutionising (high rate: more). All these observations can be explained by two interdependent effects, that of the loss of excess vacancies and that of clustering and precipitation during heating to 180 °C.

In the lean alloy heated to 180 °C within <1 s, vacancies diffuse to sinks quickly and do hardly assist precipitation. The state produced is that of a sparse population of clusters and some residual excess vacancies. Therefore, positrons annihilate with a short lifetime in the bulk lattice since many of them are not trapped.

This positron lifetime is always longer and hence the trap density higher when clusters or precipitates are formed before or during AA, thereby limit further vacancy losses, which in turn enables further clustering - a self-amplifying effect. This happens when:

- The alloy contains more solute: in this case, clusters are formed already during quenching after solutionising,
- The alloy is heated slowly to 180 °C: in this case, clustering sets in at lower temperatures, which then delays losses of vacancies at higher temperatures.
- The alloy is naturally pre-aged before AA. The clusters formed act in the way described above.
- The alloy is quenched slowly from the solutionising temperature: again, more clusters are formed during quenching before AA.

Natural secondary ageing (NSA) after AA is found to increase τ_{1C} for AA times up to 200 min. The increase is related to clustering of residual solute atoms in the matrix. The alloy composition influences the characteristics of NSA. A high solute content, especially a high Si concentration and fast heating to 180 °C are the conditions for fast NSA, which is driven by a high vacancy concentration and a still high solute supersaturation after AA. The more precipitation takes place during AA and the more vacancies are lost, the slower NSA will be. However, NSA kinetics and solute supersaturation and vacancy concentration do not depend on each other linearly and some open questions exist.

- **RA at 250 °C**

Already the shortest (1 s) reversion ageing (RA) treatment led to pronounced changes of hardness, resistivity and DSC trace, indicating an immediate onset of solute cluster dissolution. This fast onset of dissolution suggests that the vacancy concentration in the naturally aged alloy is still far above the thermal equilibrium value at 20 °C. The very long lifetime of excess vacancies created during solutionising is explained by the presence of clusters that temporarily retain vacancies.

Subsequent natural (secondary) ageing (NSA) after RA provides additional information about clustering. The initial rate of hardening and resistivity increase is much lower than directly after solutionising, reflecting the about 250 times lower vacancy density. However, after a few 100 min of NSA, the hardening and resistivity increase rates merge into the curve of the solutionized and NA curve. In this late stage the vacancy concentration differences must be largely equalised.

Solute supersaturation is found to play an important role. It increases during RA as solute is being sent back from the clusters into the matrix. The observed effects also prove that it is not only the content of the solute in the matrix that governs clustering after RA, but also the chemical composition. A continuously increasing Mg concentration would explain the increase of resistivity and positron lifetime after 2 min of RA, which is beyond the stage of maximum cluster dissolution.

Appendix

A.1 Properties of Heating Media.

Table A.1 The used heating media in this work and their corresponding properties.

Medium	liquid metal "LM" [97]	silicon oil "Oil"	molten salt "MS" [98]	heating plates "HP"
Composition	58% Bi + 42% Sn	Polymethylp-henylsiloxane	53% KNO_3 + 40% $NaNO_2$ + 7% $NaNO_3$	-
Operation Temperature	> 138 °C	-40 ~ 240 °C	142 ~ 500 °C	-
State of samples	in motion	in motion	resting	resting
Heating rate	190 K/s (20 ~ 170 °C) 220 K/s (20 ~ 240 °C)	25 K/s (20 ~ 170 °C)	14 K/s (20 ~ 170 °C) 15 K/s (20 ~ 240 °C)	3 K/s (20 ~ 170 °C)

A.2 Sumpals Program.

Short description of the sumplas program `(Version 4.1.1)` used for the data processing, developed by John Banhart.

Program options

File "_sumup-in.par" has the following format:

```
E              format of input file (has to be E when running version 4)
0 0 0 0 0 0    output print levels. The more 1s, the more output!
0              scanfiles (0=take file information from file, 1= scan for numbered files)
AS             file type (OT=Ortec binary, AS=ASCII single column, MP=mp2 format Halle)
========parameters governing file search, first line dummy unless scanfile=1
Al000          root of filename: files to be read are root+number(3 or 4 digits), no spaces allowed
3              number of digits counting input data files, also for the format of output file
0 0            file range (0 0 = all)
========specify time width of one bin in a spectrum
0              spectrometer no. (0=manual selection, 1=right, 2=Aurelias, 3=vertical, 4=chair bag)
0.0253         channel width in ns [valid only if 0 set in previous line and for filetype OT and AS]
========specify how input spectra are treated
3              shift (0=no,1=integer,2=peak,3=edge,4=3 with manual options)
5 0            maxedge,edgeoffset [values valid only for shift=4, default=5,0]
N              clog (N=linear, Y=logarithmic) [parameter is dummy if shift=0,1,2, valid for shift=3,4]
========binning option etc.
1              no of time channels in each bin
0              0: no selection, use summed file, <>1: sum up from pairs listed in file detectors
========summing options
N 1 0.05       no of files to sum up (0=all), summode (N=normal, L=log, F=float)
========output options
1              normalisation constant
0              column-wise output (0=no, 1=yes)
```

Description of parameters:

Line 1: the letter identifies the correct version of the program

Line 2: the ten integers allow one to turn on further output options. Normally they are all 0. What they do is documented in a comment in the program file.

Line 3: parameter "scanfiles" determines the way the spectra are found

0: directory names are read from file "filelist". Each directory contains a spectrum with a given name compatible with the file structure in Halle. Create a filelist by typing the DOS command: "dir /b >filelist", then edit file.

1: the subdirectory RAW is scanned for files beginning with the root filename (see line 5) plus a number

Line 4: format of input file

OR: binary files created by Ortec software MAESTRO. File ending CHN

AS: headerless spectra in ASCII format. File ending ASC

MP: Halle-type spectra with a header and ASCII text. Ending TXT

Line 6: root filename. Relevant only for scanfile=1.

Line 7: number of digits of input file. Must be 3 or 4.

Input files in mode scanfile=1 then have format “rootnameNNN” or “rootnameNNNN”.

If scanfile=0, this number only determines format of output files (either NNN.dat or NNN.dat, optionally with added time stamp) and has no impact on input file format.

Line 8: file range K,L. If scanfile=1, the range of spectra read is from rootfileK to rootfileL. If both are 0, all files are read. If scanfile=0, only the files listed in filelist within this range given are processed.

Line 10: spectrometer number

0: unspecified spectrometer. In this case the channel width is taken from next line or from spectra

1-4: specified spectrometers. Channel widths are fixed in program code.

Line 11: channel width. Specify here unless using file type MP, where it is given in each spectrum

Line 13: determines how spectra are shifted to compensate for fluctuations of peak position due to hardware instabilities. Makes sense only when spectra are summed up

0=no shift at all

1=integer shift: spectra are shifted by an integer value so that their peak is near channel chanzero=50. This facilitates analysis of series of spectra since peak is always near channel 50.

2=fractional shift: peak region (5 points) of spectra is spline interpolated. Maximum is determined. Peaks are then shifted by fraction of bin width to match position of first file.

3=position of leading edge of peak is determined instead of peak position. Peaks are the shifted to match first spectrum in series. (maxedge=5; edgeoffset=0)

4=3, but maxedge and edgeoffset be chosen manually, see next line

Line 14: parameters governing algorithm to find leading edge of spectra, valid only for shift=4

maxedge: analysis of leading edge is done by considering maxedge points before maximum including maximum.

edgeoffset: allows one to shift the points used. Positive values: move away from peak.

Line 15: determines whether procedure defined by line 13 and 14 (shift =2,3,4) involving spline interpolations is carried out on real values of spectra or on their logarithms. This applies to finding the leading edge or maximum of spectra and to the re-interpolation of spectra after shifting.

n=original values of spectra, y=logarithmic values

Line 17: number of time bins to be summed up. Summing reduces the number of points in each spectrum and increases the count rate (ibin). Should be used when the peak count rate in the spectra is low (say below 10000) since noise can disturb the analysis of peaks due to possible multiple maxima.

1: no binning

>1 binning. Must be smaller than total number of bins

Line 18: This option allows to sum up files from specific detector pairs only if there are more than 2 (as for the 4 detector Halle arrangement).

0: no summing, use all the data provided already summed up previously

>0: read a number of file names from file “detectors” and sum these spectra up during reading

Line 20: This line comes in two versions depending on the parameters. It allows one to sum up blocks of spectra to new spectra.

case 1: summode, isum

summode describes the mode

N: normal mode. Blocks of isum files are summed up. Reduces number of spectra to 1/isum

F: float: blocks of isum files are summed up, but floating from one spectrum to the other. Reduces the number of spectra by isum-1

isum: specifies number of files to be summed up into one new file. isum=0 implies averaging all files to one file.

case 2: summode, istart, tcrit

summode has the value ‘L’ (logarithmic)

istart: specifies at which file the averaging begins (first choice 1)

tcrit: specifies the logarithmic increment (first choice 0.05)

In case two the spectra are summed up to yield an equidistant time mesh on a logarithmic scale. A file “logmesh.dat” is generated that specifies the average time and number of averaged files

Line 22: normalization constant for output spectra

1: no normalization

>1: each spectrum is divided by this integer number

0: normalization constant is equal to isum (see line 20)

Line 23: Generate additional spectrum files containing one bin per line (file format *.col)

References

[1] J. Banhart, Age hardening of aluminium alloys, in: G.E. Totten, D.S. MacKenzie (Eds.) ASM Handbook, Heat Treating of Nonferrous Alloys (Vol. 4E), ASM International, (2016), pp. 214–239

[2] V. Fallah, A. Korinek, N. Ofori-Opoku, B. Raeisinia, M. Gallerneault, N. Provotas, S. Esmaeili, Acta Materialia, 82 (2015) 457-467.

[3] S.J. Andersen, H.W. Zandbergen, J. Jansen, C. Træholt, U. Tundal, O. Reiso, Acta Materialia, 46 (1998) 3283-3298.

[4] C.D. Marioara, S.J. Andersen, J. Jansen, H.W. Zandbergen, Acta Materialia, 49 (2001) 321-328.

[5] S.J. Andersen, C.D. Marioara, A. Frøseth, R. Vissers, H.W. Zandbergen, in: S. McVitie, D. McComb (Eds.) Electron Microscopy and Analysis (EMAG 2003), Institute of Physics, Oxford, 2004, pp. 225-228.

[6] J.H. Chen, E. Costan, M.A. van Huis, Q. Xu, H.W. Zandbergen, Science, 312 (2006) 416-419.

[7] F.D. Fischer, J. Svoboda, F. Appel, E. Kozeschnik, Acta Materialia, 59 (2011) 3463-3472.

[8] J. Banhart, M.D.H. Lay, C.S.T. Chang, A.J. Hill, Phys Rev B, 83 (2011) 014101.

[9] M. Liu, J. Čížek, C.S.T. Chang, J. Banhart, Acta Materialia, 91 (2015) 355–364.

[10] J. Buha, P.R. Munroe, R.N. Lumley, A.G. Crosky, A.J. Hill, in: B.C. Muddle, A.J. Morton, J.-F. Nie (Eds.) International Conference on Aluminium Alloys (ICAA-9), Institute of Materials Engineering Australia, Brisbane, Australia, (2004), pp. 1028-1033.

[11] A. Somoza, A. Dupasquier, I.J. Polmear, P. Folegati, R. Ferragut, Phys Rev B, 61 (2000) 14454-14463.

[12] A. Dupasquier, R. Ferragut, M.M. Iglesias, M. Massazza, G. Riontino, P. Mengucci, G. Barucca, C.E. Macchi, A. Somoza, Philosophical Magazine, 87 (2007) 3297-3323.

[13] J. Banhart, C.S.T. Chang, Z.Q. Liang, N. Wanderka, M.D.H. Lay, A.J. Hill, Adv Eng Mater, 12 (2010) 559-571.

[14] C. Haase, H. Wurst, Zeitschrift für Metallkunde, 33 (1941) 399-403.

[15] H. Uchida, H. Yoshida, Journal of the Japan Institute of Light Metals 46 (1996) 427-431.

[16] I. Polmear, D. StJohn, J.F. Nie, M. Qian, Light Alloys: Metallurgy of the Light Metals, Elsevier Science, 2017.

[17] R.S. Rana, R. Purohit, S. Das, International Journal of Scientific and Research Publications, 2 (2012).

[18] J.R. Davis, Aluminum and Aluminum Alloys, ASM International, (2001).

[19] I. Kovács, J. Lendvai, E. Nagy, Acta Metallurgica, 20 (1972) 975-983.

[20] M.A. van Huis, J.H. Chen, M.H.F. Sluiter, H.W. Zandbergen, Acta Materialia, 55 (2007) 2183-2199.

[21] C.D. Marioara, S.J. Andersen, T.N. Stene, H. Hasting, J. Walmsley, A.T.J. Van Helvoort, R. Holmestad, Philosophical Magazine, 87 (2007) 3385-3413.

[22] K. Matsuda, Y. Uetani, T. Sato, S. Ikeno, Metallurgical and Materials Transactions A, 32 (2001) 1293-1299.

[23] G. Gottstein, Physical Foundations of Materials Science, Springer Berlin Heidelberg, (2004).

[24] I.A. Girifalco, H. Herman, Acta Metallurgica, 13 (1965) 583-590.

[25] H.S. Zurob, H. Seyedrezai, Scripta Materialia, 61 (2009) 141-144.

[26] K. Matsuda, H. Gamada, K. Fujii, Y. Uetani, T. Sato, A. Kamio, S. Ikeno, Metallurgical and Materials Transactions A, 29 (1998) 1161-1167.

[27] M. Murayama, K. Hono, Acta Materialia, 47 (1999) 1537-1548.

[28] C. Ravi, C. Wolverton, Acta Materialia, 52 (2004) 4213-4227.

[29] G.A. Edwards, K. Stiller, G.L. Dunlop, M.J. Couper, Acta Materialia, 46 (1998) 3893-3904.

[30] S.J. Andersen, C.D. Marioara, A. Frøseth, R. Vissers, H.W. Zandbergen, Materials Science and Engineering A, 390 (2005) 127-138.

[31] S. Pogatscher, H. Antrekowitsch, H. Leitner, A.S. Sologubenko, P.J. Uggowitzer, Scripta Materialia, 68 (2013) 158-161.

[32] H.S. Hasting, A.G. Frøseth, S.J. Andersen, R. Vissers, J.C. Walmsley, C.D. Marioara, F. Danoix, W. Lefebvre, R. Holmestad, Journal of Applied Physics, 106 (2009) 123527.

[33] G. Sha, H. Moller, W.E. Stumpf, J.H. Xia, G. Govender, S.P. Ringer, Acta Materialia, 60 (2012) 692-701.

[34] M.W. Zandbergen, Q. Xu, A. Cerezo, G.D.W. Smith, Acta Materialia, 101 (2015) 136-148.

[35] P.H. Ninive, A. Strandlie, S. Gulbrandsen-Dahl, W. Lefebvre, C.D. Marioara, S.J. Andersen, J. Friis, R. Holmestad, O.M. Løvvik, Acta Materialia, 69 (2014) 126-134.

[36] W. Lefebvre, F. Danoix, G. Da Costa, F. De Geuser, H. Hallern, A. Deschamps, M. Dumont, Surface and Interface Analysis, 39 (2007) 206-212.

[37] R. Vissers, M.A. van Huis, J. Jansen, H.W. Zandbergen, C.D. Marioara, S.J. Andersen, Acta Materialia, 55 (2007) 3815-3823.

[38] R. Krause-Rehberg, Positron Annihilation in Semiconductors, Springer, Heidelberg, (1999).

[39] M. Liu, in, Technische Universität Berlin, Berlin, (2014).

[40] M. Bertolaccini, A. Dupasquier, Physical Review B, 1 (1970) 2896-2901.

[41] D.C. Connors, V.H.C. Crisp, R.N. West, Journal of Physics F: Metal Physics, 1 (1971) 355.

[42] W. Brandt, R. Paulin, Physical Review B, 5 (1972) 2430-2435.

[43] R.M. Nieminen, J. Laakkonen, Applied physics, 20 (1979) 181-184.

[44] T.E.M. Staab, E. Zschech, R. Krause-Rehberg, Journal of Materials Science, 35 (2000) 4667-4672.

[45] M. Puska, R.M. Nieminen, Journal of Physics F: Metal Physics, 13 (1983) 333.

[46] W.R. Leo, Techniques for Nuclear and Particle Physics Experiments: A How-to Approach, Springer, (1994).

[47] G.B. Saha, Physics and Radiobiology of Nuclear Medicine, Springer New York, 2013.

[48] J.W. Zhao, B.H. Sun, I. Tanihata, S. Terashima, L.H. Zhu, A. Enomoto, D. Nagae, T. Nishimura, S. Omika, A. Ozawa, Y. Takeuchi, T. Yamaguchi, Nuclear Instruments and Methods in Physics Research Section A: Accelerators, Spectrometers, Detectors and Associated Equipment, 823 (2016) 41-46.

[49] B. Klobes, K. Maier, T.E.M. Staab, Philosophical Magazine, 95 (2015) 1414-1424.

[50] J. Kansy, Nuclear Instruments and Methods in Physics Research Section A: Accelerators, Spectrometers, Detectors and Associated Equipment, 374 (1996) 235-244.

[51] N. Djourelov, M. Misheva, Journal of Physics: Condensed Matter, 8 (1996) 2081.

[52] T.E.M. Staab, B. Somieski, R. KrauseRehberg, Nuclear Instruments & Methods in Physics Research Section a-Accelerators Spectrometers Detectors and Associated Equipment, 381 (1996) 141-151.

[53] E. Hashimoto, M. Iwami, Y. Ueda, Journal of Physics: Condensed Matter, 6 (1994) 1611.

[54] J. Banhart, M. Liu, Y. Yong, Z. Liang, C.S.T. Chang, M. Elsayed, M.D.H. Lay, Physica B, 407 (2012) 2689-2696.

[55] C. Corbel, R.P. Gupta, J. Physique Lett., 42 (1981) 547-550.

[56] O. Melikhova, J. Kuriplach, J. Čížek, I. Procházka, Applied Surface Science, 252 (2006) 3285-3289.

[57] J. Buha, in: School of Materials Science and Engineering, University of New South Wales, Sidney, 2005.

[58] T.E.M. Staab, R. Krause-Rehberg, U. Hornauer, E. Zschech, Journal of Materials Science, 41 (2006) 1059-1066.

[59] T. Honma, K. Matsumoto, Y. Nagai, M. Hasegawa, K. Hono, in: A.J.M. J.F. Nie, B.C. Muddle (Ed.) 9th International Conference on Aluminium Alloys (ICAA9), Institute of Materials Engineering Australasia Ltd, Brisbane, (2004), pp. 494-500.

[60] M. Liu, B. Klobes, J. Banhart, Journal of Materials Science, 51 (2016) 7754-7767.

[61] H. Häkkinen, S. Mäkinen, M. Manninen, Phys Rev B, 41 (1990) 12441-12453.

[62] A. Dupasquier, R. Ferragut, M.M. Iglesias, F. Quasso, Physica Status Solidi C - Current Topics in Solid State Physics, Vol 4, No 10, 4 (2007) 3526-3529.

[63] P. Lang, Y.V. Shan, E. Kozeschnik, Materials Science Forum, 794-796 (2014) 963-970.

[64] E. Gramsch, K.G. Lynn, Phys Rev B, 40 (1989) 2537-2540.

[65] J. Lipka, Jordan Journal of Physics 2(2009) 73-88.

[66] Z.Q. Liang, C.S.T. Chang, C. Abromeit, J. Banhart, J. Hirsch, Int J Mater Res, 103 (2012) 980-986.

[67] A. Falahati, P. Lang, E. Kozeschnik, Materials Science Forum, 706-709 (2012) 317-322.

[68] M. Kubota, J.F. Nie, B.C. Muddle, Materials Transactions, 45 (2004) 3256-3263.

[69] M. Torsaeter, in, NTNU Trondheim, 2011.

[70] Z.Q. Liang, in, South China University of Technology, (2009).

[71] C.H. Liu, Y.X. Lai, J.H. Chen, G.H. Tao, L.M. Liu, P.P. Ma, C.L. Wu, Scripta Materialia, 115 (2016) 150-154.

[72] Y.X. Lai, B.C. Jiang, C.H. Liu, Z.K. Chen, C.L. Wu, J.H. Chen, Journal of Alloys and Compounds, 701 (2017) 94-98.

[73] F.A. Martinsen, F.J.H. Ehlers, M. Torsæter, R. Holmestad, Acta Materialia, 60 (2012) 6091-6101.

[74] C. Panseri, T. Federighi, Journal of the Institute of Metals London, 94 (1966) 99-197.

[75] H. Seyedrezai, D. Grebennikov, P. Mascher, H.S. Zurob, Materials Science and Engineering A, 525 (2009) 186-191.

[76] M.J. Starink, L.F. Cao, P.A. Rometsch, Acta Materialia, 60 (2012) 4194-4207.

[77] R.K.W. Marceau, A. de Vaucorbeil, G. Sha, S.P. Ringer, W.J. Poole, Acta Materialia, 61 (2013) 7285-7303.

[78] M.D.H. Lay, H.S. Zurob, C.R. Hutchinson, T.J. Bastow, A.J. Hill, Metallurgical and Materials Transactions A, 43A (2012) 4507-4513.

[79] Y. Aruga, M. Kozuka, Y. Takaki, T. Sato, Materials Science and Engineering A, 631 (2015) 86-96.

[80] L.C. Smedskjaer, M. Manninen, M.J. Fluss, Journal of Physics F: Metal Physics, 10 (1980) 2237.

[81] J. Čižek, M. Vlach, O. Melikhova, M. Vlcek, I. Procházka, B. Smola, I. Stuliková, in: Positron Studies of Defects (PSD-17), Dresden-Rossendorf, (2017), pp. Conference handout.

[82] A. Serizawa, T. Sato, in: J. Hirsch, B. Skrotzki, G. Gottstein (Eds.) 11th International Conference on Aluminium Alloys (ICAA11), Wiley VCH, Aachen, Germany, (2008), pp. 915-921.

[83] M.W. Zandbergen, Q. Xu, A. Cerezo, G.D.W. Smith, Data in Brief, 5 (2015) 626-641.

[84] A.I. Morley, M.W. Zandbergen, A. Cerezo, G.D.W. Smith, Materials Science Forum 519-521 (2006) 543-548.

[85] M. Torsæter, W. Lefebvre, S.J. Andersen, C.D. Marioara, J. Walmsley, R. Holmestad, in: S. Kumai, O. Umezawa, Y. Takayama, T. Tsuchida, T. Sato (Eds.) 12th International Conference on Aluminium Alloys (ICAA12), The Japan Institute of Light Metals, Yokohama, (2010), pp. 1385-1390.

[86] V. Fallah, B. Langelier, N. Ofori-Opoku, B. Raeisinia, N. Provatas, S. Esmaeili, Acta Materialia, 103 (2016) 290-300.

[87] H. Li, W.Q. Liu, Metall Mater Trans A, 48A (2017) 1990-1998.

[88] C.S.T. Chang, J. Banhart, Metallurgical and Materials Transactions A, 42A (2011) 1960-1964.

[89] A.K. Gupta, D.J. Lloyd, Metallurgical and Materials Transactions A, 30 (1999) 879-884.

[90] A.K. Gupta, D.J. Lloyd, S.A. Court, Materials Science and Engineering A, 301 (2001) 140-146.

[91] L. Zhen, S.B. Kang, Materials Letters, 37 (1998) 349-353.

[92] H. Herman, M.E. Fine, J.B. Cohen, Acta Metallurgica, 11 (1963) 43-56.

[93] A. Serizawa, S. Hirosawa, T. Sato, Metallurgical and Materials Transactions A, 39A (2008) 243-251.

[94] S.N. Kim, J.H. Kim, H. Tezuka, E. Kobayashi, T. Sato, Materials Transactions, 54 (2013) 297-303.

[95] M. Wustenhagen, in, Technischen Universität Berlin, Berlin, (2016), pp. 49.

[96] Y. Yan, in, Technische Universität Berlin, Berlin, (2014).

[97] H. Ge, H. Li, S. Mei, J. Liu, Renewable and Sustainable Energy Reviews, 21 (2013) 331-346.

[98] Q. Peng, X. Wei, J. Ding, J. Yang, X. Yang, International Journal of Energy Research, 32 (2008) 1164-1174.

Acknowledgements

To all the people who have contributed to this dissertation:

- Prof. Dr. John Banhart, for the supervision of this work and giving me the opportunity to pursue my PhD at the Technische Universität Berlin and the Helmholtz Zentrum Berlin. I am deeply indebted to him for his excellent supervision and guidance of how to think and work scientifically.

- Prof. Dr. Olaf Keßler (*Uni. Rostock, Germany*), for his willingness to review this dissertation.

- Dr. Meng Liu, for giving me supports in experiments, discussion, and thesis writing during my PhD period.

- Dr. Nelia Wanderka and Prof. Dr. Marwan Mousa (*Mutah Uni., Jordan*), for their support and help before and during my PhD.

- Dr. Anna Manzoni, Dr. Florian Vogel, Dr. Andre Hilger, Dr. Francisco Garcia-Moreno and Mr. Tillmann Neu, for their scientific help.

- Christiane Ciceron, Christiane Förster, Claudia Leistner, Norbert Beck and Jörg Bajorat, for the technical support.

- Prof. Dr. R. Krause-Rehberg and Dr. Mohamad (*Uni. Of Halle, Germany*), for producing the required isotope. Prof. Dr. Jakub Čížek (*Charles Uni. in Prague, Czech Republic*), for the opportunity to carry out PALS experiments with his spectrometer.

- Xingpu Zhang, Zi Yang, Saad Alrwashdeh, Ala'a Al-Falahat, Andria Fantin and Andreas Röhsler for their support and help during my PhD period.

- Jürgen Hirsch from Hydro Aluminium Bonn for providing the alloys.

- All colleagues and friends who helped and supported me during my PhD period.

Finally, my deepest gratitude to my parents, 'Priest' Adel Madanat & Wardeh Kawaleet, my brother and my sisters & their families. Whom their continuous support, enormous sacrifice, and endless love, made it possible to go all the way in my PhD period.